LASER-POLARIZED LIQUID XENON

Karen Louise Sauer

A DISSERTATION

PRESENTED TO THE FACULTY

OF PRINCETON UNIVERSITY

IN CANDIDACY FOR THE DEGREE

OF DOCTOR OF PHILOSOPHY

RECOMMENDED FOR ACCEPTANCE

BY THE DEPARTMENT OF

PHYSICS

NOVEMBER 1998

Acknowledgements

Many members of the faculty have helped me during my time at Princeton; I would especially like to thank Professor Ong, Professor Treiman, Professor Cates, Professor Young, and Professor Sherr. Most importantly, I would like to thank Professor Will Happer for his guidance and support.

Numerous people have contributed with their time, skill, or equipment to making this thesis happen. I would like to acknowledge Richmond Sarpong for synthesizing the deuterated dimethyldichlorosilane, Fred Loeser for loaning me the liquid nitrogen dewar and so many other things, Ted Griffith, Laszlo, and Al for all their shop advice, Mike Souza for the emergency glass-blowing, Bart Gibbs for his electronics advice, and Claud for his general assistance.

It has been my good fortune to make many good friends during my stay at Princeton. I would like to thank Jason for trying to make me laugh while writing this document. I appreciate Jill and Weihsueh for sharing wedding woes and helping me through on the big day. I would like to thank the lunchtime (and dinner time and tea time and midnight snack time – you get the idea) crew of Rick, Ingrid, Eddie, and Weihsueh for being, as Amir put it, a support group. I would also like to thank all those crazy cats in the basement who helped me through generals – Chris H., Rick, Cheenu, and Peter. I appreciate Becky for putting up with all my silly chemistry questions. Thank you to Heidi, Nicole, and Seahwa for showing me life beyond the

physics department.

Over the years I have had the pleasure to work with many people in the atomic-nuclear group. Bastiaan Driehuys, Hunter Middleton, Paul Bogorad, and Brian Saam advised me and brought me through my earlier years in Princeton. I would like to thank Mike Romalis for always being willing to listen to my experimental woes and giving me helpful insights. Thank you to Christopher Erickson for his good questions and discussions. I have come to appreciate Dan Walter's humor and helpfulness over the years. Brian Humensky, Ioannis Kominis, Tina Pavlin, and Ming Hsu have also added much to my experience at Princeton. I would especially like to thank Richard Fitzgerald who has been my partner in the work presented here on liquid Xe. It was a joy to work with such a capable scientist. I appreciate his diligence and perseverance in correcting the first draft of this thesis.

I appreciate my grandparents', my parents', and my sister's prayers and encouragement of me on this long journey. My husband, Brian Mark, has been a constant blessing to me throughout my years at Princeton. His support, his patience, and his love has meant a lot to me. It is to him that I dedicate this thesis.

Abstract

Because of the burgeoning applications of laser-polarized ^{129}Xe in biomedicine, materials, and fundamental physics, the ^{129}Xe relaxation mechanisms in gaseous and solid laser-polarized Xe have been extensively studied. We now extend those investigations to the liquid phase. By measuring the ^{129}Xe relaxation rate in liquid Xe as a function of magnetic field, temperature, and container surface, we determine that the major relaxation mechanisms are interaction with the surface and spin-rotation between pairs of Xe atoms. In addition, we have developed an elegant technique where, by the use of a single radio frequency, we match the Rabi frequency of surface protons to the ^{129}Xe Larmor frequency. The increase in ^{129}Xe relaxation rate caused by such a resonant condition shows that the dipole-dipole coupling between surface protons and ^{129}Xe has a significant contribution to the zero-field relaxation rate of ^{129}Xe.

The ^{129}Xe lifetime in the liquid is found to be on the order of 20-30 minutes and has only a mild dependence on temperature, magnetic field, and surface environment. Its insensitivity to these parameters makes it a convenient method for the transportation of large quantities of laser-polarized ^{129}Xe (as needed, for example, for magnetic resonance imaging of the human lungs). Furthermore, we explore in this thesis another promising application of liquid Xe in which the large nuclear polarization of ^{129}Xe ($\sim$20%) has been transferred through cross-relaxation to other spins dissolved in the liquid Xe. We have measured enhanced NMR signals for ^{1}H that are more

than a factor of 45 larger than thermal polarization signals at 200 K and 14 kG. For ^{13}C we have seen signal enhancements of over 70. Furthermore, in dissolving toluene in liquid Xe, we have observed different enhancements of the ring and methyl proton signals. The lifetimes of the enhancements are on the order of $\sim$20 min.

Contents

List of Tables

List of Figures

Chapter 1

Introduction

The first experiments on spin exchange between optically pumped alkali atoms and noble gas nuclei were carried out by Bouchiat, Carver, and Varnum [1] in 1960. They demonstrated that it was possible to transfer some of the angular momentum of optically pumped Rb atoms to the nuclei of ^{3}He gas. Through this method they attained a polarization on the order of .01% in 77 amagat-cm^3 [2] of ^{3}He. (For a spin-1/2 particle, the polarization is the difference between the number of spins aligned and the number of spins anti-aligned with the magnetic field divided by the total number of spins.) In 1978, Grover [3] showed that the electron-nuclear spin exchange could take place between Rb atoms and ^{129}Xe nuclei, achieving 10% ^{129}Xe polarization in 0.009 amagat-cm^3 (65% ^{129}Xe enriched). Since those intial experiments, advances both in the understanding of spin-exchange optical pumping and in the equipment used for it have increased both the quantities of laser-polarized ^{3}He and ^{129}Xe and their polarizations. For example, the recent development of high power diode-laser arrays, which can provide tens to hundreds of watts of pumping light, have improved the performance of spin-exchange optical pumping and greatly decreased the cost [4]. The recent nuclear physics experiment E-154 at SLAC, which relied on laser diode arrays for most of the optical pumping, attained nearly 50% polarization in about 1600 amagat-cm^3 [5, 6]. Using a laser diode array and a flowing gas system [7], as described in Chapter 3, 20% ^{129}Xe polarization in natural Xe has been produced at a rate of approximately 200 amagat-cm^3 per hour.

The large polarization of these laser-polarized noble gases are to be compared to thermal polarization. For a temperature T, magnetic field $\mathbf{H}$, and a spin-1/2 particle of magnetic moment $\boldsymbol{\mu}$, the thermal polarization is given by Boltzmann statistics as

$$P_B = \tanh\left(\frac{\boldsymbol{\mu}\cdot\mathbf{H}}{kT}\right) \approx \frac{\boldsymbol{\mu}\cdot\mathbf{H}}{kT} \tag{1.1}$$

where k is the Boltzmann constant. For example, in the typical 10 kG field used for magnetic resonance imaging (MRI), the proton polarization in a human is 3×10^{-6}, five orders of magnitude smaller than the laser-polarized noble gases. Therefore the laser-polarized noble gases have a large potential for signal enhancement, even though their spin density is smaller than the typical proton density by three orders of magnitude.

The large quantity and high nuclear polarization attainable with laser-polarized noble gases has led to many innovative applications in numerous fields, from fundamental physics to biomedicine. Some examples of the fundamental physics experiments include the first determination of the neutron spin structure function, measured by scattering polarized, high-energy electrons from highly polarized ^{3}He targets [8], studies of fundamental symmetries [9, 10], and the use of ^{3}He for neutron polarizers and polarimeters [11]. Hyperpolarized ^{3}He and ^{129}Xe has also been used for high resolution imaging of the void spaces in the lungs [12, 13, 14, 15, 16], the oral cavity [17], and materials [18].

Although ^{3}He has a larger magnetic moment than ^{129}Xe and can currently be more highly polarized, ^{129}Xe can be used in many important applications in which ^{3}He cannot. Unlike ^{3}He [19], ^{129}Xe is quite soluble in many materials [20, 21] and the ^{129}Xe nuclear magnetic resonance (NMR) signal is quite sensitive to its environment [22]. Therefore imaging dissolved laser-polarized ^{129}Xe in the blood, brain, and other tissues is very attractive and is being actively explored [16, 23, 24, 25, 26]. This high sensitivity of Xe to its local environment, as well as its chemical inertness, has also made laser-polarized ^{129}Xe an excellent probe of chemical environments [27, 28, 29]. Part of this thesis (see Chapter 4) extends the work of Driehuys [30, 31] in which laser-polarized ^{129}Xe is used to probe the dipole-dipole coupling between surface protons and ^{129}Xe.

Laser-polarized ^{129}Xe has also been used to transfer its large nuclear polarization to other spin species. The use of laser-polarized Xe as a solute [32] and adsorbate [33, 34, 35] has been shown to enhance proton NMR signals. We explore the use of similar polarization transfer techniques with liquid Xe as the *solvent* (see Chapter 5). Liquid Xe has previously been shown to be an excellent inert solvent for numerous biological and organic molecules [36, 37]. We observe signal enhancements from the dissolved molecules of over 45 for ^{1}H and over 70 for ^{13}C, compared to their thermal polarization signals at 200 K and 14 kG [38].

Many of the above experiments rely not only on having a large volume of highly polarized ^{129}Xe or ^{3}He, but also on keeping the non-equilibrium polarization for as long as possible. Therefore the relaxation rate of laser-polarized ^{129}Xe in the gaseous

and solid form have been extensively studied [39, 31, 40, 41]. In this thesis we extend the investigations of laser-polarized ^{129}Xe to the liquid phase. Figure 1.1 shows the phase diagram for Xe. Point A is the triple point (0.81 atm, 161.4 K) and C is the critical point (57.5 atm, 289.7 K) [42].

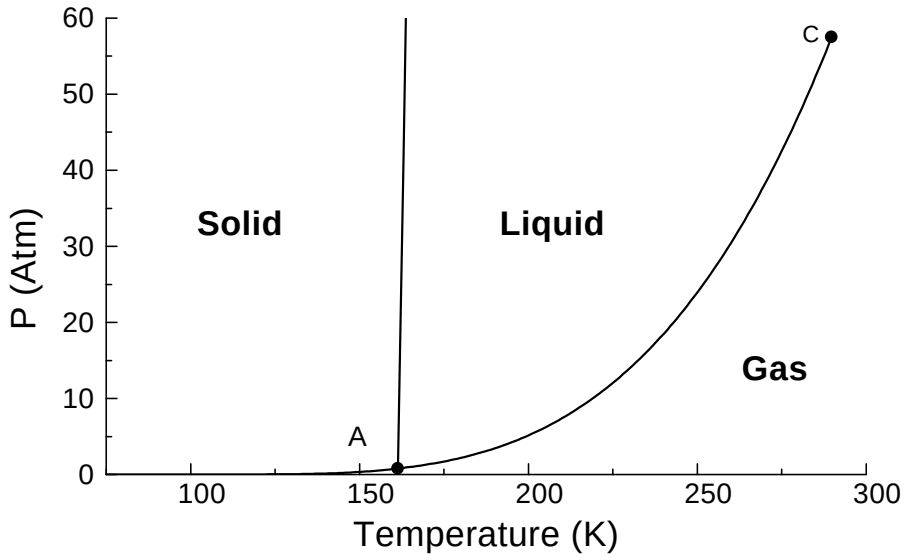

Figure 1.1: Xe phase diagram [42]. Point A is the triple point, point C is the critical point.

At high pressures, the ^{129}Xe relaxation mechanism in the gas has been proposed theoretically to be the spin-rotation interaction [43] in response to the experimental results of Hunt and Carr [44]. In the spin-rotation interaction the ^{129}Xe nucleus couples to the rotational motion of a diatomic configuration (^{129}Xe-Xe pair). However, at pressures on the order of an atmosphere, the ^{129}Xe relaxation has been found to be dominated by interactions with the surface of the container that holds it [45, 30, 31]. In the gas phase, ^{129}Xe can relax by diffusion through magnetic field gradients [46, 47, 48].

In magnetic fields above 1 kG, the spin-rotation interaction has also been found to

be the main ^{129}Xe relaxation mechanism in solid Xe [40] where the rotation is caused by a Raman scattering of phonons. At cold temperatures $T \leq 55$ K the phonons begin to freeze out: at 77 K (liquid nitrogen temperature) the ^{129}Xe lifetime is about three hours, whereas at 4.2 K the ^{129}Xe lifetime is on the order of 500 hours. These long ^{129}Xe lifetimes at low temperatures make solid Xe almost the ideal storage method for laser-polarized ^{129}Xe. However, at fields less than 500 G the relaxation rate increases as a function of decreasing magnetic field until at Earth's magnetic field ($\sim$0.5 G) ^{129}Xe has a lifetime of less than a minute at temperatures down to 77 K [49]. At these low magnetic fields the ^{129}Xe relaxation rate in the solid is dependent on the sample's isotopic composition and is not completely understood.

The spin-rotation was proposed by Torrey [43] and Oppenheim *et al.* [50] to be the main mechanism of relaxation for the liquid Xe, in response to Hunt and Carr's experimental results using liquid Xe with thermal equilibrium polarization [44]. Using laser-polarized liquid Xe, with about five orders of magnitude more polarization than thermal polarization, we study in this thesis the ^{129}Xe relaxation rate as a function of magnetic field, temperature, and chemical environment. Our results, as shown in Chapter 4, indicate that both the spin-rotation mechanism and surface interactions contribute to the ^{129}Xe relaxation rate in liquid Xe. However, in contrast to Xe gas, the ^{129}Xe relaxation rate in the liquid is not very sensitive to the surface or to field gradients (for the temperatures we studied, the diffusion constant of the liquid is approximately three orders of magnitude smaller than in the gas at STP [51, 52]). In contrast to solid Xe, the relaxation rate in the liquid is not very sensitive to magnetic field or temperature. Because of its insensitivity and relatively long lifetimes (20-30 minutes) the liquid provides a convenient means of transporting large quantities of laser-polarized Xe *without the constraint of a holding field.* The temperature demands can be readily met with a bath of ethanol and dry ice at 198 K [53].

In the next chapter we discuss the theory used to describe cross-relaxation between ^{129}Xe and other spins due to dipole-dipole coupling. This theory is applied to both the case in which molecules are dissolved in liquid Xe and the case where the ^{129}Xe relaxation rate is dominated by interaction with surface spins. Chapter 3 describes the experimental techniques employed in this thesis, including the development of a very simple yet elegant method for exploring the contribution of dipole-dipole coupling between surface protons and ^{129}Xe to the total ^{129}Xe relaxation rate. The application of this method is demonstrated in Chapter 4. Chapter 4 also shows the results of the measurement of the ^{129}Xe relaxation rate in liquid Xe as a function of magnetic field,

temperature, and surface environment. In addition, it discusses the theory of spin-rotation as applied to liquid Xe. In the final chapter we discuss a novel application of liquid Xe in which the polarization of the ^{129}Xe is transferred to the spins on molecules dissolved in the liquid. The appendix catalogs the cells that were made when exploring the interaction of gaseous ^{129}Xe with surfaces.

Chapter 2

Theory of Cross-relaxation between ^{129}Xe and ^{1}H

Dipole-dipole coupling between ^{129}Xe and ^{1}H, either on molecules dissolved in laser-polarized liquid Xe or on the surface of the container containing the liquid Xe, can be a significant source of relaxation to the ^{129}Xe polarization. Moreover, through this dipole-dipole coupling, the laser-polarized ^{129}Xe can transfer some of its polarization to the ^{1}H. This cross-relaxation process has been called spin polarization-induced nuclear Overhauser effect (SPINOE) [32]. SPINOE requires no radio-frequency irradiation of the spins because the energy mismatch between the intial and final spin states is transferred to random motions of the lattice. In this chapter, we derive the equations that govern the evolution in time of the ^{129}Xe and ^{1}H polariztions under dipole-dipole coupling to each other. Although we focus on the interaction of ^{129}Xe with ^{1}H, all of the equations derived are equally applicable to the interaction of ^{129}Xe with other spin-1/2 nuclei, such as ^{13}C. The initial part of this chapter closely follows the treatment in Abragam [54] of relaxation by dipole-dipole coupling in gases and liquids immersed in a static magnetic field. However, Abragam uses approximations based on the assumption that the spin polarizations are close to thermal equilibrium values. We re-evaluate these assumptions in light of the large non-equilibrium polarization of ^{129}Xe. We extend the equations governing the two-spin system to include other relaxation mechanisms besides dipole-dipole coupling and calculate the solution to these equations for the case in which the ^{1}H are on molecules dissolved in liquid Xe. The relaxation rate of ^{129}Xe is further calculated for the situation that radio frequency (rf) at the ^{1}H Larmor frequency is applied to the system.

The expectation values of the ^{129}Xe spin and the ^{1}H spin, of nuclear spin quantum

number K and I respectively, are determined by the density matrix ρ

$$\langle \mathbf{K} \rangle = \mathrm{tr}\{\rho \mathbf{K}\}; \quad \langle \mathbf{I} \rangle = \mathrm{tr}\{\rho \mathbf{I}\} \tag{2.1}$$

The density matrix, and therefore the expectation values of the spins, evolves with time under influence of the Hamiltonian $\hbar(\mathcal{H}_0 + \mathcal{H}_1)$ where $\hbar\mathcal{H}_0$ is the main Hamiltonian and $\hbar\mathcal{H}_1$ is the perturbing Hamiltonian. In the cases discussed in this thesis, $\mathcal{H}_0$ is due to the interaction of the spins with a static magnetic field and with an applied rf, while $\mathcal{H}_1$ is due to random magnetic field fluctuations caused by neighboring magnetic nuclei. These random fluctuations are invariant under a change in origin of time, and therefore the autocorrelation function $\overline{\mathcal{H}_1(t), \mathcal{H}_1^*(t+\tau)}$ is dependent only on τ. We assume that this autocorrelation function is proportional to $\exp(-|\tau|/\tau_c)$ where the correlation time τ_c is the time scale of the random fluctuations. According to the Wiener-Khintchin Theorem, the corresponding power spectral density at the radio frequency ω must be proportional to $(1+\omega^2\tau_c^2)^{-1}$, so energy mismatches ΔE, of magnitudes up to $\Delta E = \hbar\omega \sim \hbar/\tau_c$, are readily absorbed or supplied by the random fluctuations.

2.1 Time Evolution of the Density Matrix

The equation of motion for ρ is the Liouville equation,

$$\frac{1}{i}\frac{d\rho}{dt} = -[\mathcal{H}_0 + \mathcal{H}_1, \rho], \tag{2.2}$$

For ease of calculation, and to avoid the rapidly oscillating coupling caused by $\mathcal{H}_0$, we use the interaction representation where

$$\tilde{\rho} = e^{i\mathcal{H}_0 t}\rho e^{-i\mathcal{H}_0 t}; \quad \tilde{\mathcal{H}_1} = e^{i\mathcal{H}_0 t}\mathcal{H}_1 e^{-i\mathcal{H}_0 t} \tag{2.3}$$

Using this interaction representation, the Liouville equation is simplified to

$$\frac{1}{i}\frac{d\tilde{\rho}}{dt} = -[\tilde{\mathcal{H}_1}, \tilde{\rho}] \tag{2.4}$$

By successive integration of Eq. (2.4), $\tilde{\rho}$ can be approximated up to second order in $\tilde{\mathcal{H}_1}$ by

$$\tilde{\rho} = \tilde{\rho}(0) - i\int_0^t [\tilde{\mathcal{H}_1}(t'), \tilde{\rho}(0)]dt' - \int_0^t dt' \int_0^{t'} dt''[\tilde{\mathcal{H}_1}(t'), [\tilde{\mathcal{H}_1}(t'', \tilde{\rho}(0)]] \tag{2.5}$$

Taking the time derivative of this expression and substituting in $\tau = t - t'$, we find

$$\frac{d\tilde{\rho}}{dt} = -i[\tilde{\mathcal{H}}_1(t), \tilde{\rho}(0)] - \int_0^t d\tau [\tilde{\mathcal{H}}_1(t), [\tilde{\mathcal{H}}_1(t-\tau), \tilde{\rho}(0)]] \tag{2.6}$$

Because $\tilde{\mathcal{H}}_1$ is a random operator, it is necessary to use an ensemble-averaged density operator $\overline{\tilde{\rho}}$ to calculate what an experiment would measure. To obtain an expression for $\overline{\tilde{\rho}}$ an ensemble average is taken over both sides of Eq. (2.6).

We assume that $\overline{\tilde{\mathcal{H}}_1} = 0$ and that $\tilde{\mathcal{H}}_1$ and $\tilde{\rho}$ can be averaged separately so that the first term in Eq. (2.6) averages to zero. By neglecting the correlation between $\tilde{\mathcal{H}}_1$ and ρ and assuming a short correlation time, it can be shown that $\tilde{\rho}(0)$ can be replaced by $\tilde{\rho}(t)$ in the right hand side of Eq. (2.6) [54]. Contributions to the integral in Eq. (2.6) from values of $\tau \gg \tau_c$ are negligible, and therefore the upper limit of the integral can be extended to ∞. Using these assumptions, Eq. (2.6) becomes

$$\frac{\overline{d\tilde{\rho}}}{dt} = -\int_0^\infty d\tau \overline{[\tilde{\mathcal{H}}_1(t), [\tilde{\mathcal{H}}_1(t-\tau), \tilde{\rho}(t)]]}. \tag{2.7}$$

2.2 Time Evolution of an Observable

The time evolution of the operator Q acting on the variables of the system can be found by multiplying both sides of Eq. (2.7) by Q and taking the trace. By detailed balance, $d\tilde{\rho}/dt$ must be zero when the density operator is equal to the thermal equilibrium density operator matrix ($\tilde{\rho} = \tilde{\rho}_0 = \rho_0$). Therefore we must replace $\tilde{\rho}$ by $\tilde{\rho} - \rho_0$ in Eq. (2.7). Proceeding with these steps, and using the invariance of the trace of a product of matrices under cyclic permutation of the matrices, Eq. (2.7) becomes

$$\frac{d\langle\tilde{Q}\rangle}{dt} = -\mathrm{tr}\{\mathcal{A}_Q(\tilde{\rho} - \rho_0)\} \tag{2.8}$$

where

$$\mathcal{A}_Q = \int_0^\infty d\tau \overline{[\tilde{H}_1(t-\tau), [\tilde{H}_1(t), Q]]}. \tag{2.9}$$

Equation (2.8) describes the evolution of the expectation value of Q in the interaction representation

$$\langle\tilde{Q}\rangle = \mathrm{tr}\{\tilde{\rho}Q\}. \tag{2.10}$$

However, if Q commutes with the unperturbed Hamiltonian $\mathcal{H}_0$ then $\langle\tilde{Q}\rangle = \langle Q\rangle$. In most of the experiments employed in this thesis the examined observable, such as K_z, commutes with $\mathcal{H}_0$.

2.3 Relaxation by Dipolar Coupling in a DC Field

The dipole-dipole coupling between the nucleus of a ^{129}Xe atom with spin $\mathbf{K}$ and the nucleus of a ^{1}H atom with spin $\mathbf{I}$ can be represented as

$$\frac{3(\boldsymbol{\mu}_K \cdot \hat{\mathbf{r}})(\boldsymbol{\mu}_I \cdot \hat{\mathbf{r}})}{r^3}, \tag{2.11}$$

where $\mathbf{r}$ is the displacement between the two nuclei. The ^{129}Xe magnetic moment $\boldsymbol{\mu}_K$ and the ^{1}H magnetic moment $\boldsymbol{\mu}_I$ can be written as

$$\boldsymbol{\mu}_K = \hbar\gamma_K \mathbf{K}, \quad \boldsymbol{\mu}_I = \hbar\gamma_I \mathbf{I}, \tag{2.12}$$

where γ_K and γ_I are the ^{129}Xe and ^{1}H gyromagnetic ratios. Using these definitions in Eq. (2.11), we can expand $\mathcal{H}_1$ as

$$\mathcal{H}_1 = \sum_q F^{(q)}(t) A^{(q)}, \tag{2.13}$$

where

$$F^{(0)} = \frac{1 - 3\cos^2\theta}{r^3}, \quad F^{(1)} = \frac{\sin\theta\cos\theta e^{-i\phi}}{r^3}, \quad F^{(2)} = \frac{\sin^2\theta e^{-2i\phi}}{r^3}, \tag{2.14}$$

$$\begin{aligned} A^{(0)} &= \alpha\{-\frac{2}{3}K_z I_z + \frac{1}{6}(K_+ I_- + K_- I_+)\}, \\ A^{(1)} &= \alpha\{K_z I_+ + K_+ I_z\}, \\ A^{(2)} &= \frac{1}{2}\alpha K_+ I_+, \end{aligned} \tag{2.15}$$

and the constant α is $-\frac{3}{2}\gamma_K\gamma_I\hbar$. Note that $F^{(0)}A^{(0)}$ is Hermitian, while $F^{(-1)}A^{(-1)}$ and $F^{(-2)}A^{(-2)}$, which are not listed above, are simply the Hermitian conjugates of $F^{(1)}A^{(1)}$ and $F^{(2)}A^{(2)}$ respectively. $F^{(q)}$ contains the part of $\mathcal{H}_1$ randomly dependent on time and $A^{(q)}$ are operators on the system.

The main Hamiltonian describes the motion of spin K and I in a static magnetic field of strength H_0 as

$$\hbar\mathcal{H}_0 = \hbar(\omega_{0K} K_z + \omega_{0I} I_z) \tag{2.16}$$

where the Larmor frequency of K is $\omega_{0K} = -\gamma_K H_0$ and the Larmor frequency of I is $\omega_{0I} = -\gamma_I H_0$. Using this Hamiltonian, $\tilde{\mathcal{H}}_1$ can be calculated in the interaction representation,

$$\begin{aligned} \tilde{\mathcal{H}}_1 &= \sum_q F^{(q)}(t)(e^{i\mathcal{H}_0 t} A^{(q)} e^{-i\mathcal{H}_0 t}) \\ &= \sum_q F^{(q)}(t)(\sum_p A_p^{(q)} e^{i\omega_p^{(q)} t}), \end{aligned} \tag{2.17}$$

where $A^{(q)}$ has been further expanded into values of $A_p^{(q)}$ corresponding to the distinct transitions between states of the system and $\hbar\omega_p^q$ is the difference in energy between these states.

For the case of dipole-dipole coupling, $A^{(0)}$ in the rotating frame becomes

$$\begin{aligned}\tilde{A}^{(0)} &= e^{i\mathcal{H}_0 t}A^{(0)}e^{-i\mathcal{H}_0 t} = \sum_p A_p^{(q)}e^{i\omega_p^{(q)}t} \\ &= -\frac{2}{3}\alpha K_z I_z + \frac{1}{6}\alpha K_+ I_- e^{i(\omega_{0K}-\omega_{0I})t} + \frac{1}{6}\alpha K_- I_+ e^{-i(\omega_{0K}-\omega_{0I})t} \end{aligned} \tag{2.18}$$

Therefore the components $A_p^{(0)}$ are

$$\begin{aligned} &A_1^{(0)} = -\tfrac{2}{3}\alpha K_z I_z, \quad && A_2^{(0)} = \tfrac{1}{6}\alpha K_+ I_-, \quad && A_3^{(0)} = \tfrac{1}{6}\alpha K_- I_+ \\ &\omega_1^{(0)} = 0, && \omega_2^{(0)} = \omega_{0K} - \omega_{0I}, && \omega_3^{(0)} = \omega_{0I} - \omega_{0K} = -\omega_2^{(0)}. \end{aligned} \tag{2.19}$$

In a similar manner, the components of $A_p^{(1)}$ and $A_p^{(2)}$ are calculated to be

$$\begin{aligned} &A_1^{(1)} = \alpha K_+ I_z, \quad && A_2^{(1)} = \alpha K_z I_+, && A_1^{(2)} = (\alpha/2)K_+ I_+, \\ &\omega_1^{(1)} = \omega_{0K}, && \omega_2^{(1)} = \omega_{0I}, && \omega_1^{(2)} = \omega_{0K} + \omega_{0I}. \end{aligned} \tag{2.20}$$

Again the components $A_p^{(-1)}$ and $A_p^{(-2)}$ are the Hermitian conjugates of $A_p^{(1)}$ and $A_p^{(2)}$ respectively, where $\omega_p^{(-q)} = -\omega_p^{(q)}$.

Replacing the expression for $\mathcal{H}_1$ in Eq. (2.9) by [2.17], we find

$$\mathcal{A}_Q = \sum_{q,q',p,p'} e^{i(w_p^{(q)}+w_{p'}^{(q')})t}[A_{p'}^{(q')},[A_p^{(q)},Q]]\int_0^\infty d\tau \overline{F^{(q)}(t)F^{(q')}(t-\tau)}e^{-i\omega_{p'}^{(q\prime)}\tau}. \tag{2.21}$$

According to Eq. (2.7), the density matrix would be time independent if $\tilde{\mathcal{H}}_1$ did not exist, and since $\tilde{\mathcal{H}}_1$ is a small perturbation, the variation of $\tilde{\rho}$ with time is slow. The effects on $\tilde{\rho}$ of those terms in Eq. (2.21) with a rapidly varying exponential $(w_p^{(q)} + w_{p'}^{(q')}) \neq 0$ should be negligible compared with those terms for which $(w_p^{(q)} + w_{p'}^{(q')}) = 0$ [54]. In evaluating $\mathcal{A}_Q$, this will allow us to neglect many of the terms in the above summation. We also assume, for simplicity, that the autocorrelation function $\overline{F^{(q)}(t)F^{(q')}(t-\tau)} = \delta_{q,-q'}\overline{F^{(q)}(t)F^{(-q)}(t-\tau)}$, an assumption realized in the cases presented in this thesis.

Furthermore, the imaginary part of the integral in Eq. (2.21) does not add to the relaxation rate of $\langle\tilde{Q}\rangle$ [54] and can be neglected. As a consequence, we can replace the integral in Eq. (2.21) with half the spectral density $J_q(\omega_p^{(q)})$, where

$$J_q(\omega_{p'}^{(q)}) = 2\int_0^\infty \overline{F^{(q)}(t)F^{(q)*}(t+\tau)}\cos\omega_{p'}^{(q)}\tau d\tau. \tag{2.22}$$

The spectral density is proportional to the power available to excite spin transitions caused by random motions of the lattice [55]. With the above discussed replacements, Eq. (2.17) is reduced to

$$\mathcal{A}_Q = \frac{1}{2}\sum_{q,p,p'} e^{i(w_p^{(q)}+w_{p'}^{(q')})t} J_q(\omega_{p'}^{(q)})[A_{p'}^{(-q)},[A_p^{(q)},Q]]. \tag{2.23}$$

where again the non-secular terms can be neglected. We can now calculate $d\langle\tilde{Q}\rangle/dt$ by simply evaluating the spectral densities $J_q(\omega_p^{(q)})$ and computing the various commutators in Eq. (2.23) with the use of the operators $A_p^{(q)}$ given in Eq. (2.19) and (2.20).

2.3.1 Evolution of ^{129}Xe Polarization

The ^{129}Xe polarization is twice the expectation value of the operator K_z. By taking K_z as Q in Eq. (2.8) we find the evolution of $\tilde{K}_z$ with time (under dipolar coupling in a static field) is

$$\frac{d\langle\tilde{K}_z(t)\rangle}{dt} = -\mathrm{tr}\{\mathcal{A}_{K_z}(\tilde{\rho}-\rho_0)\}, \tag{2.24}$$

where $\mathcal{A}_{K_z}$ is calculated from above values of $A_p^{(q)}$ to be

$$\begin{aligned}\mathcal{A}_{K_z} &= \frac{\alpha^2}{72}J^{(0)}(\omega_{0K}-\omega_{0I})[K_-I_+,[K_+I_-,K_z]]+h.c.\\ &+\frac{\alpha^2}{2}J^{(1)}(\omega_{0K})[K_-I_z,[K_+I_z,K_z]]+h.c.\\ &+\frac{\alpha^2}{8}J^{(2)}(\omega_{0K}+\omega_{0I})[K_-I_-,[K_+I_+,K_z]]+h.c.,\end{aligned} \tag{2.25}$$

where the abbreviation h.c. stands for the Hermitian conjugate. In addition to computing the various commutators in Eq. (2.26), we employ the following relationship

$$\langle K_x^2\rangle = \langle K_y^2\rangle = \langle K_z^2\rangle = \frac{K(K+1)}{3}; \quad \langle I_x^2\rangle = \langle I_y^2\rangle = \langle I_z^2\rangle = \frac{I(I+1)}{3}, \tag{2.26}$$

which is always exactly true for spin-1/2 particles, like ^{129}Xe and ^{1}H, but only approximately true for particles with spin greater than 1/2 when the polarization is very low. Therefore we find

$$\frac{d\langle\tilde{K}_z(t)\rangle}{dt} = -\varrho_K^{KI}(\langle\tilde{K}_z(t)\rangle - K_0) - \sigma_{KI}(\langle\tilde{I}_z(t)\rangle - I_0), \tag{2.27}$$

where $2K_0$ and $2I_0$ are the ^{129}Xe and proton polarizations in thermal equilibrium with the surrounding lattice. The coupling constants, ϱ_K^{KI} and σ_{KI}, are given by

$$\begin{aligned}\varrho_K^{KI} &= \gamma_I^2\gamma_K^2\hbar^2 I(I+1)\left\{\frac{1}{12}J^{(0)}(\omega_{0K}-\omega_{0I})+\frac{3}{2}J^{(1)}(\omega_{0K})\right. \\ &\quad \left.+\frac{3}{4}J^{(2)}(\omega_{0K}+\omega_{0I})\right\}, \qquad (2.28)\\ \sigma_{KI} &= \gamma_I^2\gamma_K^2\hbar^2 K(K+1)\left\{-\frac{1}{12}J^{(0)}(\omega_{0K}-\omega_{0I})+\frac{3}{4}J^{(2)}(\omega_{0K}+\omega_{0I})\right\}. \qquad (2.29)\end{aligned}$$

Furthermore, $\langle\tilde{K}_z\rangle$ can be replaced by $\langle K_z\rangle$ and $\langle\tilde{I}_z\rangle$ by $\langle I_z\rangle$ in the above equations because both K_z and I_z commute with $\mathcal{H}_0=(\omega_{0K}K_z+\omega_{0I}I_z)$.

To evaluate the coupling constants ϱ_K^{KI} and σ_{KI}, we must analyze the spectral density functions $J^{(0)}(w)$, $J^{(1)}(w)$, and $J^{(2)}(w)$. The correlation function $\overline{F^{(q)}(t)F^{(q)*}(t+\tau)}$ is assumed to be of the form $\langle F^{(q)}(t)F^{(q)*}(t)\rangle\exp(-|\tau|/\tau_c)$ [56], where τ_c is the correlation time. Therefore, from Eq. (2.22), $J^{(q)}(\omega)$ becomes

$$\begin{aligned}J^{(q)}(\omega) &= \langle F^{(q)}(t)F^{(q)*}(t)\rangle\left(2\int_0^\infty\cos(w\tau)e^{-\tau/\tau_c}d\tau\right)\\ &= \langle F^{(q)}(t)F^{(q)*}(t)\rangle\frac{2\tau_c}{1+\omega^2\tau_c^2} \qquad (2.30)\end{aligned}$$

The dependence of the spectral density on ω shows that frequencies smaller than $1/\tau_c$ are present in the sample, but frequencies larger than $1/\tau_c$ are few. These frequencies supply the necessary energy for the observed spin transitions to occur. To complete the calculation of the spectral densities, we determine the values of $\langle F^{(q)}(t)F^{(q)*}(t)\rangle$, using Eq. (2.14), to be

$$\begin{aligned}\langle F^{(0)}(t)F^{(0)*}(t)\rangle &= \left\langle\frac{(1-3\cos^2\theta)^2}{r^6}\right\rangle_{4\pi}=\frac{4}{5}\frac{1}{r^6}\\ \langle F^{(1)}(t)F^{(1)*}(t)\rangle &= \left\langle\frac{\sin^2\theta\cos^2\theta}{r^6}\right\rangle_{4\pi}=\frac{2}{15}\frac{1}{r^6} \qquad (2.31)\\ \langle F^{(2)}(t)F^{(2)*}(t)\rangle &= \left\langle\frac{\sin^4\theta}{r^6}\right\rangle_{4\pi}=\frac{8}{15}\frac{1}{r^6}.\end{aligned}$$

The dependence of the spectral density on ω, and therefore on the magnetic field since ω_{0K} and ω_{0I} are proportional to H_0, is most apparent in the interaction of gaseous or liquid ^{129}Xe with surface protons because τ_c tends to be quite long, on the order of microseconds. Figure 4.5 shows quite clearly the Lorentzian-like behavior of the ^{129}Xe relaxation rate with magnetic field. The field-dependent ^{129}Xe relaxation

rate is given by ϱ_K^{KI} (for now we ignore the second term on the right hand side of Eq. (2.27) since the ^{129}Xe polarization is orders of magnitude bigger than the ^{1}H polarization while ϱ_K^{KI} and σ_{KI} are on the same order of magnitude). By substituting the above calculated spectral densities into the expression (2.28) for ϱ_K^{KI}, we find

$$\varrho_K^{KI} = \frac{1}{T_1} = \frac{1}{10T_0}\left(\frac{1}{1+(\omega_{0K}-\omega_{0I})^2\tau_c^2} + \frac{3}{1+\omega_{0K}^2\tau_c^2} + \frac{6}{1+(\omega_{0K}+\omega_{0I})^2\tau_c^2}\right) \quad (2.32)$$

where $1/T_0$, the ^{129}Xe relaxation rate at zero field, is

$$\frac{1}{T_0} = \frac{4}{3}I(I+1)\frac{\gamma_K^2\gamma_I^2\hbar^2}{r^6}\tau_c. \quad (2.33)$$

In some cases, the experimental data needed to be fit to more than one expression of the form in (2.32) to account for multiple correlation times.

2.3.2 Evolution of ^{1}H Polarization

An identical equation and coupling constants can be obtained for the operator I_z by interchanging the letters K and I in Eq. (2.27), (2.28), and (2.29). As a consequence, we can write the coupled equations

$$\frac{d\langle K_z(t)\rangle}{dt} = -\varrho_K^{KI}(\langle K_z(t)\rangle - K_0) - \sigma_{KI}(\langle I_z(t)\rangle - I_0), \quad (2.34)$$

$$\frac{d\langle I_z(t)\rangle}{dt} = -\varrho_I^{IK}(\langle I_z(t)\rangle - I_0) - \sigma_{IK}(\langle K_z(t)\rangle - K_0), \quad (2.35)$$

where σ_{IK} and σ_{KI} are known as cross-relaxation rates. These two cross-relaxation rates are equal for equal number densities of ^{129}Xe and protons given the fact that ^{129}Xe and protons are both spin-1/2 particles (see Eq. (2.28) and (2.29)). More generally, the cross-relaxation rate σ_{KI} of ^{129}Xe due to protons is proportional to the ^{1}H number density N_I and similarly, the cross-relaxation rate σ_{IK} of protons due to ^{129}Xe is proportional to the ^{129}Xe number density N_K. Therefore, the two cross-relaxation rates are related by

$$\sigma_{KI} = \frac{N_I}{N_K}\sigma_{IK}. \quad (2.36)$$

2.4 Relaxation with ^{1}H Dissolved in Liquid Xe

In order to describe the system of hydrocarbons dissolved in liquid Xe we must include the other sources of relaxation to ^{129}Xe and to ^{1}H besides their dipolar coupling to each other. This can be done by replacing ϱ_K^{KI} in Eq. (2.34) by ϱ_K and ϱ_I^{IK} in Eq. (2.35) by the ϱ_I, where the ^{129}Xe autorelaxation rate ϱ_K sums over all the ^{129}Xe relaxation mechanisms including a significant contribution from ϱ_K^{KI}, and the proton autorelaxation rate ϱ_I sums over all the ^{1}H relaxation mechanisms. The proton autorelaxation rate ϱ_I is dominated by interaction with other protons while the rate ϱ_I^{IK} from dipole-dipole coupling to ^{129}Xe makes a negligible contribution.

The equations governing the two spin system can be written in matrix notation and a solution of the form $(\langle K_z(t)\rangle - K_0, \langle I_z(t)\rangle - I_0) = \left(C_K e^{\lambda t}, C_I e^{\lambda t}\right)$ can be assumed so that

$$\lambda \begin{pmatrix} C_K \\ C_I \end{pmatrix} = \begin{pmatrix} -\varrho_K & \sigma_{KI} \\ \sigma_{IK} & -\varrho_I \end{pmatrix} \begin{pmatrix} C_K \\ C_I \end{pmatrix} \tag{2.37}$$

Furthermore, as justified in Chapter 5 for the system in which molecules are dissolved in liquid Xe, we assume that

$$\varrho_I \gg \varrho_K, \sigma_{KI}, \sigma_{IK}. \tag{2.38}$$

We solve for the eigenvalues λ_1 and λ_2 and their corresponding eigenvectors $\mathbf{X}_1$ and $\mathbf{X}_2$ for the matrix equation (2.37) and approximate them, using the above assumption, as

$$\lambda_1 = -\varrho_I, \quad \mathbf{X}_1 = C_1 \begin{pmatrix} \sigma_{KI}/\varrho_I \\ 1 \end{pmatrix}; \quad \lambda_2 = -\varrho_K, \quad \mathbf{X}_2 = C_2 \begin{pmatrix} -\varrho_I/\sigma_{IK} \\ 1 \end{pmatrix} \tag{2.39}$$

where C_1 and C_2 are constants to be determined by intial conditions.

2.4.1 Laser-polarized Liquid Xe

When a solute with thermal-equilibrium polarization is dissolved at time t=0 into laser-polarized liquid Xe, we can take the initial conditions as

$$\langle K_z(0)\rangle - K_0 = \langle K_z(0)\rangle, \qquad \langle I_z(0)\rangle - I_0 = 0, \tag{2.40}$$

where $\langle K_z(0)\rangle - K_0$ has been approximated as $\langle K_z(0)\rangle$ since $\langle K_z(0)\rangle$ is five orders of magnitude larger than K_0 with our experimental conditions of 200 K and 14 kG. With these initial conditions, and recognizing that $\sigma_{KI}\sigma_{IK}/\varrho_I^2 \ll 1$, the solution to Eq. (2.37) becomes

$$\begin{pmatrix} \langle K_z(t)\rangle - K_0 \\ \langle I_z(t)\rangle - I_0 \end{pmatrix} = \langle K_z(0)\rangle \left[\begin{pmatrix} 0 \\ \sigma_{IK}/\varrho_I \end{pmatrix} e^{-\varrho_I t} + \begin{pmatrix} 1 \\ -\sigma_{IK}/\varrho_I \end{pmatrix} e^{-\varrho_K t} \right] \quad (2.41)$$

Thus the initial rise of the solute polarization is governed by the ^{1}H autorelaxation rate ϱ_I while its decay in polarization, along with the decay of the ^{129}Xe polarization, is governed by the ^{129}Xe autorelaxation rate ϱ_K. When $t \gg 1/\varrho_I$ one can see that

$$\langle I_z(t)\rangle - I_0 = -\frac{\sigma_{IK}}{\varrho_I}(\langle K_z(t)\rangle - K_0) \quad (2.42)$$

However, it is difficult to measure σ_{IK} independently. We know from Eq. (2.36) that $\sigma_{KI} = \frac{N_I}{N_K}\sigma_{IK}$. Furthermore we can show that in the fast motion limit $\omega\tau_c \ll 1$ the spectral density functions are frequency-independent, i.e., $J^{(q)}(w) = J^{(q)}(0)$, and that

$$\sigma_{KI} = \frac{\varrho_K^{KI}}{2}. \quad (2.43)$$

To first approximation, it is possible to measure ϱ_K^{KI} since it is a significant part of the ^{129}Xe autorelaxation rate ϱ_K (see Chapter 4). Therefore, in Eq. (2.42) we replace σ_{IK} by $(N_K/N_I)(\varrho_K^{KI}/2)$ to write

$$\langle I_z(t)\rangle - I_0 = -\frac{N_K}{N_I}\frac{\varrho_K^{KI}}{2\varrho_I}(\langle K_z(t)\rangle - K_0) \quad (2.44)$$

We are justified in using Eq. (2.43) to make the above replacement because we are well within the the fast motion limit at our operating magnetic field of 14 kG, assuming a typical τ_c of a picosecond for the interaction of ^{129}Xe and ^{1}H on molecules dissolved in liquid Xe.

2.4.2 Thermally Polarized Liquid Xe

While ϱ_K is easily measured from the decay of both the ^{129}Xe and ^{1}H polarizations, ϱ_I is difficult to measure from the very rapid rise ($\approx$ 10 s) of the ^{1}H polarization. Moreover, it is impossible to assign an exact t=0 when the solute has been dissolved

in the liquid Xe because the hyperpolarized ^{129}Xe liquid and thermally polarized solvent are not shaken together. The Xe is initially frozen on top of the also frozen solvent and the polarization transfer starts as soon as they begin to thaw and mix uncontrollably. However, it is possible to measure ϱ_I by waiting until the ^{129}Xe (and therefore also ^{1}H) polarization reaches its equilibrium value, and then tipping the ^{1}H polarization by $\pi/2$. Therefore taking

$$\langle K_z(0)\rangle - K_0 = 0 \tag{2.45}$$

$$\langle I_z(0)\rangle - I_0 = -I_0 \tag{2.46}$$

as the intial conditions, we find that

$$\begin{pmatrix} \langle K_z(t) - K_0\rangle \\ \langle I_z(t) - I_0\rangle \end{pmatrix} = I_0 \left[\begin{pmatrix} -\sigma_{KI}/\varrho_I \\ -1 \end{pmatrix} e^{-\varrho_I t} + \begin{pmatrix} \sigma_{KI}/\varrho_I \\ (-\sigma_{KI}\sigma_{IK})/\varrho_I^2 \end{pmatrix} e^{-\varrho_K t} \right] \tag{2.47}$$

In the limit $\sigma_{KI}, \sigma_{IK} \ll \varrho_I$, the above solution shows that the ^{129}Xe polarization is not affected by the pulse and that, after the pulse, the relaxation of the ^{1}H spin I back towards thermal equilibrium is completely dominated by ϱ_I. Therefore ϱ_I can be measured by monitoring this decay toward thermal equilibrium.

2.5 Relaxation with a Rotating Field

If, in addition to a static field, we apply a rotating magnetic field at the ^{1}H Larmor frequency the Hamiltonian $\hbar\mathcal{H}$ can be written as

$$\mathcal{H} = \omega_{0K} K_z + \omega_{0I} I_z + \mathcal{H}_{rf} + \mathcal{H}_{dd} \tag{2.48}$$

where

$$\mathcal{H}_{rf} = \omega_{1I}(I_x \cos\omega_{0I} t + I_y \sin\omega_{0I} t) \tag{2.49}$$

and $\mathcal{H}_{dd}$ describes the dipole-dipole interaction as in Eq. (2.11). The ^{1}H Rabi frequency is $\omega_{1I} = -\gamma_I H_1$, where H_1 is the magnitude of the rotating field. Transforming to the rotating frame,

$$\tilde{\rho} = e^{i(\omega_{0K}K_z + \omega_{0I}I_z)t} \rho e^{-i(\omega_{0K}K_z + \omega_{0I}I_z)t}, \tag{2.50}$$

$$\tilde{\mathcal{H}}_{rf} + \tilde{\mathcal{H}}_{dd} = e^{i(\omega_{0K}K_z + \omega_{0I}I_z)t} (\mathcal{H}_{rf} + \mathcal{H}_{dd}) e^{-i(\omega_{0K}K_z + \omega_{0I}I_z)t}, \tag{2.51}$$

and the Liouville equation, Eq. (2.2), becomes

$$\frac{1}{i}\frac{d\tilde{\varrho}}{dt} = -[\tilde{\mathcal{H}}_{rf} + \tilde{\mathcal{H}}_{dd}, \tilde{\varrho}]. \tag{2.52}$$

Using the relationships [57]

$$e^{iI_z\phi} I_x e^{-iI_z\phi} = I_x \cos\phi - I_y \sin\phi \tag{2.53}$$
$$e^{iI_z\phi} I_y e^{-iI_z\phi} = I_x \sin\phi + I_y \cos\phi. \tag{2.54}$$

we see that $\tilde{\mathcal{H}}_{rf} = \omega_{1I} I_x$. We can then transform into the doubly rotating frame to get rid of the rapid precession due to H_1 by using the transformations

$$\hat{\varrho} = e^{i\omega_{1I} I_x} \tilde{\rho} e^{-i\omega_{1I} I_x} \tag{2.55}$$
$$\hat{\mathcal{H}}_{dd} = e^{i\omega_{1I} I_x} \tilde{\mathcal{H}}_{dd} e^{-i\omega_{1I} I_x} \tag{2.56}$$

to further reduce the Liouville equation to

$$\frac{1}{i}\frac{d\hat{\rho}}{dt} = -\left[\hat{\mathcal{H}}_{dd}, \hat{\rho}\right]. \tag{2.57}$$

From this reduced Liouville equation, we can proceed as we did previously to find that

$$\frac{d\langle\hat{Q}\rangle}{dt} = -\mathrm{tr}\{\mathcal{A}_Q(\hat{\rho} - \hat{\rho}_0)\} \tag{2.58}$$
$$\mathcal{A}_Q = \frac{1}{2}\sum_{q,p,p'} e^{i(w_p^{(q)} + w_{p'}^{(q')})t} J_q(\omega_{p'}^{(q)})[A_{p'}^{(-q)}, [A_p^{(q)}, Q]]. \tag{2.59}$$

where $\langle\hat{Q}\rangle$ is defined to be $\mathrm{tr}\{\hat{\rho}Q\}$ and where $F^{(q)}$ are as in Eq. (2.14) and $A_p^{(q)}$ and their corresponding $\omega_p^{(q)}$ are now defined from the distinct transitions between states of the system due to $\hat{\mathcal{H}}_{dd}$,

$$\hat{\mathcal{H}}_{dd} = \sum_{q,p} F^{(q)}(t) A_p^{(q)} e^{i\omega_p^{(q)} t}. \tag{2.60}$$

All that is required to determine the time evolution of $\hat{Q}$ is to calculate the commutators in Eq. (2.59), because the spectral densities $J(\omega)$ are the same as when the rotating field was absent (see Eq. (2.30) and (2.32)). As in the previous section, the transformation of $A^{(0)}$ of $\mathcal{H}_{dd}$ into the rotating frame yields

$$\tilde{A}^{(0)} = -\frac{2}{3}\alpha K_z I_z + \frac{1}{6}\alpha K_+ I_- e^{i(\omega_{0K} - \omega_{0I})t} + \frac{1}{6}\alpha K_- I_+ e^{-i(\omega_{0K} - \omega_{0I})t} \tag{2.61}$$

Before transforming into the doubly rotating frame, it is necessary to change the definition of the raising and lowering operators because the ^{1}H magnetization is now quantized in the x-direction. We therefore introduce

$$I'_+ = I_y + iI_z \tag{2.62}$$

$$I'_- = I_y - iI_z \tag{2.63}$$

With this change of operators and by transforming into the doubly rotating frame, we find that

$$\begin{aligned}\hat{A}^{(0)} &= e^{i\omega_{1I}I_x}\tilde{A}^{(0)}e^{-i\omega_{1I}I_x} \\ &= \left(i\frac{\alpha}{3}K_zI'_+e^{i\omega_{1I}t} + \frac{\alpha}{6}K_+I_xe^{i(\omega_{0K}-\omega_{0I})t}\right. \\ &\quad \left. -i\frac{\alpha}{12}K_+I'_+e^{i(\omega_{0K}-\omega_{0I}+\omega_{1K})t} - i\frac{\alpha}{12}K_+I'_-e^{i(\omega_{0K}-\omega_{0I}-\omega_{1I})}\right) + h.c.\end{aligned} \tag{2.64}$$

From this expression for $\hat{A}^{(0)}$ one finds the eight $A_p^{(0)}$ and corresponding $\omega_p^{(0)}$. For instance, $A_1^{(0)} = i\frac{\alpha}{3}K_zI'_+$ and $\omega_1^{(0)} = \omega_{1I}$. The other values of $A_p^{(q)}$ can be calculated in a similar manner to $A_p^{(0)}$.

We are interested in finding out how the ^{129}Xe relaxation rate is affected by this rf applied at the ^{1}H Larmor frequency. Therefore we take K_z as Q. Because K_z commutes with both $\omega_{0K}K_z + \omega_{0I}I_z$ and with $\omega_{1I}I_x$,

$$\langle\hat{K}_z\rangle = \langle K_z\rangle \tag{2.65}$$

which means that whatever time dependence we are calculating for K_z should be measurable in the laboratory frame. In calculating the commutators in Eq. (2.59), we use again the relationship for a spin-1/2 particle that $\langle K_i^2\rangle = K(K+1)/3$, and we assume that $\langle K_z\rangle \gg \langle S_x\rangle, K_0$. We therefore approximate the time derivative of $\langle K_z\rangle$ as

$$\frac{d\langle K_z\rangle}{dt} = \frac{1}{T_1}\langle K_z\rangle, \tag{2.66}$$

where the ^{129}Xe relaxation rate $1/T_1$ is

$$\begin{aligned}\frac{1}{T_1} &= \frac{1}{40T_0}\left[\frac{6}{1+(\omega_{1I}+\omega_{0K})^2\tau_c^2} + \frac{6}{1+(\omega_{1I}-\omega_{0K})^2\tau_c^2} + \right. \\ &\quad \frac{12}{1+(\omega_{0I}+\omega_{0K})^2\tau_c^2} + \frac{6}{1+(\omega_{0I}-\omega_{1I}+\omega_{0K})^2\tau_c^2} + \\ &\quad \frac{6}{1+(\omega_{0I}+\omega_{1I}+\omega_{0K})^2\tau_c^2} + \frac{1}{1+(\omega_{0I}+\omega_{1I}-\omega_{0K})^2\tau_c^2} + \\ &\quad \left.\frac{2}{1+(\omega_{0I}-\omega_{0K})^2\tau_c^2} + \frac{1}{1+(\omega_{0I}-\omega_{1I}-\omega_{0K})^2\tau_c^2}\right].\end{aligned} \tag{2.67}$$

The rate $1/T_0$ is the zero-field relaxation rate given by Eq. (2.33), the zero-field relaxation rate in the absence in any rf. In the limit as ω_{1I} goes to zero, the relaxation rate above reduces to the ^{129}Xe relaxation rate in the presence of only a static magnetic field as found in Eq. (2.32). One can see from the first term in the above equation that, if dipole-dipole coupling between ^{129}Xe and ^{1}H is a dominant relaxation mechanism, the ^{129}Xe relaxation rate is increased when $\omega_{1I} = -\omega_{0K}$. We calculated the effects on the ^{129}Xe relaxation rate of an rf applied at the proton Larmor frequency, looking for just such a signature of dipole-dipole coupling between ^{129}Xe and ^{1}H as this resonance condition provides.

A more general expression for the ^{129}Xe relaxation rate can be obtained for when the applied rf frequency is slightly detuned from the proton Larmor frequency. One can begin with an expression derived in Ref. [58] for the ^{129}Xe relaxation rate in the frame rotating with H_{eff} when two rotating magnetic fields are applied, one applied at a frequency ω_I close to the proton Larmor frequency ω_{0I} and the other applied at a frequency ω_K close to the ^{129}Xe Larmor frequency ω_{0K}.

$$\frac{1}{T_1} = \frac{1}{T_0} \sum_{\mu\nu\eta} \frac{\left[d^1_{1\mu}(\beta_K)\right]^2 \left[d^1_{\nu\eta}(\beta_I)\right]^2 C^2(121;\nu,\mu-\nu)}{1+(\eta\Omega_I + \nu\omega_I - \Omega_K - \mu\omega_K)^2\tau_c^2} \tag{2.68}$$

where the summation variables run between -1 to 1 and the Wigner d-functions ($d^1_{\nu\eta}(\beta_I)$ and $d^1_{1\mu}(\beta_K)$) and the Clebsch-Gordon coefficients ($C^2(121;\nu,\mu-\nu)$) can be found in Ref. [59]. The detuning enters through

$$\tan\beta_K = \frac{\omega_{1K}}{\omega_{0K}-\omega_K} \quad ; \qquad \Omega_K^2 = (\omega_{0K}-\omega_K)^2 + \omega_{1K}^2 \tag{2.69}$$

$$\tan\beta_I = \frac{\omega_{1I}}{\omega_{0I}-\omega_I} \quad ; \qquad \Omega_I^2 = (\omega_{0I}-\omega_I)^2 + \omega_{1I}^2. \tag{2.70}$$

where β_S is the angle between the laboratory z axis and the quantization axis of the rotating coordinate system for spin S and $|\gamma_S\Omega_S|$ is the magnitude of the effective field felt by spin S. The above equation for $1/T_1$ assumes that the coupling of ^{129}Xe to ω_I is negligible and that the coupling of ^{1}H to ω_K is also negligible.

However, with one only one rf applied, we can allow for both spins to couple to the same rf by taking $\omega_K = \omega_I = \omega_{rf}$. If we in addition assume that ω_{rf} is not close to the ^{129}Xe Larmor frequency, we find that the above expression (2.68) is reduced to

$$\frac{1}{T_1} = \frac{1}{T_0} \sum_{\nu\eta} \frac{\left[d^1_{\nu\eta}(\beta_I)\right]^2 C^2(121;\nu,1-\nu)}{1+(\eta\Omega_I + \nu\omega_{rf} - \omega_{0K})^2\tau_c^2} \tag{2.71}$$

If we go further to assume that the rf applied is exactly at the proton Larmor frequency then the above expression reduces to Eq. (2.67), as is expected.

Chapter 3

Experimental Methods

The study of the relaxation mechanisms of ^{129}Xe in the liquid phase and the study of its cross-relaxation to other nuclear species dissolved in the liquid Xe share many of the same experimental methods. This chapter describes those shared techniques: from the production of the large quantities of laser-polarized ^{129}Xe needed, to the NMR techniques, both pulsed and continuous, employed for the polarization measurements. These experiments would not be possible without the large non-equilibrium polarization of ^{129}Xe created through spin-exchange [60, 1, 61, 3, 62, 63] with optically-pumped Rb [64, 65]. Spin-exchange optical pumping has been described in detail in many places such as Ref. [4, 65] and remains an active area of research [66, 67]. Therefore it will not be described here.

A home-built pulsed nuclear magnetic resonance (NMR) spectrometer [68] was used at 14 kG and 200 K for the cross-relaxation studies to measure the enhancement of the solute spin species and its autorelaxation rate, in addition to the ^{129}Xe polarization and autorelaxation rate. The same spectrometer was used at 14 kG to measure the ^{129}Xe relaxation rate in pure liquid Xe as a function of temperature and cell surface. For fields $\leq$ 1 kG, the ^{129}Xe relaxation rate in pure liquid Xe was measured using a continuous wave NMR technique known as adiabatic fast passage (AFP). The ^{129}Xe relaxation rate was measured as a function of magnetic field, temperature, cell surface, and applied radio frequency (rf). AFP was also used in the cross-relaxation studies to determine the relative sign of the enhanced polarization of the solute spin species.

3.1 Production of Laser-Polarized ^{129}Xe

Driehuys [7] describes in detail the technique that we used to produce the large quantity of laser-polarized ^{129}Xe needed for both the liquid and cross-relaxation studies. This method used optically pumped Rb vapor to polarize the nucleus of ^{129}Xe through spin-exchange. A typical mixture of 1.5% Xe, 1% N_2, and 97.5% ^{4}He at 8.5 atm flowed through the optical pumping chamber (see Fig. 3.1). The Xe was of natural isotopic composition (26% ^{129}Xe), except for a few runs of the cross relaxation studies in which the Xe was enriched to 71% ^{129}Xe. The He pressure-broadened the Rb D1 absorption profile in order to absorb efficiently the broad spectral output of the 100 W AlGaAs diode laser array used in our experiment. The flow rate used, ∼300 scc/min, allowed for ^{129}Xe to be polarized to near saturation during the few minutes required to pass through the optical pumping chamber.

After leaving the optical pumping chamber, the gas mixture flowed through a cold trap, maintained at 77 K by a bath of liquid nitrogen. The laser-polarized Xe accumulated as solid dendritic crystals while the He and N_2 passed through and were vented into the room. Inside the liquid nitrogen, around the cold trap, were placed a pair of permanent magnets. The permanent magnets were held in place by an iron yoke which also served as a flux return. The permanent magnets provided a field of 1 kG, ensuring that the polarization lifetime of the laser-polarized Xe crystals was ∼3 hours [40]. With less than an hour accumulation, we routinely collected about a gram of polarized Xe ice in the cold trap. The production rate was somewhat smaller than that predicted by the flow rate. The liquid nitrogen level had to be kept low to prevent clogging of the cold finger. As a consequence, not all of the Xe was frozen out from the gas stream.

After being transferred to the measurement cells from the cold trap, the ^{129}Xe polarization was typically between 10% and 20%. The polarization was determined by comparison to NMR signals from both a cyclopentane sample and a thermal equilibrium sample of Xe enriched to 71% ^{129}Xe. We typically polarized the ^{129}Xe into the lower energy state to avoid masing during our NMR measurements. When we polarized it into the higher energy state, we observed mysteriously large losses of polarization upon application of NMR pulses to our hyperpolarized liquid samples. These losses disappeared when we polarized into the lower energy state.

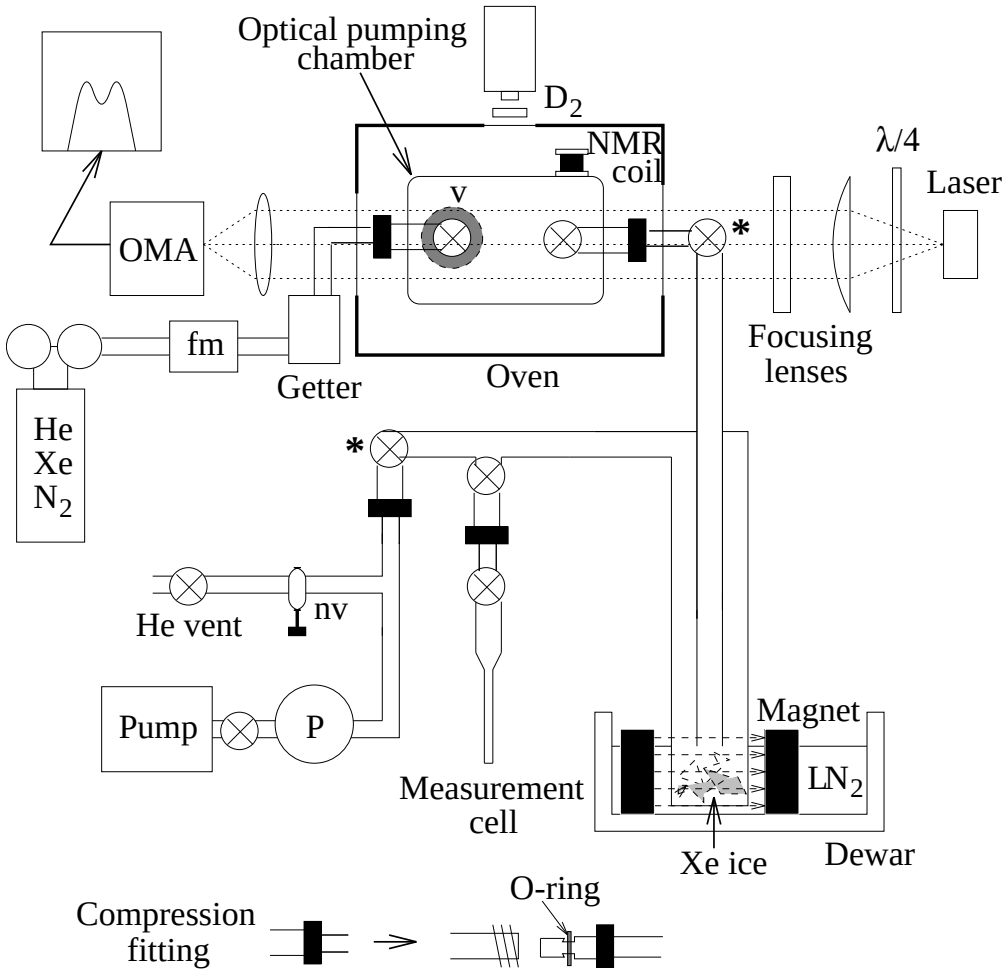

Figure 3.1: Laser-polarized ^{129}Xe production apparatus. A mixture of He, Xe, and N_2 at high-pressure flowed through a zirconium getter, a vaporizer **v** filled with Rb, and into the optical pumping chamber. The needle valve **nv** set the flow rate; the flowmeter **fm** monitored the flow rate. The pressure of the system was measured at **P**. Xe was frozen out between the pair of magnets immersed in liquid nitrogen, while He and N_2 continued through to be vented into the room. To determine the optimal temperature of the oven, the optical multi-channel analyzer **OMA** monitored the spectral profile of the light as it left the optical pumping chamber. NMR and D_2 fluorescence provided additional diagnostics. After accumulation, the starred valves were closed and the nearby compression fittings were disconnected so that the cold trap and measurement cell could be removed from the apparatus.

3.2 Transfer Techniques

The Xe ice accumulated in the cold trap was transferred to a detachable cell used for our measurements. Before accumulation of the laser-polarized Xe began, we attached

this measurement cell to the outlet of the cold trap and evacuated both the cell and cold trap to below a millitorr. After accumulation of the laser-polarized Xe was finished, we pumped on both the Xe ice in the cold trap and on our measurement cell in order to remove any remaining He and N_2 gas. The basic transfer method was to thaw the solid Xe from the cold trap into gas and refreeze this gas into our measurement cell. To ensure that the ^{129}Xe relaxation rate in the ice was negligible during the transfer, both the measurement cell and the cold trap needed to be in a magnetic field greater than 500 G [40].

In order to remove the cold trap and measurement cell to a field greater than 500 G, the starred valves in Fig. 3.1 were closed and their closest connections released. The connections were 1/4 inch compression fittings modified so that the O-ring sat in a groove (shown at the bottom of Fig. 3.1). With this modification, the connection could withstand the 8.5 atm operating pressure of the laser-polarized Xe production apparatus. It was easy to release these connections and lift out the whole cold trap, including the liquid nitrogen dewar and magnets, with our measurement cell still attached. The cold trap/measurement cell was then placed in the fringe field ($\geq$ 500 G) of the magnet in which the measurements would be taken. Then the solid Xe could be thawed into gas using a stream of hot air and concurrently the gas could be refrozen into our measurement cell using a small dewar of liquid nitrogen. The air heater was positioned far upstream from the Xe to prevent any ^{129}Xe depolarization from any magnetic fields the heater produced. The Xe often froze near the top of the measurement cell as seen in Fig. 3.2. After the transfer of laser-polarized Xe, the cell was sealed, detached from the cold trap, and placed inside our measurement apparatus. When the solid Xe warmed and liquified, the bubbling liquid was mixed as it flowed down toward the bottom of the cell. In this way our liquid samples started with a fairly uniform ^{129}Xe polarization. In addition, we found that there was negligible loss of ^{129}Xe polarization in going from the solid to the liquid Xe.

3.3 Oxygen Contamination in Liquid Xe

Oxygen contamination has plagued those researching liquid Xe [69, 44]. Hunt and Carr [44] found that it would take on the order of 10 ppm of oxygen to account for their observed relaxation rates in ^{129}Xe. Although the oxygen impurity of our gas mixture straight from the gas cylinder was on the ppm level, the mixture passed through a zirconium getter [70] rated to reduce the impurities to 100 ppb. The hot

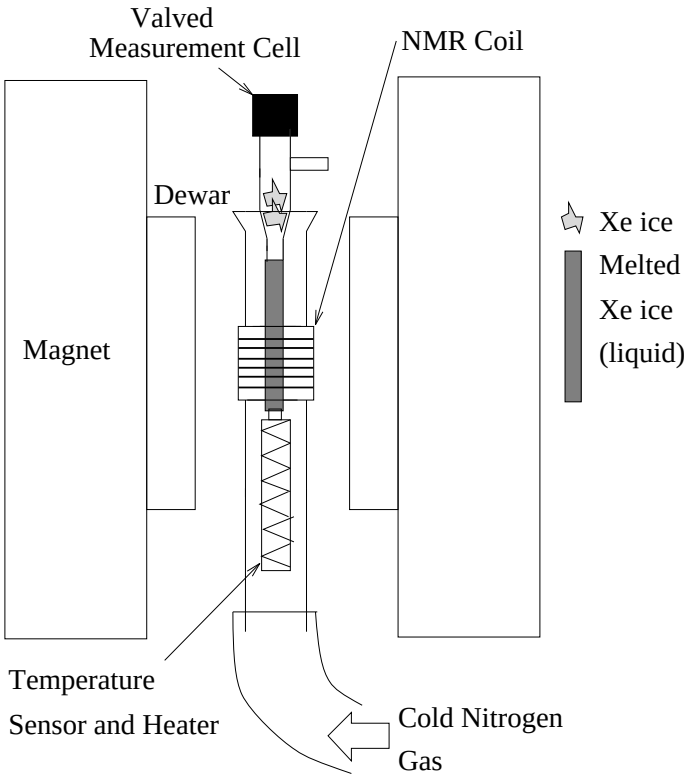

Figure 3.2: Simplified schematic of the NMR measurement apparatus. A valved cell containing Xe ice was inserted in a glass dewar where the ice was melted into liquid. A NMR coil at the bottom of the cell was used to measure the liquid ^{129}Xe signal. Cold nitrogen gas flowing through the dewar, together with a heater and temperature sensor positioned below the cell, provided temperature control.

Rb metal used for the spin-exchange optical pumping also acted as a getter [53]. The two getters should have ensured that the solid Xe accumulated in the cold trap contained less than a ppm level of oxygen. As mentioned above, we evacuated our measurement cell and pumped on the collected Xe solid before transferring the Xe to the measurement cell. This procedure also should have kept the impurity below a ppm in the liquid. The reproducible results, at 14 kG where the liquid T_1 was not very sensitive to surfaces, gave the most convincing evidence of the absence of oxygen.

3.4 Cell Parameters/Preparation

3.4.1 Liquid Xe Cells

All of our cells were made of glass tubing whose specifications gave allowable pressures up to 40 atm. Liquid Xe has a significant vapor pressure, ranging from 0.81 atm at 161.4 K (the triple point) to 57 atm at 289.7 K (the critical point) [42]. We therefore restricted our temperature range from close to the triple point to 240 K. The bottom of the cells were made with long pieces of small tubing (1 mm to 4 mm in diameter) so that a long column of liquid, typically 7 – 10 cm, could be achieved. This long column of liquid was needed to ensure that relaxation in the vapor phase did not influence our liquid-phase ^{129}Xe T_1 measurements. We took our measurements near the bottom of the column of liquid. See Fig. 3.2 for the pulsed NMR set-up and Fig. 3.3 for the AFP set-up. The diffusion constants of the liquid ranges from 1.8×10^{-5} cm^2/s at 165 K to 6.4×10^{-5} cm^2/sec at 240 K [51]. Therefore during the hour a typical experiment lasted, a Xe atom would have only been able to diffuse about 0.5 cm into the liquid from the gas at the warmest temperature studied. This characteristic diffusion length was much shorter that the 2 to 6 cm typically separating the liquid/gas interface from the top of the measurement coil.

The densities of the saturated vapor and liquid are dependent only on the temperature and are tabulated in [42]. The amount of liquid Xe in the measurement cell is determined by these densities, the cell volume, and the total quantity of Xe. Because of the significant vapor pressure of Xe, a large fraction of Xe in a cell would be in the gas instead of the liquid. By reducing the size of the cell to 2 – 4 cm^3, we increased the fraction of the Xe found in the liquid so that the liquid heights mentioned above could be obtained. The small cell volume meant that we would have had as many as 90 atm of gaseous Xe if the cell were to warm up to room temperature. Therefore we were careful to keep our cells cold and release the Xe after we finished our measurements.

In order to investigate whether the cell surface affected the ^{129}Xe relaxation rate in the liquid, we examined cells with different surfaces. Most cells were left with bare pyrex as their surface. However one cell was filled with a 0.3 molar solution of gadolinium nitrate in water and heated to 90°C for over 40 hours. The cell was then dried and evacuated, leaving behind the gadolinium ions on the surface. The Gd^{3+} ion has a large effective magnetic moment of 8.0 Bohr magnetons [71] which should couple strongly to ^{129}Xe.

3.4.2 Cross-relaxation Samples

In the cross-relaxation studies, the solute was put in the measurement cell first and the Xe was added later. The solute, placed inside the measurement cell, was purified by a combination of vacuum boiling and freeze-pump-thaw cycles to remove any dissolved oxygen. After this purification, the mass of the solute was measured before the cell was attached to the cold trap of the apparatus shown in Fig. 3.1. During the accumulation process of laser-polarized ^{129}Xe, the measurement cell's valve was closed to the cold trap. After accumulation, the transfer procedure to get the solid Xe from the cold trap to the measurement cell was exactly as described above. During the transfer, because the measurement cell was immersed in liquid nitrogen, the Xe froze out on top of the frozen solute. All of the solutes we explored, as well as Xe itself, have melting points between 160 and 180 K. Thus as the cell warmed to 200 K, the operating temperature used for the cross-relaxation experiments, the Xe and the solute both thawed and mixed together.

To quantify the cross-relaxation measurements, we needed to know the number densities of ^{129}Xe and the solute spin species in the solution. The amount of Xe in solution could be determined by measuring the the total mass of Xe in the cell and subtracting the mass of the vapor. Our cell volumes for the cross-relaxation studies were large, ~ 8 cm^3, in order that we might safely measure the mass of our samples, Xe and solute, after they had warmed up to room temperature. We determined that 0.32 ± 0.02 g of Xe was in the vapor for our samples at 200 K, with the balance in the solution. (Because the vapor pressures of the solutes we examined were 1 torr or less at 200 K, the amount of solute in the vapor was negligible.) By visually measuring the volume of the solution, the number densities of ^{129}Xe and solute spin species could be determined.

3.5 Temperature Control

The cross-relaxation studies were conducted at 200 K, while the pure liquid Xe studies were conducted between 165 to 240 K. The cell containing the sample was cooled in an evacuated glass dewar by flowing cold nitrogen gas from a nearby liquid nitrogen tank (see Fig. 3.2). A pressure regulator placed on the liquid output of the tank provided coarse control of the temperature. A Lake Shore model 520 cryogenic temperature controller produced the fine control. The controller monitored the temperature with a DT-471 diode sensor and regulated the current through a nichrome heater wire to

warm the nitrogen gas to the appropriate temperature. The heater wire was wrapped into two counterwound solenoids so that very little magnetic field was generated by the ~ 1 A dc heater current, and consequently our measurements were not affected. The temperature varied by less than 1 K from above the temperature sensor to within 3 cm of the top of the dewar so that the bottom 13 cm of the cell, including the entire column of liquid, was kept at the same temperature. The Lake Shore controller read the temperature $\sim 2°$C colder than what it really was inside the dewar and therefore we had to offset the set point on the Lake Shore controller by this amount. Because the liquid sample was cooled from below, convective mixing was ruled out; convective mixing otherwise might have contributed to a greater exchange with the gas. The cell valve was kept outside of the dewar because the valve made use of O-rings which contract when cold.

For a given sample of laser-polarized liquid Xe, after measuring the ^{129}Xe relaxation rate at a given temperature, if we changed the temperature to measure the ^{129}Xe relaxation rate at a new temperature we often did not get reliable relaxation rate results for the second temperature. The exchange between gas and the liquid as the sample came to the new equilibrium temperature probably resulted in an uneven distribution of polarization that, through diffusion, contributed unpredictably to the relaxation rate. In contrast, after measuring the ^{129}Xe relaxation rate at a given magnetic field, we could change the magnetic field to a new value and reliably measure the ^{129}Xe relaxation rate at that new field.

3.6 Adiabatic Fast Passage

3.6.1 Overview

For an adiabatic fast passage (AFP) experiment, the liquid Xe is placed in a dc field of $H_0\mathbf{k}$ produced by a large set of Helmholtz coils (≈ 2 ft in diameter). A small rotating rf field of strength H_1 and angular frequency ω_{rf} is applied perpendicularly to $H_0\mathbf{k}$ and kept on continuously during an AFP measurement. The principle of adiabatic fast passage is that the angle between the magnetization of the nuclear spins $\mathbf{M}$ and the effective field in the frame rotating with the rf

$$\mathbf{H_{eff}} = (H_0 + \omega_{rf}/\gamma)\ \mathbf{k} + H_1\ \mathbf{i} \tag{3.1}$$

remains constant (where γ is the gyromagnetic ratio of the nuclear spins). The angle between $\mathbf{H_{eff}}$ and $\mathbf{M}$ is practically zero when $\mathbf{H_0}$ is far from the resonant condition $H_0 = -\omega_{rf}/\gamma$. At resonance, the effective field is H_1 and therefore the angle between $\mathbf{H_1}$ and $\mathbf{M}$ is zero so that the nuclear spins rotate along with H_1. These nuclear spins can then be detected by a coil using Faraday's Law. The dc field H_0 is typically kept about 4 G off resonance (in our case 137 G) until it is time for a measurement. It is then ramped up through resonance and ramped back down through resonance to its original value, providing two AFP signals. After this field sweep, the magnetization of the spins is left pointed in the same direction as before the sweep of H_0 began. For a more detailed description of AFP see Abragam [54].

3.6.2 AFP Constraints

In an adiabatic *fast* passage experiment, H_0 must be swept sufficiently *fast* so that the effects of relaxation will be negligible during the time τ of passage through resonance

$$\tau \cong H_1 / \frac{dH_0}{dt} \ll T_{1\rho}^{\star}, \tag{3.2}$$

where $T_{1\rho}^{\star}$ is the effective polarization lifetime in the rotating frame. For *adiabatic* fast passage, the *adiabatic* condition places the additional requirement that the static field must be swept sufficiently *slowly* so that the ^{129}Xe spins can follow the effective magnetic field. This is especially of concern during the resonance condition when the spins feel an effective field of H_1, but this effective field is changing by dH_0/dt. The nuclear spins need to be able to precess many time around $\mathbf{H_1}$ in the time that it takes to change H_0 by order H_1

$$\frac{1}{H_1}\frac{dH_0}{dt} \ll \gamma H_1. \tag{3.3}$$

Rewriting Eq. (3.2) and Eq. (3.3) together:

$$\frac{1}{T_{1\rho}^{\star}} \ll \frac{1}{H_1}\frac{dH_0}{dt} \ll \gamma H_1. \tag{3.4}$$

Using a sweep rate of ~ 4 G/s and an H_1 of ~ 170 mG satisfies these constraints.

In order for amplitudes of the AFP signals to be a reliable measure of the ^{129}Xe polarization, the widths of the AFP signals must be rf-broadened, not dominated by field inhomogeneities [54]. For an H_0 of 141 G, the inhomogeneities in H_0 across

our measurement region were less than the H_1 of 170 mG (according to the specifications of our magnet). Moreover, the signal's width was experimentally observed to be linearly dependent on H_1 for $H_1 \geq 70$ mG. Therefore, the widths of our AFP peaks were determined solely by the strength of the rf and the amplitudes accurately reflected the ^{129}Xe polarization. After taking AFP measurements at appropriately spaced intervals, we could fit the amplitudes of the signals to

$$P(t) = P_0 \exp(-t/T_1) \tag{3.5}$$

and extract $1/T_1$, the polarization relaxation rate.

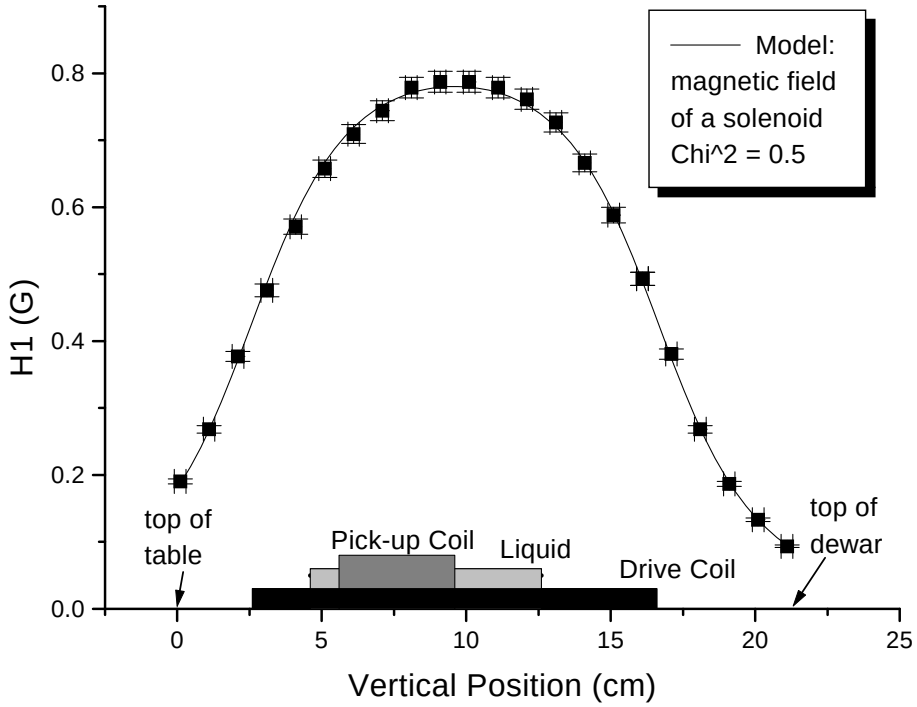

Figure 3.3: H_1 of the AFP drive coil. H_1, measured using a small Faraday coil, is fitted to the functional form of a magnetic field from a solenoid. The vertical positions of the liquid sample, the drive and pick-up coils are also shown.

In order to satisfy Eq. (3.4) for the entire column of liquid, two coils were used: a

large drive coil to apply rf to the spins and a small set of pick-up coils to detect their response to this rf. Figure 3.3 shows the relative vertical positions of the drive and pick-up coils, and where a liquid sample would typically have been placed. Figure 3.3 also shows the strength of the rf field as a function of vertical position. We detected only the nuclear spins towards the bottom of the liquid in order to isolate the liquid relaxation rate from any contribution from the gas/liquid interface. When we initially tried using a single small coil both to drive and to detect the spins, polarization was lost in the region (outside of the coil) where the AFP conditions were not met. Xe from this polarization-depleted region would later diffuse into the pick-up coil, appearing as a sudden increase in the ^{129}Xe relaxation rate.

Because our liquid height extended over a large region, one concern had been a significant contribution of inhomogeneities in both H_1 and H_0 to the relaxation rate in the rotating frame [30]

$$\frac{1}{T_{1\rho}^{\star}} = \frac{1}{T_{1\rho}} + D\left(\frac{|\nabla H_{0z}|^2}{H_1^2} + \frac{|\nabla H_{1\perp}|^2}{H_1^2}\right). \tag{3.6}$$

Where ∇H_{0z} is the field gradient of H_0 in the z direction and $\nabla H_{1\perp}$ is the field gradient of H_1 in the direction perpendicular to H_1. However, because of the small diffusion constant of liquid Xe, D $\sim 5 \times 10^{-5}$ cm^2/s, the contribution due to the field inhomogeneities turned out to be negligible compared to $1/\tau$. The intrinsic relaxation rate in the rotating frame of the liquid $1/T_{1\rho}$ was also negligible compared to $1/\tau$. We observed no significant loss in polarization during an AFP sweep. The AFP signal from when H_0 was swept up through resonance was repeatedly observed to be equal in amplitude to the AFP signal from when H_0 was swept down through resonance.

3.6.3 The AFP Probe: Signal Detection

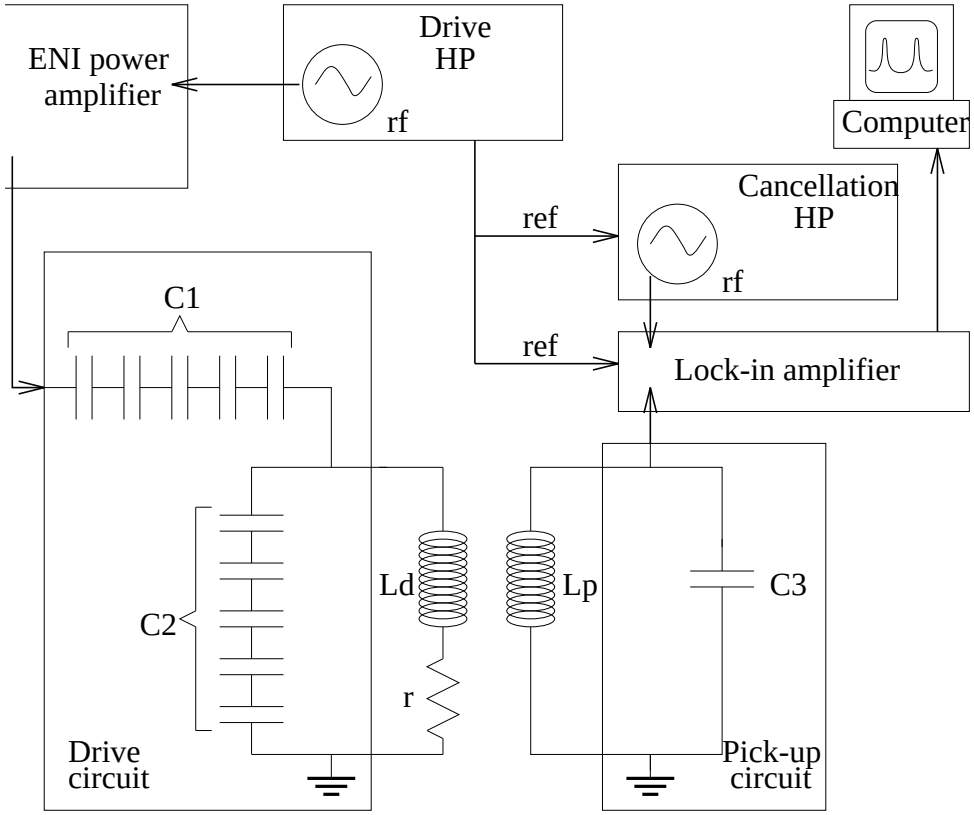

C_1	C_2	L_d	L_p	C_3
500 pF	1101 pF	520 μH	73 μH	13.9 nF

Figure 3.4: AFP detection scheme. The drive and the pick-up circuits both resonate at about 166 kHz, which corresponds to a resonant field of 141 G for ^{129}Xe. The drive coil provides the rf field and the pick-up coil detects the spin precession.

The signal of the Hewlett Packard 3325A function generator (drive HP), amplified first through the ENI power amplifier and afterwards through the resonant tank circuit, is applied across the liquid sample at the rf field H_1. The tank circuit consists of an inductive solenoid copper wire coil (the drive coil) and tuning capacitors chosen to resonate at a frequency $\nu_0 = \omega_{rf}/2\pi = 166$ kHz. The tank circuit (the drive coil

and C_2) plus coupling capacitor is used to match the impedance of the coil to the electronic devices, in this case the ENI amplifier. The output impedance of this power amplifier is nominally 50 Ω. The impedance of the drive tank circuit, together with the coupling capacitor, is given by

$$Z = \frac{rX_{C_2}^2 - i[r^2(X_{C_1} + X_{C_2}) + (X_{L_d} - X_{C_2})(X_{L_d}(X_{C_1} + X_{C_2}) - X_{C_1}X_{C_2})]}{r^2 + (X_{L_d} - X_{C_2})^2}, \quad (3.7)$$

where $X_{L_d} = \omega L_d$ and $X_{C_i} = 1/\omega C_i$ are the reactances for the drive coil and capacitors, respectively. This expression assumes that the mutual inductance of the drive coil and the pick up coils is negligible because the drive coil is perpendicular to the pick-up coils. This expression also assumes that the dominant source of power dissipation is due to the coil resistance r. Typically r is much smaller than the magnitude of all the other impedances, although it is important to remember that due to the skin effect, r depends on ω and is many times its dc value at large frequencies.

In order to obtain the maximum H_1 for a given voltage in V_{in}, it is necessary to obtain the maximum current through the coil and therefore through r. Using the relationship for the average power dissipated in the drive circuit,

$$P_{\text{dissipated}} = \frac{I_{\text{coil}}^2 r}{2} = \frac{V_{\text{in}}^2}{2}\frac{\text{Re}[Z]}{|Z|^2}, \quad (3.8)$$

it can be seen that the maximum current through the coil occurs when the imaginary part of the impedance is set to zero. Therefore, setting the imaginary part of Eq. (3.7) to zero, we obtain the resonance condition

$$\omega_0 = \frac{1}{\sqrt{L_d(C_1 + C_2)}}, \quad (3.9)$$

where terms proportional to r^2 have been neglected. The real part of Eq. (3.7) is

$$\text{Re}(Z) = \frac{rX_{C_2}^2}{(X_{L_d} - X_{C_2})^2} = \frac{r}{(1 - \omega^2 L_d C_2)^2} \quad (3.10)$$

and for $\omega = \omega_0$

$$\text{Re}(Z_0) = r\left(1 + \frac{C_2}{C_1}\right)^2 = \frac{\omega_0 L_d}{Q_0}(1 + \frac{C_2}{C_1})^2, \quad (3.11)$$

where Q_0, the intrinsic Q of the coil at ω_0, is equal to $\omega_0 L_d/r$. Q is readily measurable or calculated and $Q \approx 100$ is a reasonable order of magnitude for an rf coil [54]. After constructing the drive coil, C_1 and C_2 are chosen to meet the resonance condition

of Eq. (3.9) and to match the circuit's impedance at resonance to 50 Ω. Typically, these conditions provide only a rough guideline and some empirical work is needed to obtain a circuit with the correct frequency response.

The pick-up coil is part of a second tank-circuit tuned to resonate with the same frequency $\nu_0 = 166$ kHz. An emf $\mathcal{E}$ will be produced by spins precessing at ν_0 in the coil. The emf $\mathcal{E}$ will appear as a voltage equal to $Q_p\mathcal{E}$ across its terminals [54], where Q_p is the intrinsic Q of the pick-up coil. An Ithaco 3961B lock-in amplifier, referenced to the drive HP, then detects this voltage from the precessing spins and its output is read by a computer. Because we operated close to the specified upper frequency limit (200 kHz) of our lock-in amplifier, the signal gain for different lock-in scales was not uniform. Therefore, the ^{129}Xe relaxation rate was extracted from data taken using a single lock-in scale.

3.6.4 The AFP Probe: Noise Reduction

The main source of noise in the AFP signal was caused by rf leakage from the drive coil to the pick-up coils. The drive coil is placed perpendicularly to $\mathbf{H}_0$ in order that $\boldsymbol{\omega_0}$ be aligned with $\mathbf{H}_0$. The pair of pick-up coils were placed orthogonally to both $\mathbf{H}_0$ and the drive coil. This configuration helped to minimize the leakage of rf from the drive coil to the pick-up coils. The arrangement of components is shown in Fig. 3.5. The drive coil was wound around a plexiglass cylinder (7.5 cm in diameter) which rested on the table that the dewar comes through. The pair of pick-up coils were wound around a machined piece of teflon that fit tightly, with the aid of teflon tape, onto the dewar.

Initially, a large amount of noise was produced by the relative motion between the drive and pick-up coils. In order to minimize this source of noise we machined a pair of teflon pieces to fit snugly between the dewar and the plexiglass cylinder and another pair of teflon pieces to fit snugly between the dewar and the hole through the table. In this way, the dewar (and therefore the pick-up coils) could be held firmly in place with respect to the drive coil. Four nylon screws, screwed through the plexiglass cylinder and with rubber grommets glued to the end of them, are employed to keep the top of the dewar held in place. These four screws allowed for fine adjustment of the pick-up coils relative to the drive coil. Moreover, the two screws in the **i** direction provide especially sensitive control of the rf leakage between the coils. In theory, if we could get the drive coil and the pick-up coils perfectly orthogonal to each other there would be no rf leakage. However, cross-talk between the drive and pick-up circuits

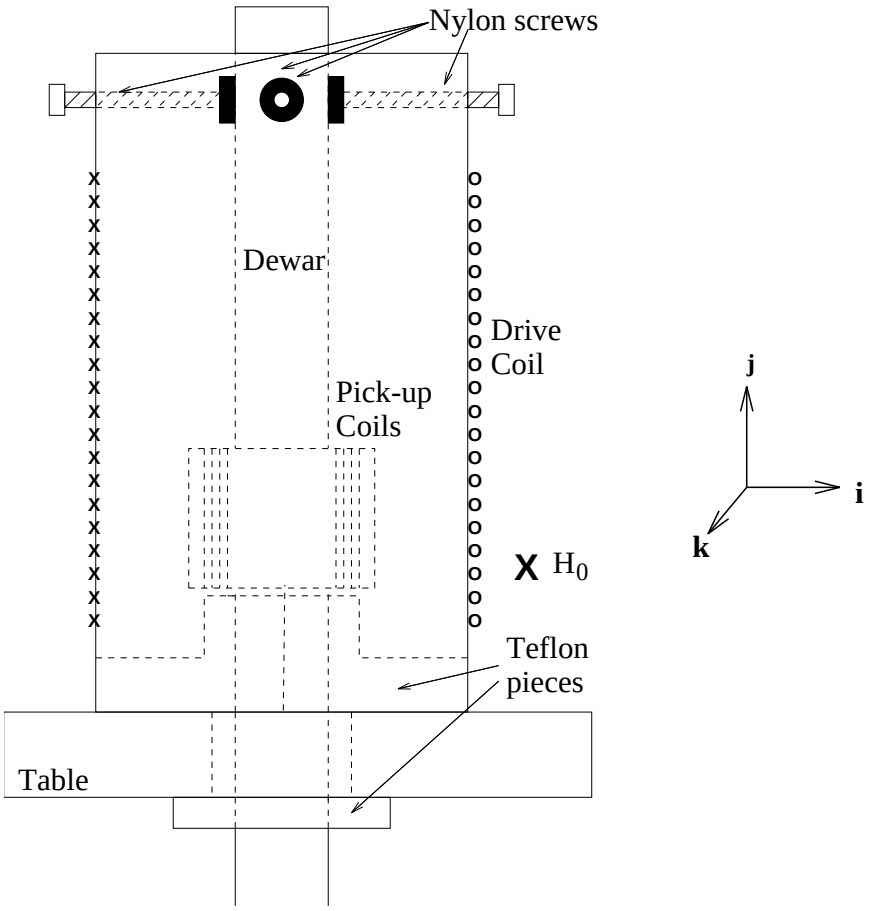

Figure 3.5: Dual-coil AFP probe. The teflon pieces stabilized both the dewar and drive coil. The nylon screws were used to adjust the relative position of the pick-up coils to the drive coil in order to reduce rf leakage.

also produced rf leakage. Separation of these circuits into two boxes and separating the BNC cables leading to the two coils helped greatly to cut down on this cross-talk.

A second method of noise reduction was to subtract off from the AFP signal a cancellation signal of the same amplitude and frequency as the rf leakage. Before the AFP sweep was made, while H_1 is turned on but H_0 was still off resonance, the only signal detected by the lock-in amplifier was rf leakage. The cancellation signal was provided by a second HP frequency generator (cancellation HP) which was synchronized to the drive HP (see Fig. 3.4). The phase and amplitude of this cancellation signal could be adjusted manually as necessary so that together with the rf leakage signal the lock-in amplifier could be "zeroed" before the AFP sweep began.

Typically, when using an H_1 of 170 mG, a cancellation signal on the order of 2 mV was required.

The lock-in amplifier was frequency and phase-locked to the drive HP, enabling the lock-in amplifier to simultaneously detect both the amplitude and phase of the AFP signal. The AFP signal and the rf leakage signal were nearly $\pi/2$ out of phase from one another. In practice, we did not have a rotating rf field but the drive coil generated a linearly polarized magnetic field $2H_1 \cos\omega t\ \mathbf{j}$ that could be decomposed into two counter-rotating vectors of magnitude H_1. Only one of these rotating fields had the correct frequency *and* sense of precession to meet the resonance condition (and as a consequence affect the spins), while the other rotating component had little interaction with the spins. The pick-up coil therefore saw a linear rf field of $2H_1 \cos\omega t\ \mathbf{j}$ and a magnetization from the nuclear spins of $M(\cos\omega t\ \mathbf{j} + \sin\omega t\ \mathbf{i})$. The maximum rf leakage would then occur when there is maximum change of magnetic flux due to H_1 (automatically in the $\mathbf{j}$ direction), whereas the maximum AFP signal would occur when there was a maximum change in flux due to the nuclear spins in the direction of the pick-up coils (the $\mathbf{i}$ direction). These two occurrences were $\pi/2$ out of phase from one another and therefore the channel of the lock-in amplifier that contained the signal had much less noise than the out of phase channel. Detailed discussion of this phenomena can be found in Ref. [72].

3.6.5 Proton-Xe Coupling Experiment

The basic idea of the proton-Xe coupling experiment was to cause the protons to precess around their effective field in the rotating frame at the same frequency that ^{129}Xe precesses around the field in the laboratory frame. If the coupling between the two nuclear spin species was responsible for the increased ^{129}Xe relaxation rate observed in some samples at very low fields (≤ 20 G), then an increased relaxation rate should also be observed under this resonance condition. Such cross-coupling between the rotating and laboratory frames was first discussed in Kaplan and Hahn [73] and in Hartmann and Hahn [74]. In particular, we applied a rotating rf of magnetic field strength H_1 at the ^{1}H Larmor frequency

$$\omega = -\gamma_I H_0, \tag{3.12}$$

where γ_I is the gyromagnetic ratio of ^{1}H. Therefore H_1 was the proton's effective field in the frame rotating with the rf. Because we were far from the ^{129}Xe resonance, the effective field of the ^{129}Xe in the laboratory frame was essentially H_0. Therefore the

resonance condition for increased coupling occurred when

$$|\gamma_I H_1| = |\gamma_K H_0|, \tag{3.13}$$

where the γ_K is the the gyromagnetic ratio of ^{129}Xe. A tuned circuit (shown in Fig. 3.4) was already in use to take ^{129}Xe AFP measurements at 141 G. In order to make use of this circuit resonating at 166 kHz, we chose to operate at $H_0 = (|\gamma_K|/|\gamma_I|)141$ G = 39 G. From the field dependence data of the ^{129}Xe relaxation rate, a magnetic field of 39 G, without any rf applied, was strong enough to decouple the spins responsible for the observed increased relaxation at lower fields (see Fig. 4.5). The choice of 39 G for the dc static field in turn meant that we needed an H_1 of about 11 G (from Eq. (3.13)) in order to turn back on the coupling seen at lower fields.

The beauty of this proton resonance experiment was that the same circuit could be used for 1) the measurement of a ^{129}Xe AFP signal at a dc field of 141 G and 2) application of an 11 G H_1 at the proton resonance frequency in a dc field of 39 G. Moreover, unlike measurements in the rotating frame, this experiment also required no special field stabilization. The general measurement scheme then was as follows: using an H_1 of 170 mG, an AFP signal is taken at 141 G and the magnetic field is then dropped to 39 G. An H_1 of 11 G is then applied continuously through the drive coil. Changing H_1 only required increasing the output of the drive HP. After an appropriate amount of time (typically 10 min), this large rf field is turned off and the static dc field is returned to 141 G to take another ^{129}Xe AFP signal. The AFP signals from many such measurements were fitted to the exponential form in Eq. (3.5), after correcting for the time spent at the higher magnetic field. An increased ^{129}Xe relaxation rate, and therefore an increased coupling between Xe and protons, was observed for both the liquid and gas cells (see Chapter 4).

The only difficulty this experiment presented was the large H_1 needed to satisfy Eq. (3.13). Unlike the H_1 of 170 mG used for the ^{129}Xe AFP measurements, the 11 G H_1 required a power amplifier. An ENI amplifier model 350L was available, as already seen in Fig. 3.4. Although the 50 db amplifier's specified range was between 250 kHz – 100 MHz, it still produced an amplification of over 40 dB at 166 kHz, our operating frequency. The amplifier supplied nearly 40 V to the AFP probe to create a rotating field of 11 G. Assuming a resonant circuit impedance of 50 Ω, the calculated voltage across the tank circuit at resonance was well over 1000 V. The typical breakdown voltage of the mica capacitors we used was 500 V. For both C_1 and C_2, we therefore used many capacitors in series in order not to exceed this breakdown voltage.

3.7 Pulsed NMR

3.7.1 Overview

For a pulsed nuclear magnetic resonance (NMR) experiment, the liquid is placed in a dc field H_0 and pulsed for a brief period of time τ_p with a rotating rf field of strength H_1 and angular frequency $\omega_0 = -\gamma H_0$. The rf field $\mathbf{H}_1$ rotates in the plane perpendicular to $\mathbf{H}_0$. According to Eq. (3.1), the effective field suddenly experienced by the spins during τ_p is H_1. The magnetization $\mathbf{M}$ of the spins begins to precess around $\mathbf{H}_1$. The nuclear spins are tipped away from the direction of $\mathbf{H}_0$ by an angle,

$$\theta = \gamma H_1 \tau_p. \tag{3.14}$$

After the rf pulse, the effective magnetic field is again $\mathbf{H}_0$ and the spins precess around it. However, because they are now tipped by an angle θ from $\mathbf{H}_0$ they produce a rotating field of strength $M \sin\theta$ in the transverse plane to H_0. This rotating field is then detected by the same coil that transmitted the rf pulse. The main difference between pulsed NMR and AFP is that in pulsed NMR, the detection of the precessing spins occurs *after* the rf has been applied, not *during*. This intrinsically cuts down on noise problems. Also in pulsed NMR, unlike in AFP, a fraction or all of the magnetization is destroyed with each pulse. This is especially of concern because the polarization of laser-polarized nuclei is non-renewable. In pulsed NMR, the magnetization projected into the transverse plane $M \sin\theta$ is lost due to dephasing of the nuclear spins in an inhomogeneous magnetic field. The magnetization left is $M \cos\theta$. Therefore polarization loss can be minimized by using small pulse angles. For a more detailed description of pulsed NMR see Ref. [54, 57, 75].

3.7.2 Pulsed NMR Probe

The pulsed NMR measurements were made in a 14 kG iron-core electromagnet which corresponds approximately to a Larmor frequency (divided by 2π) of 16.462 MHz for ^{129}Xe, 59.462 MHz for ^{1}H, and 14.962 MHz for ^{13}C. We used a pulsed NMR spectrometer built by Brian Saam, a former Princeton graduate student [68]. All the rf electronics of this home-built spectrometer have a characteristic impedance of 50 Ω. The NMR probe, shown in Fig. 3.6, is similar in design to the previously described AFP probe and it has the same input impedance as given by Eq. (3.7). Therefore

the maximum H_1 of angular frequency ω_0 occurs when

$$\frac{1}{\sqrt{L(C_1 + C_2)}} = \omega_0 \text{ and } \mathrm{Re}(Z_0) = 50\ \Omega. \tag{3.15}$$

The variable capacitors, C_1 and C_2, are adjusted manually to meet these conditions.

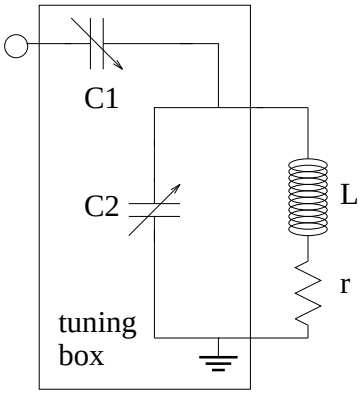

	^{1}H tuning box	^{129}Xe tuning box	^{13}C tuning box
C_1	2.5-10 pF	2.7-26 pF	4.6-75 pF
C_2	6-25 pF	2.7-26 pF	4.6-75 pF
L of coil	$\sim 1.0\ \mu$H	$\sim .7\mu$H	$\sim .7\ \mu$H

Figure 3.6: Pulsed NMR probe. The variable capacitors, C_1 and C_2, are adjusted so that the circuit is tuned to the correct frequency and the circuit impedance on resonance is matched to 50 Ω.

During the cross-relaxation studies, it became necessary to be able to switch quickly between measurements of different nuclear species without changing the magnetic field. Therefore we built three different tuning boxes. For ^{13}C and ^{129}Xe we were able to run a BNC cable from the coil centered between the pole pieces of the magnet to the tuning box placed conveniently outside the magnet. This BNC cable could then be easily switched between the two tuning boxes, enabling the use of the same coil for the detection of both nuclear species. However for ^{1}H, the tuning circuit needed to resonate at a much higher frequency and the extra capacitance of this BNC cable could not be tolerated. The tuning box for ^{1}H was soldered directly to the coil and it was therefore located in the narrow gap between the pole pieces of the electromagnet. As a consequence, we needed to build two separate coils and interleave them

around the dewar: one coil closely soldered to the tuning box of the protons and the other coil which could be used, through a BNC cable, for either ^{13}C or ^{129}Xe.

3.7.3 Relaxation Rate Measurements

The area under the Fourier transform of the free induction decay of the pulsed NMR signal is a reliable measure of polarization. If all the spins are equivalent for a given nuclear species the intial peak-to-peak value of the NMR signal is also a reliable measure of the polarization. For example, in cyclopentane (C_5H_{10}) all the proton spins are equivalent by symmetry, but in toluene ($C_6H_5CH_3$) the proton spins are nonequivalent. The polarization measurements, taken at appropriate time intervals, can be fit to an exponential (Eq. (3.5)) to determine the relaxation rate of the polarization. During a cross-relaxation study, the polarization relaxation rate of both the solute nuclear species and of ^{129}Xe turned out to be equivalent to the ^{129}Xe autorelaxation rate (see Chapter 5).

To conserve the non-equilibrium ^{129}Xe polarization, as well as to prevent saturation of the spectrometer, we used pulses between 0.2° and 4° for ^{129}Xe. Where significant, we corrected for the polarization loss per NMR pulse. In the cross-relaxation studies, for ^{1}H and ^{13}C we typically used 9° pulses. As we show in Chapter 5, however, we could use 90° pulses for ^{1}H and ^{13}C because the laser-polarized Xe can repeatedly enhance the solute polarization without significant depolarization of the ^{129}Xe.

The proton autorelaxation rate was measured when the ^{129}Xe polarization, and therefore the proton polarization as well, had reached its thermal equilibrium value. The method used to measure the proton's autorelaxation is known as saturation recovery [75]. A long train of 90° pulses with a separation of τ_s gives (after a steady state condition has been reached):

$$M(\tau_s) = M_0(1 - \exp^{-\tau_s/T_p}) \tag{3.16}$$

Measuring $M(\tau_s)$ for various values of τ_s, and fitting this data to Eq. (3.16), we extracted $1/T_p$, the proton autorelaxation rate. This measurement method relies on the renewability of thermal equilibrium polarization.

Chapter 4

Relaxation Mechanisms of ^{129}Xe in Liquid Xe

Streever and Carr [69] and Hunt and Carr (HC) [44] first studied ^{129}Xe relaxation in liquid Xe using thermally polarized ^{129}Xe. The use of laser-polarized ^{129}Xe provides a boost of five orders of magnitude in polarization over thermally polarized ^{129}Xe at 14 kG and 200 K. Therefore we have a new sensitive probe of the liquid. Fig. 4.1 shows the improvement of signal to noise ratio in our data over that taken with the thermally polarized ^{129}Xe. A portion of the material in this chapter was published in a different form in Ref. [76].

We explore the relaxation mechanisms in liquid Xe by studying the relaxation rate of the laser-polarized ^{129}Xe as a function of magnetic field, temperature, and cell environment. The first section of this chapter discusses our measurements at 14 kG and between 165 and 240 K. We compare our results to the earlier high-field (5 – 25 kG) work of HC and to the theoretical results of Oppenheim, Bloom, and Torrey (OBT) [50] in which the spin-rotation interaction is proposed to be the dominant relaxation mechanism. In the second section of this chapter we discuss our results at 135 G, the first measurements of the ^{129}Xe relaxation rate in liquid Xe made at such a low magnetic field. We compare this low-field data to the 14 kG data.

Finally, in the last section we explore the liquid ^{129}Xe relaxation rate at even lower fields than 135 G. Because of the significant field dependence seen below 135 G, we developed an elegant technique to discover whether the coupling between ^{129}Xe and protons was responsible for the observed field dependence. We used this method, which involves cross-coupling between the protons in their rotating frame and ^{129}Xe

in the laboratory frame, to study the coupling between surface protons and ^{129}Xe in the liquid and gas phases.

4.1 High Field Liquid ^{129}Xe Relaxation Rate

4.1.1 The Signature of Surface Relaxation

HC, after coating their cells with Drifilm and observing no change in relaxation rate from their uncoated cells, ruled out surfaces as a significant relaxation mechanism. However, because our measured relaxation rates were smaller than theirs we suspected that surfaces (or some other impurity) might have been contributing to their relaxation. In order to test the worst case scenario, we coated a 2.4 mm diameter pyrex cell with Gd^{3+} ions as described in Chapter 3, which provided an effective magnetic moment of 8.0 Bohr magnetons for the ^{129}Xe to couple to.

Before putting liquid Xe in this cell, we examined the surface of the Gd^{3+} cell and an uncoated pyrex cell of similar geometry by filling both cells with 5 atmospheres of laser-polarized Xe gas at 200 K. The ^{129}Xe gas in the uncoated cell had a T_1 of 25 min ($1/T_1 \sim 6.7 \times 10^{-4}$ s^{-1}) and the Gd^{3+} cell had a T_1 of 4 min ($1/T_1 \sim 42 \times 10^{-4}$ s^{-1}). The contribution of field inhomogeneities to these gas relaxation rates is given by [47, 48]

$$\frac{1}{T_1^{\rm inh}} = D\frac{|\nabla H_{0\rm x}|^2 + |\nabla H_{0\rm y}|^2}{H_0^2}, \tag{4.1}$$

where H_0 is the dc applied field in the $\hat{z}$ direction, and $\nabla H_{0\rm x}$ and $\nabla H_{0\rm y}$ are the gradients of the transverse components of the field. The field gradients would have provided a contribution on the order of $\sim 2 \times 10^{-4}$ s^{-1} to the gas relaxation rate because its diffusion constant is large (5.2×10^{-3} cm^2/s [77]) and most of the gas was located near the top of the cell where the gradients were highest (~ 2 kG/cm). Therefore, the ^{129}Xe relaxation rate due to *surface* effects in the Gd^{3+} cell was *more* than 6 times that in the uncoated cell.

We also observed an increased ^{129}Xe relaxation rate in the liquid phase for the Gd^{3+} cell over the uncoated cell. The contribution of field inhomogeneities to the ^{129}Xe relaxation rate in the liquid phase is negligible because of the liquid's small diffusion constant. However, the ^{129}Xe relaxation rate of liquid Xe in the Gd^{3+} cell was only 1.3 times that of the uncoated cell (see Fig. 4.1), a much smaller increase than that observed for the gas phase. This implies that the total ^{129}Xe relaxation

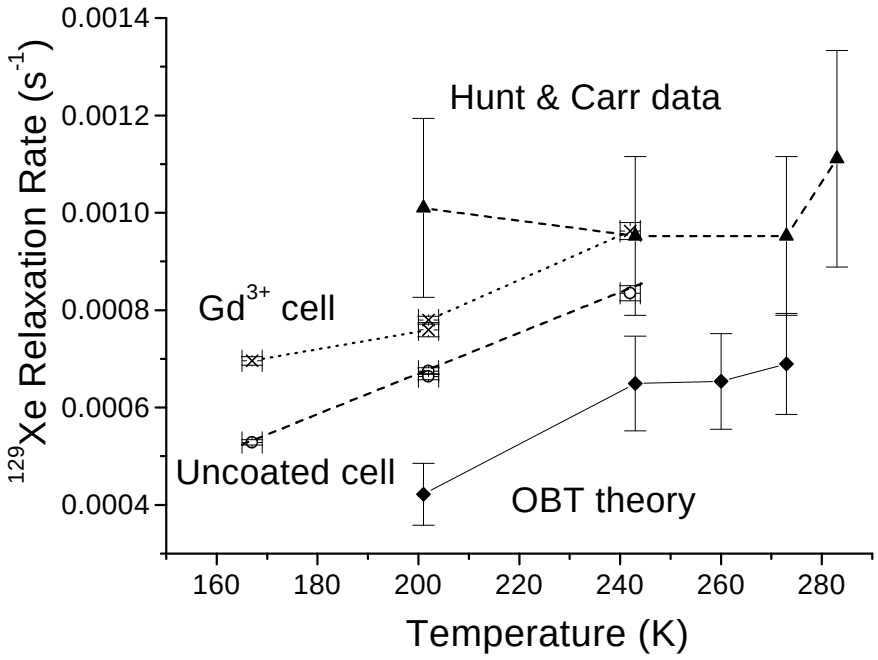

Figure 4.1: ^{129}Xe relaxation rates vs. temperature at high magnetic field. Hunt and Carr [44] measured the ^{129}Xe relaxation rates using thermal equilibrium Xe at 5, 12, and 25 kG. We took data using laser-polarized ^{129}Xe at 14 kG, using pyrex cells; a representative uncoated cell and one coated with Gd^{3+} are shown above. The theory curve was calculated by Oppenheim, Bloom, and Torrey [50] using the spin-rotation interaction as the relaxation mechanism.

rate in the liquid phase was dominated by the bulk liquid, not its interactions with the surfaces. In fact, the difference between the ^{129}Xe relaxation rate in the liquid in the Gd^{3+} cell and the uncoated cell was smaller than HC's error bars. Therefore perhaps the difference between our data and HC's data could be attributed to surface effects.

We went further with our examination of surface contributions to study uncoated pyrex cells of different diameter tubing from 1 to 4 mm (see Fig. 4.2a). If the contribution of surface effects to the ^{129}Xe relaxation rate was significant, it should be observable in the relaxation rate as a function of diameter. From modeling ^{129}Xe surface relaxation as evaporation from the surface of a cylinder of radius b, the ^{129}Xe

relaxation rate should decrease as b increases. At the surface

$$-D\frac{\partial C}{\partial r} = \alpha C, \tag{4.2}$$

where D is the diffusion constant and C is the polarization density. The proportionality constant α is a measure of how depolarizing the surface is to ^{129}Xe. Assuming an initial uniform polarization P_0, the amount of polarization after a time t would be given by [78]

$$P(t) = P_0 \sum_{n=1}^{\infty} \frac{4L^2 e^{-\beta_n^2 Dt/b^2}}{\beta_n^2(\beta_n^2 + L^2)}, \tag{4.3}$$

where the β_n's are the roots of

$$\beta J_1(\beta) - LJ_0(\beta) = 0 \tag{4.4}$$

and

$$L = \frac{b\alpha}{D}, \tag{4.5}$$

a dimensionless parameter. After the initial transients, in which the liquid sample equilibrated to the dewar's temperature, we observed a single exponential for our ^{129}Xe relaxation rate. That would imply that, if surface interactions were responsible for the relaxation, the ^{129}Xe relaxation rate would given by the first term of Eq. (4.3), with $1/T_1^{\rm surf} = \beta_1^2 D/b^2$. In the surface-limited case, where the spins are able to diffuse rapidly to the surface (L is small), the relaxation rate reduces to $4\alpha/b$. In the opposite extreme when diffusion to the wall is the limiting factor in the relaxation rate (L is very large), the diffusion-limited case, β_1 approaches a constant and the relaxation rate is proportional to D/b^2. In either case, one expects to see, assuming α is the same for all uncoated pyrex cells, that the ^{129}Xe relaxation rate decreases with increasing diameter.

The ^{129}Xe relaxation rate in the pyrex cells of different diameters showed no such inverse dependence on the radius of the pyrex tubing of cell, even though the radius changed by a factor of four in the cells we examined. As seen in Fig. 4.2(a), there is very little variation between different diameter cells at 14 kG. This slight variation of different diameter cells is another indication that the total ^{129}Xe relaxation rate in liquid Xe is dominated by interactions in the bulk liquid at 14 kG.

4.1.2 The Signature of Spin-Rotation

In response to the work done by Streever and Carr [69] and Hunt and Carr (HC) [44], Torrey [43] and Oppenheim, Bloom, and Torrey (OBT) [50] proposed that the spin-rotation mechanism was the main mechanism of ^{129}Xe relaxation in the bulk liquid. When two Xe atoms collide, their charge clouds become distorted. The rotation of these distorted charge distributions produces the time varying magnetic field H_r necessary for relaxation.

According to Torrey's model [43], the interaction potential is given by the Hamiltonian

$$\mathcal{H}' = -\gamma_K \hbar \mathbf{K} \cdot \mathbf{H_r}, \tag{4.6}$$

where a nuclear spin $\mathbf{K}$ having a gyromagnetic ratio γ_K feels the magnetic field $\mathbf{H_r}$. In general, H_r will be proportional to ω, the angular velocity of the diatomic system, by a proportionality factor $f(R)$ depending on the distance R between the two atoms [43]

$$H_r = \omega f(R). \tag{4.7}$$

Using this and

$$\omega = \frac{\mathbf{R} \times \mathbf{P}}{\mu R^2}, \tag{4.8}$$

where $\mathbf{P}$ is the relative momentum between the two particles and μ is the reduced mass, $\mathcal{H}'$ can be written as

$$\mathcal{H}' = -\left(\frac{\gamma_K \hbar}{\mu R^2}\right) f(R) \mathbf{K} \cdot \mathbf{R} \times \mathbf{P}. \tag{4.9}$$

Torrey used a model, proposed by Adrian Ref. [79], where van der Waals forces cause the distortion of the charge clouds and f(R) is given by

$$f(R) = \frac{\kappa}{R^6}. \tag{4.10}$$

κ is taken as 2.7×10^{-56} c.g.s. units by OBT. (Adrian, in a paper after OBT's paper, calculated that, in addition to the van der Waals forces, the exchanges forces make a sizable contribution to $f(R)$ [80].)

In addition to the interaction Hamiltonian, the collisional trajectories of the atoms also need to be determined to calculate the relaxation rates. In a liquid, the two particles of interest interact with many other particles while interacting with each other. The collisional trajectories are therefore determined by not only the potential of the pair of atoms, but also by a frictional restoring force and a rapidly fluctuating

force caused by all the surrounding atoms (see the discussion of the Langevin equation in Ref. [81]). The interaction potential is assumed to be small compared to the pair potential and is therefore not included in determining the collisional trajectories. OBT approximate the Xe-Xe interaction using a hard sphere pair potential for ease of calculation. In addition, OBT use what is known as the "constant acceleration approximation", whereby the the force on a particle due to the pair potential is taken as constant.

With the spin-rotation interaction and the assumptions used to predict the collisional trajectories, OBT find that the relaxation rate in s^{-1} is given by

$$\frac{1}{T_1} \cong 0.01 D \rho_a g(1.08), \tag{4.11}$$

where D is the diffusion constant, ρ_a is the density in amagats, and $g(1.08)$ is the the radial distribution function at a radius of 1.08 a (a is the distance R at which the Lennard-Jones 6-12 potential goes to zero). The radial distribution function is dependent on temperature, density, and the pair potential model. OBT found, using a hard sphere model, that $g(1.08)$ increases with decreasing temperature. Ehrlich and Carr [51] observed that

$$\rho D \propto T^{2.74}. \tag{4.12}$$

This temperature dependence dominates over the temperature dependence of $g(1.08)$. Therefore the ^{129}Xe relaxation rate due to spin rotation is predicted to decrease with decreasing temperature. Our results show such a dependence, in contrast to the results of HC. As to the difference in values between our experimental results and the proposed theory, OBT end their paper with [50]

> The agreement between experiment [HC's data] and theory is remarkable considering the rough evaluation of [the formulas]... and the approximations introduced into the theory.

Moreover, Adrian's later calculation [80] that the dominate contribution to $f(R)$ is from the exchange forces, *not* van der Waals forces, means that OBT's model underestimates the ^{129}Xe relaxation rate.

4.2 ^{129}Xe Relaxation Rate at 135 G

According to OBT's model, there should be no field dependence of the ^{129}Xe relaxation rate due to spin-rotation. However, Xe_2 does form weakly bound molecules (the

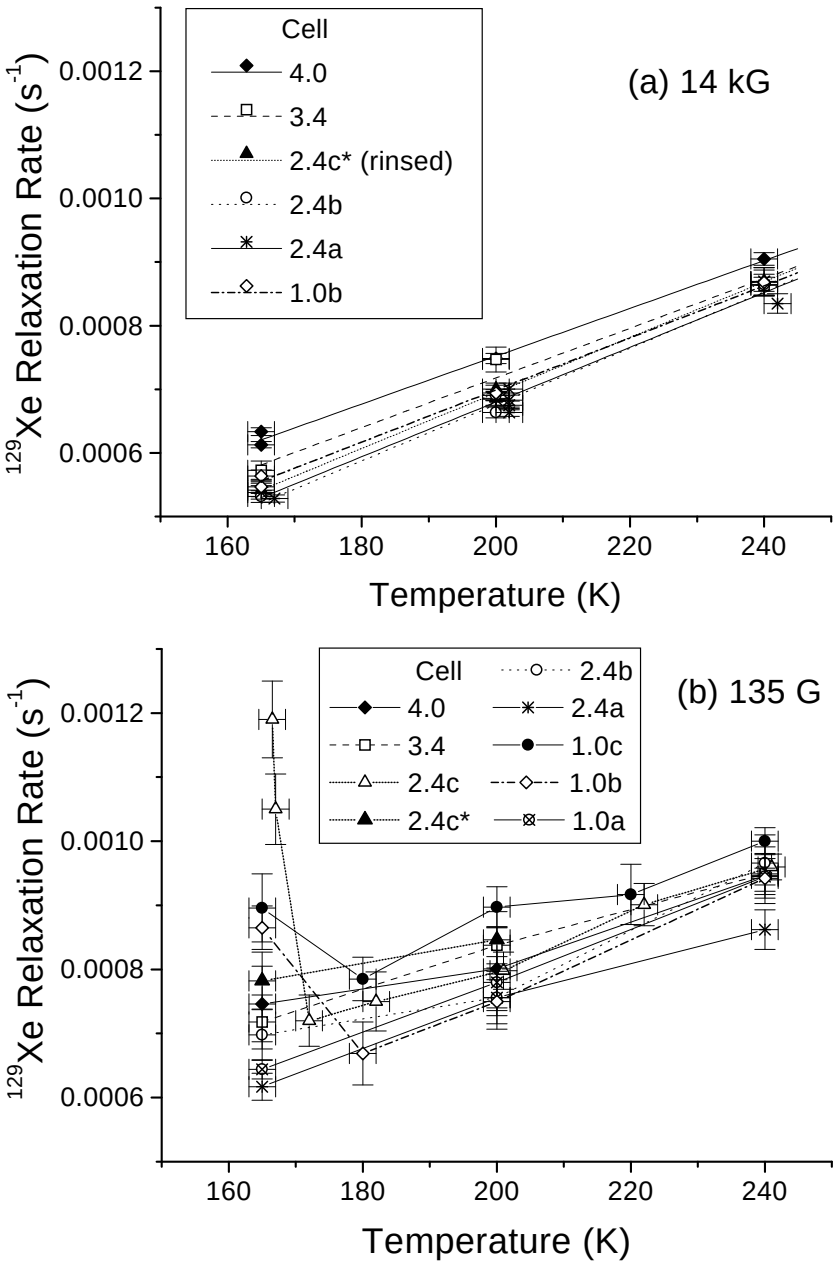

Figure 4.2: Comparison of ^{129}Xe relaxation rates at (a) 14 kG and (b) 135 G. The ^{129}Xe relaxation rate was measured as a function of temperature and cell diameters, given by the cell number in mm (cell 4.0 had a 4 mm diameter, cell 3.4 a 3.4 mm diameter, etc.). 2.4c* is cell 2.4c after the cell has been rinsed with acetone and methanol. All lines are only intended to guide the eye.

ground states of the Xe atoms are repulsive except for van der Waals attractions which provide a minimum of 0.024 eV at about 4.4 Å internuclear separation) [82]. If the ^{129}Xe relaxation caused by ^{129}Xe in Xe molecules is significant, field dependence of the ^{129}Xe relaxation rate in the bulk liquid might be present. Measurements of ^{129}Xe relaxation rates made by HC at 5.0, 12.2, and 25 kG revealed no field dependence. Our measurements of ^{129}Xe relaxation rates taken at 14 kG and 135 G are shown in Fig. 4.2. The cell which consistently exhibited the smallest ^{129}Xe relaxation rates, cell 2.4a, showed no difference in ^{129}Xe relaxation rates between the two fields at 240 K and a somewhat larger relaxation rate at 135 G than 14 kG at colder temperatures. Cell 2.4a's overall insensitivity to magnetic field on the scale observed is consistent with the ^{129}Xe relaxation rate being dominated by bulk liquid at 1.4 kG and with spin-rotation being the relaxation mechanism in the bulk liquid.

Unlike the ^{129}Xe relaxation rates at 14 kG, which show little variation between cells, the ^{129}Xe relaxation rates in our cells at 135 G showed significant variation between cells, especially at lower temperatures. A surface relaxation mechanism can cause increased relaxation with decreasing temperature because both the correlation time and the fraction of ^{129}Xe dissolved inside the wall coating are exponential in (1/kT) [30]. The variation of ^{129}Xe relaxation rates in different cells was not correlated with cell diameter, indicating that there was a greater difference in α, the parameter that characterizes how depolarizing the surface is to ^{129}Xe, than in the cell diameter.

Cell 2.4c deviated the most from the ^{129}Xe relaxation rates observed at 14 kG. Figure 4.3 shows the ^{129}Xe relaxation rate of liquid Xe in cell 2.4c at 135 G. The cell originally showed a very sharp increase of relaxation rate with decreasing temperature starting at $\sim$ 170 K. It was only possible to characterize this curve qualitatively, not quantitatively, because of the narrow range of temperature available between 170 K and the triple point (161.4 K) and our control of the temperature to within 2 K. The line drawn in Fig. 4.3 is only intended to guide the eye. After cell 2.4c had been rinsed with both acetone and methanol, the sharp increase in ^{129}Xe relaxation rate below 170 K disappeared (see Fig. 4.3). Apparently, by rinsing the cell, we removed the surface impurities that had provided the dominant ^{129}Xe relaxation mechanism below 170 K.

Figure 4.2 also shows that the the error bars of the relaxation rates measured at 135 G are on the order of four times larger than at 14 kG. The dominant contribution to the errors were due to random changes that occurred between one filling of a cell to the next (see Fig. 4.4). We calculated the standard deviation σ of numerous relaxation rates measured using the same cell. This standard deviation was representative of

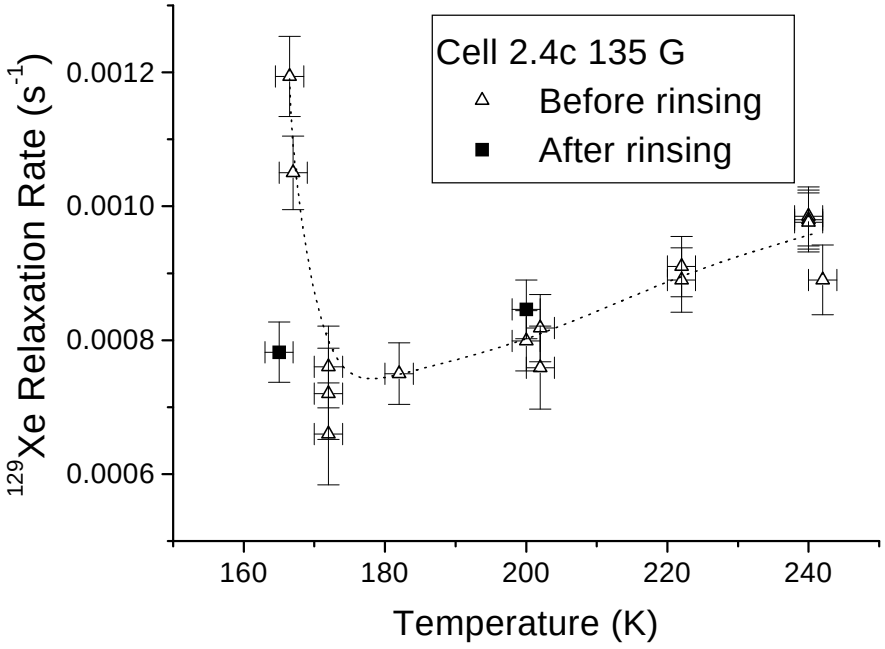

Figure 4.3: Effects of surface changes on the ^{129}Xe relaxation rate. Cell 2.4c, before rinsing, and after rinsing with acetone and methanol. The dashed line is only intended to guide the eye.

the errors introduced by these random changes in relaxation rate. As can be seen in Fig. 4.4, the error bars due to experimental errors (i.e. the errors from fitting our data to an exponential which was dominated by experimental error) were much smaller than the standard deviation and could not account for the standard deviation. For the data in Fig. 4.2(b) and 4.3, we added the standard deviation in quadrature to the experimental errors to obtain the total uncertainty for a given relaxation rate measurement.

What caused these random variations in ^{129}Xe relaxation rates from measurement to measurement at 135 G? The variation of the relaxation rate seemed to have no dependence on liquid height (as it might if the gas had been contributing to the ^{129}Xe relaxation rate in the measured liquid). The error in the temperature was not large enough to account for this variation because, for the most part, the relaxation rate had only a mild dependence on temperature. We initially thought that perhaps

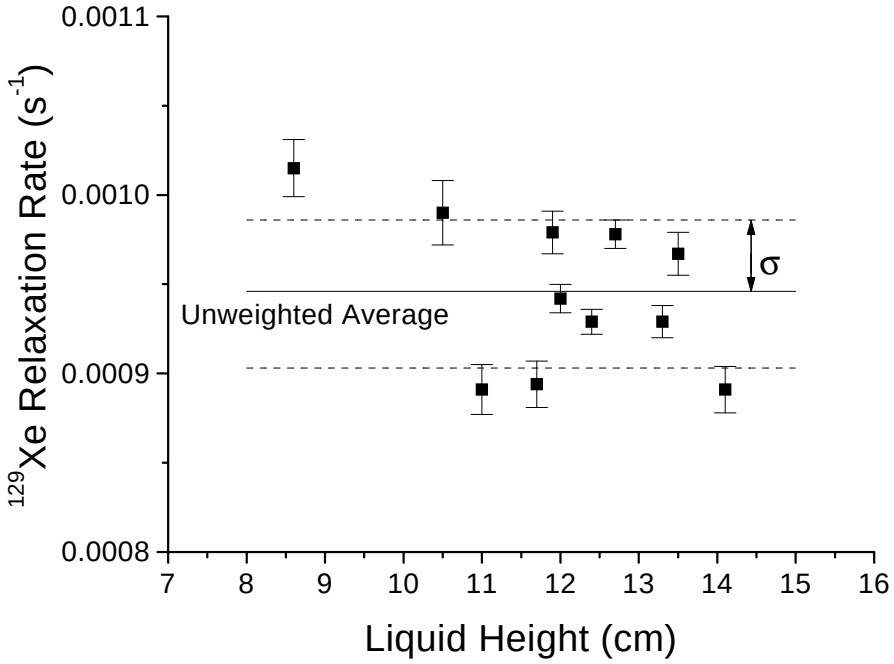

Figure 4.4: Random uncertainties in the low field ^{129}Xe relaxation rates. Cell 1.0a was measured several times at 135 G and 240 K. The straight line is the unweighted average of the measurements and the dashed lines shows the standard deviation.

the variation was caused by small variable amounts of oxygen in our samples being leaked in from the transfer plumbing connecting the cold trap to the measurement cell. We tried many methods of improving the transfer technique. However, none of these improvements seemed to have any effect whatsoever in the relaxation rates observed. This led us to believe that there was no such leak. The largest suspect of these random changes became slight changes in the surface from run to run. This hypothesis was supported by the field dependence of the standard deviation σ. At 135 G, $\sigma \approx 0.4 - -0.5 \times 10^{-4}$; at 14 kG, $\sigma \approx 0.13 \times 10^{-4}$, on the order of the experimental errors at 14 kG. Although the measurements at 14 kG were taken using pulsed NMR and those at 135 G with AFP, the temperature control system and filling procedure were essentially the same for both fields. Coupled with the results shown in Fig. 4.2, surface variations are the likely candidate for the observed variations in low-field relaxation rates.

4.3 ^{129}Xe-Proton Coupling Experiment

4.3.1 Field Dependence Observed Below 140 G

We continued to study the ^{129}Xe relaxation rate in the liquid as a function of magnetic field by taking measurements at fields under 140 G. The field dependence we observed was similar to the field dependence observed by Driehuys [31, 30] for ^{129}Xe in the gas phase in sealed pyrex cells coated with SurfaSil [83]. Figure 4.5 shows results from gaseous Xe in a SurfaSil cell at 250 K and from liquid Xe in cell 1.0c at 240 K (other cells studied displayed a similar, but smaller, field dependence of the ^{129}Xe relaxation rate in liquid Xe). The observed field dependence of ^{129}Xe relaxation rate is caused by fluctuating fields at the ^{129}Xe nucleus. The power spectrum of a fluctuating field contains all frequencies up to $\sim \tau_c^{-1}$, the inverse correlation time. The ^{129}Xe nucleus relaxes when the ^{129}Xe Larmor frequency, $\omega_{0K} = -\gamma_K H_0$, is smaller in magnitude than $\sim \tau_c^{-1}$.

The fluctuating fields responsible for the ^{129}Xe relaxation are most likely caused on the surface by 1) protons from either the OH groups on the glass surface, water, or other organic molecules stuck to the surface, 2) paramagnetic impurities, such as iron found in the pyrex, and 3) other Xe atoms trapped together on the surface so that the correlation time might be longer than in the liquid. In the original work done by Driehuys, the ^{129}Xe relaxation rate in the SurfaSil cell was found to be dominated by dipole-dipole coupling to surface protons using a double resonance experiment. Using a model of dipole-dipole coupling to protons, the ^{129}Xe relaxation rate can be calculated

$$\frac{1}{T_1} = \frac{1}{10T_0}\left(\frac{1}{1+(\omega_{0K}-\omega_{0I})^2\tau_c^2} + \frac{3}{1+\omega_{0K}^2\tau_c^2} + \frac{6}{1+(\omega_{0K}+\omega_{0I})^2\tau_c^2}\right), \qquad (4.13)$$

where ω_{0I} and ω_{0K} are the proton and ^{129}Xe Larmor frequencies respectively. The zero-field relaxation $1/T_0$ is given by

$$\frac{1}{T_0} = \frac{4}{3} f I(I+1)\gamma_K^2\gamma_I^2\hbar^2\tau_c \sum_i r_i^{-6}, \qquad (4.14)$$

where f is the fraction of ^{129}Xe adsorbed on the surface, γ_K and γ_I are the ^{129}Xe and proton gyromagnetic ratios, and r_i is the distance from the adsorbed ^{129}Xe atom to the i^{th} neighboring proton. The ^{129}Xe relaxation rate of gaseous Xe in the SurfaSil cell was fit to two such expressions of Eq. (4.13) plus a constant background. The correlation time corresponding to the larger peak, τ_{c1}, was 9.3 μs and that corresponding to the

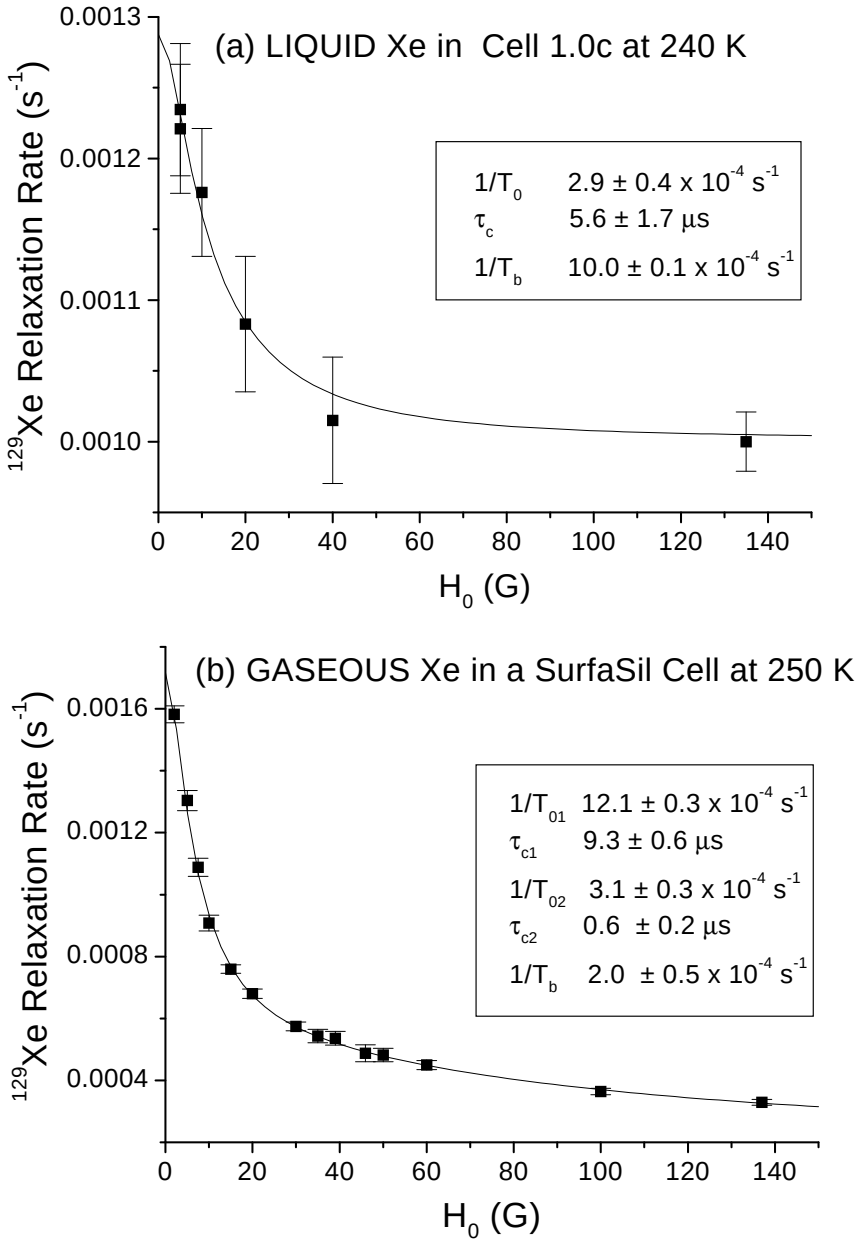

Figure 4.5: ^{129}Xe relaxation rate vs magnetic field for $H_0 < 140$ G. (a) Liquid Xe in cell 1.0c at 240 K. The fit of the data to a model of dipole-dipole coupling to surface protons (Eq. (4.13)), gives the values for the background relaxation rate $1/T_b$, the zero-field peak height $1/T_0$, and the correlation time τ_c. (b) Gaseous Xe in a SurfaSil cell at 250 K and the relaxation curve was fit to a sum of two expressions of the form in Eq. (4.13) plus a constant background.

smaller peak, τ_{c2}, was 0.6 μs (see Fig. 4.5). Fitting the liquid data of cell 1.0c to Eq. (4.13), plus a constant background, gives a τ_c of 6 μs, on the same order as τ_{c1} for the Xe gas data in the SurfaSil cell.

In the liquid, we observed that the correlation time increased with decreasing temperature as $\tau_c \propto \exp(E_a/kT)$ (see Fig. 4.6). The increasing τ_c at colder temperatures is reflected in the narrowing of the field dependence seen in Fig. 4.6(a). We also measured the relaxation rate at 165 K and saw no field dependence of the ^{129}Xe relaxation rate between 5 and 140 G presumably because the peak had become too narrow. Figure 4.6(b) shows the fit of τ_c to $\tau_{c0}\exp(E_a/kT)$ with an activation energy of $E_a = 0.11 \pm .04$ eV. This activation energy is similar to what Driehuys found to be the binding energy of the surface site for gaseous Xe in the SurfaSil coated cell, $E_s = 0.10 \pm 0.01$ eV. Most of the data of Fig. 4.6 were taken within a two week period because we noticed there was a slow evolution of surface properties.

According to Eq. (4.14), $1/T_0$ is directly proportional to both f, the fraction of Xe adsorbed to the coating, and to τ_c. The fraction of Xe adsorbed to the coating can be estimated by modeling the particles adsorbed on the surface as a two-dimensional gas. This 2-d gas must be in equilibrium with both the gas and the liquid phase and therefore the chemical potential of the liquid, vapor, and 2-d gas must all be equal. Setting the chemical potential of the vapor and the surface gas equal, the mean number n of particles adsorbed per unit area of the surface can be calculated to be [81]

$$n = \frac{p\ h\ e^{E_s/kT}(kT)^{-3/2}}{\sqrt{2\pi m}} \tag{4.15}$$

where p is the mean pressure of the surrounding vapor, m is the Xe mass, h is Planck's constant, and k is Boltzmann's constant. Using 0.11 eV as E_s, we calculated that n remains fairly constant at $\sim 1 \times 10^{18}/\mathrm{m}^2$ over the range 180 to 240 K. The fraction of Xe dissolved in the coating f is proportional to n/ρ where ρ is the Xe number density of liquid Xe. Because ρ only changes by 20% over the range 180 to 240 K, f is not significantly dependent on temperature. The main temperature dependence of $1/T_0$ therefore comes from τ_c. The zero-field peak height $1/T_0$ does in general get larger at decreasing temperatures, but this dependence does not fit well to $\exp(0.11\ \mathrm{eV}/kT)$ as would be expected from temperature dependence of τ_c. An accurate measurement of $1/T_0$, however, is very sensitive to relaxation measurements near 0 G, which are difficult to perform in the laboratory frame.

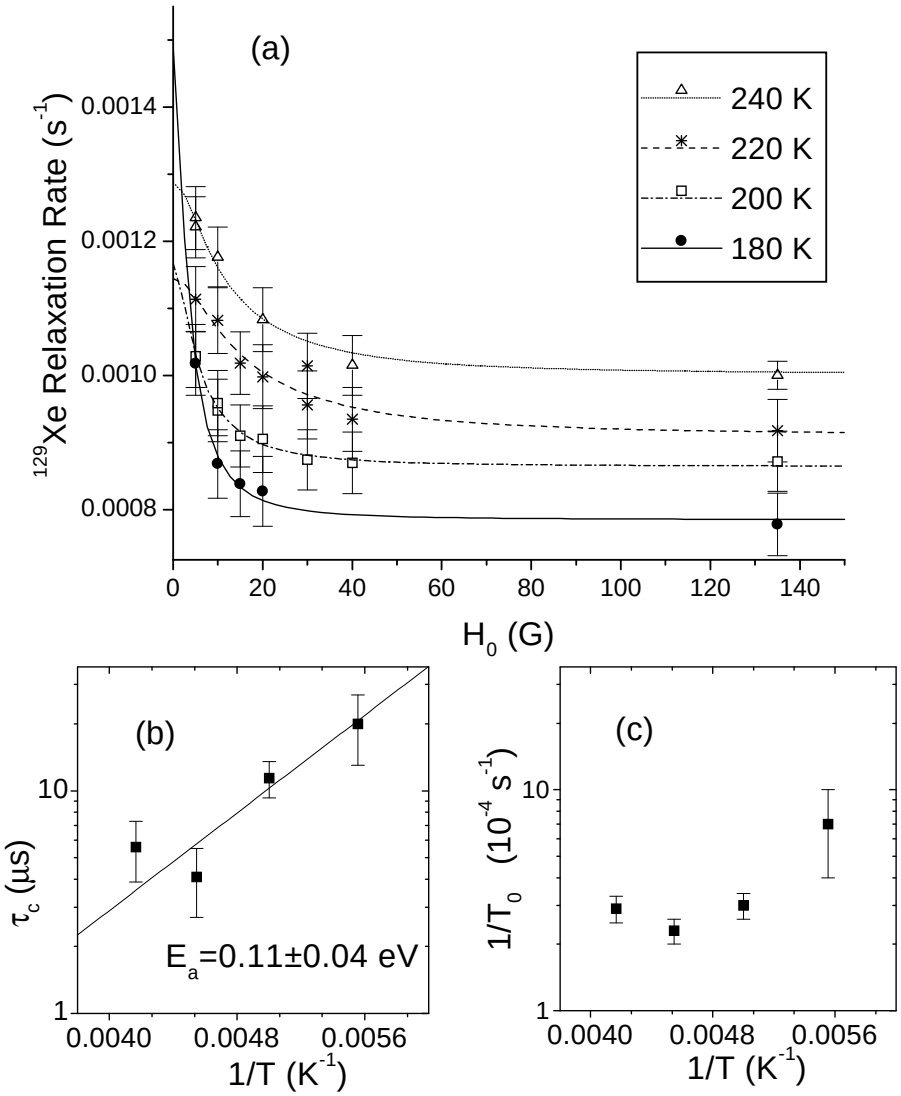

Figure 4.6: Temperature dependence of the field-dependent ^{129}Xe relaxation rate in the liquid. The narrowing of the peaks in (a) as the temperature decreases is an indication of increasing correlation times τ_c. The correlation times are fitted to $\tau_{c0}e^{E_a/kT}$ in (b). Graph (c) shows the increase in the zero-field peak height as function of decreasing temperature.

4.3.2 Cross-coupling of Rotating and Laboratory Frames

A double-resonance experiment like that used by Driehuys [31, 30] could have been used to see whether surface protons contributed to the low field ^{129}Xe relaxation in the liquid. In the Driehuys double resonance experiment, the ^{129}Xe is spin-locked to a small rotating field at the ^{129}Xe Larmor frequency while a second rotating field is applied at the proton Larmor frequency. The strength of this proton rf is increased until the proton Rabi frequency $\omega_{1I} \gg 1/\tau_c$, the intrinsic frequency of the proton dipole-dipole fluctuations. At such large resonant proton fields, the ^{129}Xe relaxation rate in the rotating frame is slowed down, demonstrating the low-field coupling between the ^{129}Xe and the surface protons. However, the double resonance experiment requires two rotating rf fields (one at the proton Larmor frequency and one at the ^{129}Xe Larmor frequency). Because our AFP measurements were already done with two coils this would have meant adding a third coil in a very limited space and a third frequency generator. Furthermore, in order to measure the ^{129}Xe relaxation rate in the rotating frame for the Driehuys double resonance experiment, a magnetometer is also needed to stabilize the field to within a small fraction of a Gauss. Because of the difficulty of this experiment, lack of equipment, and limited space, we developed a new, simpler way to explore whether the coupling between ^{129}Xe and the protons caused the increased relaxation rates at low fields.

As described in Chapter 3, we can cross-couple between the protons in their rotating frame and ^{129}Xe in the laboratory frame without any additional coils or equipment but a power amplifier (which we would have also needed for the Driehuys double resonance experiment). At a static field H_0 greater that the decoupling field $H = 1/(\gamma_K \tau_c)$, the coupling between ^{129}Xe and protons should be turned on again when the proton Rabi frequency is matched to the ^{129}Xe precession frequency around H_0 in the laboratory frame. Such cross-coupling between frames was first discussed by Kaplan and Hahn [73] and by Hartmann and Hahn [74]. We first tested this cross-coupling between frames in a system in which the Xe-proton coupling had already been confirmed as the main source of ^{129}Xe relaxation, i.e., with gaseous Xe in a SurfaSil cell. In order to compare our results to Driehuys' earlier results, we used the same SurfaSil-coated cell that Driehuys used for his double resonance experiment [31, 30]. The data shown in Fig. 4.6(b) are the low field ^{129}Xe relaxation rates we measured using this cell and compare favorably with the results shown by Driehuys [30].

There are other reasons why the Xe gas in a SurfaSil-coated cell makes a good first choice for trying to match the proton Rabi frequency to the ^{129}Xe Larmor frequency. SurfaSil has an abundant number of surface protons. In addition, the SurfaSil-coated

cell is a 1 cm^3 pyrex cell sealed with Rb inside for quick polarization of the 600 torr of Xe (enriched to 73% ^{129}Xe) through spin-exchange optical pumping. For the SurfaSil coated cell, with Xe gas at 250 K, the background relaxation rate $1/T_b$ is only 12% of the total zero-field height, whereas for cell 1.0c, with liquid Xe at temperatures between 180 and 240 K, $1/T_b$ is over 50% of the total zero-field height. Moreover, the total gaseous peak height in Fig. 4.5 (b), $1/T_{01} + 1/T_{02}$, is a factor of two times larger than the peak heights of all the liquid Xe relaxation curves shown in Fig. 4.6. For these reasons, the effects of the cross-coupling between the laboratory and the rotating frame should be more apparent in the gaseous Xe/SurfaSil system than in the liquid system.

4.3.3 Cross-coupling in Gaseous Xe

Figure 4.7(a) shows the increase of ^{129}Xe relaxation rate in the laboratory frame measured at 250 K with a rotating rf of field strength $H_1 \approx (\gamma_K/\gamma_I)39$ G = 10.8 G and an angular frequency equal to the proton Larmor frequency at 39 G. The peak of the increased relaxation occurs at 39 G, where the proton Rabi frequency, $\omega_{1I} = -\gamma_I H_1$, is matched to the ^{129}Xe Larmor frequency, $-\gamma_K H_0$. Figure 4.7(b) shows that the increase of relaxation is dependent on the strength of the rf. Again the largest relaxation should occur when $|\gamma_I H_1| = |\gamma_K H_0|$. According to the Fig. 4.7(b) the peak occurred at 11.9 G which is 10% higher than the expected value of H_1 = 10.8 G. However H_1 in Fig. 4.7(b) was only roughly calibrated using a twenty-turn Faraday coil which had an uncertainty of 10% in its area. The fit of the data in Fig. 4.7(b) gave a new more accurate calibration of H_1. With this new calibration we determined that for the measurements made in Fig. 4.7(a) the H_1 used was 10.3 G instead of the desired 10.8 G. However because the full width at half maximum of the peak in Fig. 4.7(b) is 4 – 5 G, this small discrepancy made little difference. Figures 4.7(a) and (b) together confirm what Driehuys had found through his double resonance experiment: dipole-dipole relaxation due to surface protons is the dominant source of relaxation in this system.

The H_1 dependence of the ^{129}Xe relaxation rate seen in Fig. 4.7(b) can be fit to (see Chapter 2)

$$\frac{1}{T_1} = \frac{1}{40T_0}\left[\frac{6}{1+(\omega_{1I}+\omega_{0K})^2\tau_c^2} + \frac{6}{1+(\omega_{1I}-\omega_{0K})^2\tau_c^2} + \frac{12}{1+(\omega_{0I}+\omega_{0K})^2\tau_c^2} + \frac{6}{1+(\omega_{0I}-\omega_{1I}+\omega_{0K})^2\tau_c^2} +\right.$$

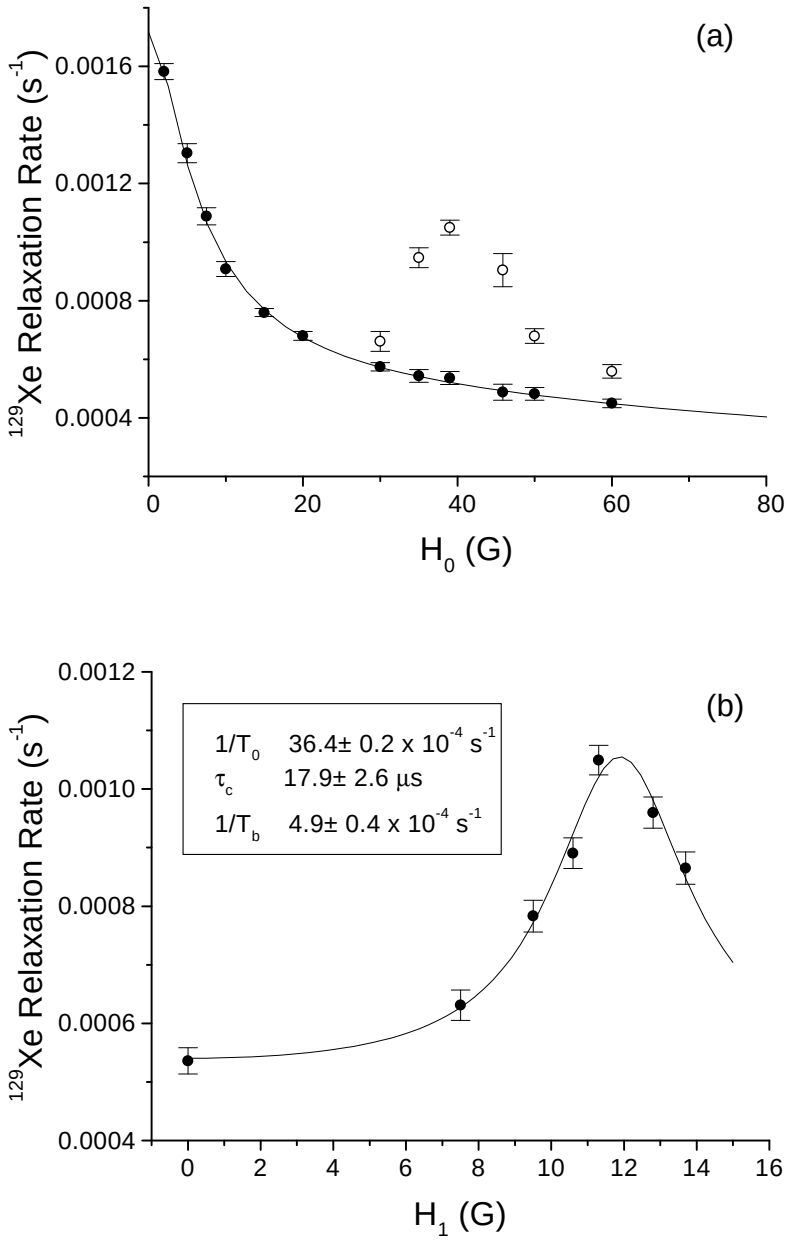

Figure 4.7: Cross-coupling between the laboratory frame and the rotating frame in a SurfaSil cell filled with Xe gas at 250 K. In graph (a), ○'s represent the ^{129}Xe relaxation rate with a rotating 10.3 G H_1 at 166.3 kHz and ●'s represent the ^{129}Xe relaxation rate without this rf. Graph (b) show the H_1 dependence of the ^{129}Xe relaxation at an H_0 of 39 G.

$$\frac{6}{1+(\omega_{0I}+\omega_{1I}+\omega_{0K})^2\tau_c^2}+\frac{1}{1+(\omega_{0I}+\omega_{1I}-\omega_{0K})^2\tau_c^2}+\frac{2}{1+(\omega_{0I}-\omega_{0K})^2\tau_c^2}+\frac{1}{1+(\omega_{0I}-\omega_{1I}-\omega_{0K})^2\tau_c^2}\Bigg], \tag{4.16}$$

where the first term gives the dominant dependence on the resonant field H_1 (because γ_I and γ_K are of opposite signs). The correlation time τ_c from this fit is 17.9 ± 2.6 μs, which is twice as long as the correlation time expected from the static field dependence, 9.3 ± 0.6 μs. Furthermore, the ^{129}Xe relaxation rate at $H_1 = (|\gamma_K|/|\gamma_I|)H_0$ is about three times the expected value (the expected value, according to Eq. (4.16) should be $(3/20)(1/T_0)$). Although these results do not agree with the expected results, they do agree with what Driehuys found in his double resonance experiments.

One possibility for this apparent discrepancy is that a significant part of a field dependence peak corresponding to a τ_c of 18μs would be below 2 G ($1/\gamma_I\tau_c \sim 2$ G) and therefore would not have been measured in the laboratory frame. One of the greatest advantages of doing an experiment either where one resonantly cross-couples between the laboratory and the proton rotating frame (our experiment) or where one resonantly cross-couples between a ^{129}Xe rotating frame and a proton rotating frame (Hartmann-Hahn matching [74]) is that the ^{129}Xe and the protons are able to interact as though they were in zero field without needing the complication of isolating the experiment from the earth's field or other stray static magnetic fields. Despite the apparent discrepancies, the basic conclusions still remains: that the surface protons are a dominant source of ^{129}Xe relaxation and that the correlation times are quite long (on the order of μs) for gaseous Xe in a SurfaSil cell.

4.3.4 Cross-coupling in Liquid Xe

After we confirmed, using gaseous Xe in a SurfaSil cell, that we could effectively cross-couple between the ^{129}Xe in the laboratory frame and the protons in the frame rotating with the rf, we examined this cross-coupling between frames with liquid Xe in the uncoated pyrex cells. For a number of cells filled with liquid Xe and at $H_0 = 39$ G, we measured the difference in ^{129}Xe relaxation rate with and without an rf of 166.3 kHz and 10.3 G H_1 (see Fig. 4.8). A pair of measurements, with and without the rf, was made using the same sample of laser-polarized liquid Xe to avoid the slight surface variations that could occur from one run to the next. The measurements were taken at 180 and 165 K because, as seen in Fig. 4.6, the zero-field ^{129}Xe relaxation rate increased with decreasing temperature and the size of the effect we were looking

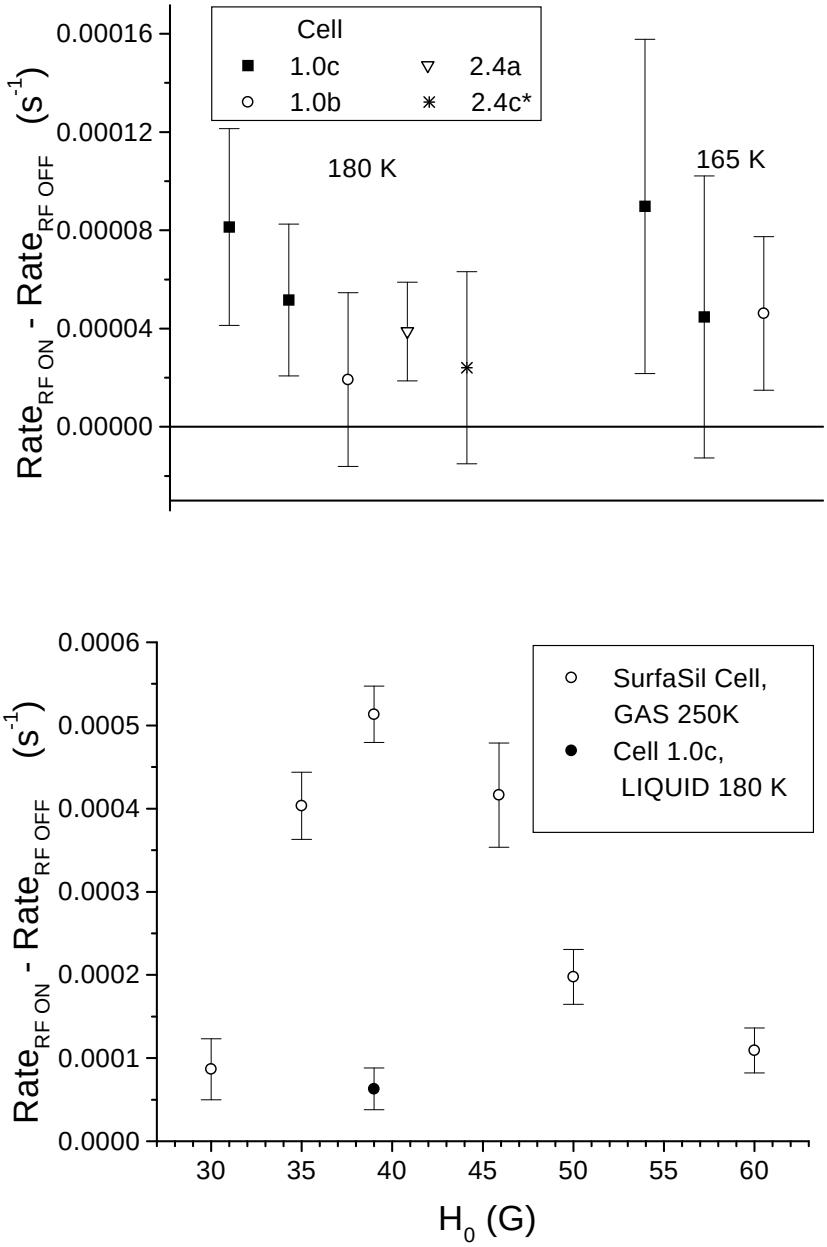

Figure 4.8: Cross-coupling between the laboratory frame and the rotating frame in liquid Xe. Graph (a) and (b) shows the difference in ^{129}Xe relaxation rates with and without an rf of 166.3 kHz and 10.3 G H_1. Graph(a) shows this difference for a number of cells containing liquid Xe. Graph(b) shows this difference for Xe gas in a Surfasil cell (○) and for liquid Xe in cell 1.0c (●).

for goes as $(3/20)(1/T_0)$. Although all cells studied gave a non-zero result, the one with the largest effect was cell 1.0c, the same cell that showed a significant field dependence below 140 G. Because of the signal to noise ratio of our signals seen in Fig. 4.8(a) we did not have the resolution to explore the relaxation in liquid as we did for gaseous Xe in SurfaSil cells at 250 K. However, we applied a rotating H_1 of 10.3 G and 166.3 kHz and measured the ^{129}Xe relaxation rate in cell 1.0c at $H_0 = 39$ G first and then at $H_0 = 60$ G, using the same sample of laser-polarized liquid Xe. The ^{129}Xe relaxation rate was higher at 39 G than at 60 G by $7.5 \pm 2.8 \times 10^{-5}$ s^{-1}. This confirmed that there was a resonance at 39 G. Using Eq. (4.16) and the fitted value of $1/T_0$ at 180 K, we calculated that the size of the effect seen in Fig. 4.8(a) should be on the order of 1×10^{-4} s^{-1}, in agreement with the observed size. Figure 4.8(b) shows for both the gas and liquid results the difference in ^{129}Xe relaxation rates with and without an rf of 166.3 kHz and 10.3 G H_1. In conclusion, the low-field ^{129}Xe relaxation rate in the liquid has a significant contribution from surface protons.

4.4 Conclusions

Using laser-polarized ^{129}Xe, we have found that ^{129}Xe lifetime in liquid Xe is on the order of 20-30 minutes and exhibits a mild dependence on magnetic field, temperature, and surface environment. The dependence of the ^{129}Xe relaxation rate on these parameters indicates that spin-rotation between pairs of Xe atoms and interaction with the surface are the main relaxation mechanisms. Furthermore, the field dependence of the ^{129}Xe relaxation rate under 100 G in some liquid Xe cells resembles the field dependence of the ^{129}Xe relaxation rate for gaseous Xe in SurfaSil-coated cells. Using a single rf tuned to the proton Larmor frequency, we match the proton Rabi frequency to the ^{129}Xe Larmor frequency. The observed increased ^{129}Xe relaxation rate at this resonant condition shows that in both the SurfaSil-coated cell and in the liquid Xe cells that there is a significant contribution to the zero-field relaxation rate of dipole-dipole coupling between surface protons and ^{129}Xe.

Chapter 5

Cross-Relaxation in Laser-Polarized Liquid Xenon

In efforts to improve their sensitivity in NMR experiments, researchers have been going to higher magnetic fields to increase the Boltzmann nuclear polarization. Dynamic polarization techniques such as the nuclear Overhauser effect (NOE) [84, 85, 86, 87, 88] have also been employed to boost the signals above their thermal levels, as well as to determine structural information [89, 90]. Optical pumping and spin exchange provide additional methods of substantially increasing nuclear polarization by four or five orders of magnitude over thermal equilibrium. In Xe ice, the large nuclear polarization of hyperpolarized ^{129}Xe has been transferred to ^{131}Xe [40] and to ^{13}C in trapped CO_2 citeBowers. Hyperpolarized ^{129}Xe has also been used to enhance the NMR of surface spins citeLong,Room,Driehuys93,Gaede,Pietrass, Brunner98. Cross-relaxation between dissolved ^{129}Xe and ^{1}H of the liquid benzene solvent has been shown to enhance the ^{1}H polarization by a factor of 0.1 to 2 at 42 kG and room temperature citeNavon. Such cross-relaxation from laser-polarized nuclei has been called the spin polarization-induced nuclear Overhauser effect (SPINOE) [32]. We demonstrate in this Chapter that with hyperpolarized liquid Xe as the *solvent* [36, 37], cross-relaxation to other spins in solution yields enhancements of up to 74 at 14 kG and 200 K. In addition, we have also observed different enhancements for nonequivalent spin sites within the same molecule. A portion of the material in this chapter was published in a slightly different form in Ref. [38].

5.1 Overview

We have examined cross-relaxation from ^{129}Xe to ^{1}H in cyclopentane and toluene and to ^{13}C in CS_2. Typical data for an enhancement run are shown in Fig. 5.1(a). This particular run, with cyclopentane dissolved in liquid Xe of natural isotopic composition, had a ^{1}H number density of 6.9 mmol/cm^3 and a ^{129}Xe number density of 5.8 mmol/cm^3. The initial ^{129}Xe polarization was 16%. The ^{1}H NMR signal reached its peak value A_p at a time $t_p = 94$ s after the sample was inserted into the dewar, and then relaxed back down to its thermal equilibrium value A_0 (dashed line) at a rate of $(18.7 \pm 0.2 \text{ min})^{-1}$. The enhancement of the NMR signal, given by $(A_p - A_0)/A_0$, was 30 ± 2. Displayed in Fig. 5.1(b) is the ^{129}Xe NMR signal from the same run. The steep descent near $t = 0$ is due to the Xe entering the vapor phase and leaving the NMR measurement coil. After the initial build-up of polarization of ^{1}H, the ^{129}Xe and ^{1}H have, within error, the same relaxation rate towards thermal equilibrium.

The evolution of our two-spin system is governed by what are known as the Solomon equations [32, 54, 88]

$$\begin{aligned} \frac{d\langle I_z(t)\rangle}{dt} &= -\varrho_I(\langle I_z(t)\rangle - I_0) - \sigma_{IK}(\langle K_z\rangle - K_0) \\ \frac{d\langle K_z(t)\rangle}{dt} &= -\varrho_K(\langle K_z(t)\rangle - K_0) - \sigma_{KI}(\langle I_z\rangle - I_0). \end{aligned} \tag{5.1}$$

The expectation values $\langle I_z(t)\rangle$ and $\langle K_z(t)\rangle$ are the polarizations of the spin I (^{1}H) and the spin K (^{129}Xe); I_0 and K_0 are their equilibrium values. ϱ_I and ϱ_K are the autorelaxation rates of the ^{1}H and ^{129}Xe spins. For $I = K = 1/2$ and dipole-dipole coupling, the cross-relaxation rates σ_{IK} and σ_{KI} are constant, independent of $\langle I_z\rangle$ and $\langle K_z\rangle$, and, as discussed in Chapter 2, are related by $\sigma_{IK} = (N_K/N_I)\sigma_{KI}$, where N_K and N_I are the number densities of spin K and spin I. As also discussed in Chapter 2, in the fast motion limit $\sigma_{KI} = \varrho_K^{KI}/2$, where ϱ_K^{KI} is that part of the ^{129}Xe autorelaxation rate due to dipole-dipole coupling with the protons.

Because dipole-dipole coupling between protons produces ^{1}H relaxation rates $\sim (10 \text{ sec})^{-1}$, while the observed relaxation rates are on the order of $(20 \text{ min})^{-1}$, similar to the relaxation rate of neat liquid Xe, we expect $\varrho_I \gg \varrho_K, \sigma_{IK}, \sigma_{KI}$. In this limit, as shown in Chapter 2, the solution to the coupled equations (5.1) gives, for all times $t \gg \varrho_I^{-1}$,

$$\langle I_z(t)\rangle - I_0 = -\frac{N_K}{2N_I}\frac{\varrho_K^{KI}}{\varrho_I}(\langle K_z(t)\rangle - K_0), \tag{5.2}$$

with the eigenvalue ϱ_K, so that both the ^{1}H and ^{129}Xe polarizations relax exponentially back to thermal equilibrium at the rate ϱ_K.

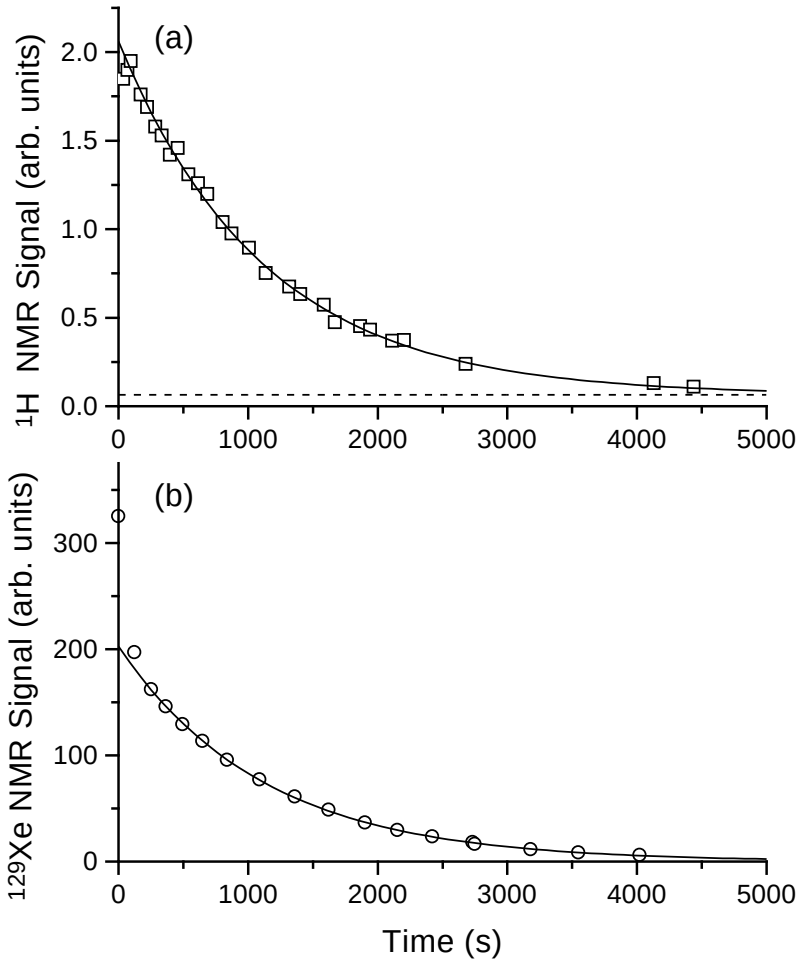

Figure 5.1: (a) Time dependence of an enhanced ^{1}H NMR signal for cyclopentane dissolved in hyperpolarized liquid Xe at 200 K and 1.4 T. The peak signal A_p occurred at a time $t_p = 94$ s after the sample was inserted in the 200 K dewar. The signal relaxed toward its equilibrium value A_0 (dashed line) at a rate of $(18.7 \pm 0.2 \text{ min})^{-1}$. The enhancement, $(A_p - A_0)/A_0$, was 30 ± 2. (b) The ^{129}Xe NMR signal from the same sample. The initial 16% ^{129}Xe polarization decayed at the same rate as the ^{1}H polarization. The steep descent near $t = 0$ is due to Xe entering the vapor phase and leaving the coil.

One can see from Eq. (5.2) that the polarization of the ^{1}H should be antiparallel to the ^{129}Xe polarization. We have verified this experimentally by observing the relative orientations of the ^{129}Xe and enhanced ^{1}H magnetization in single-coil Adiabatic Fast Passage sweeps. For spin 1/2 particles the magnetization of the sample is given by

$$M = N\gamma\hbar P/2 \tag{5.3}$$

where N is the number of the spins, γ is the gyromagnetic ratio, and P is their polarization. Because the ^{129}Xe gyromagnetic ratio γ_K is negative and the ^{1}H gyromagnetic ratio γ_I is positive, Eq. (5.2) and (5.3) together predict that the orientation of the ^{129}Xe magnetization should be parallel to the proton magnetization. During an AFP measurement, the angle between the magnetization and H_{eff} remains constant. As the static magnetic field H_0 is swept through the resonant field $H_0 = \omega_{rf}/\gamma_S$ for spin S, the magnetization rotates with the applied rf, creating an AFP signal. During a single-coil AFP measurement, where the rf is applied through the same coil through which the spins are detected, the phase of the signal relative to the applied linear rf is recorded. Using a 113 kHz tuned circuit, we took an AFP measurement of both the ^{129}Xe and the proton magnetization by changing H_0 so that the rf frequency is equal to the appropriate Larmor frequency. The relative phase between the ^{129}Xe and the ^{1}H signals was approximately zero, confirming that the ^{1}H polarization is antiparallel to the ^{129}Xe polarization.

5.2 ^{129}Xe Autorelaxation Rate

The ^{129}Xe autorelaxation rate ϱ_K can be expressed as the sum of two contributions,

$$\varrho_K = \varrho_K^0 + \varrho_K^{KI}, \tag{5.4}$$

where ϱ_K^{KI} is the contribution from dipole-dipole coupling to the protons in solution and ϱ_K^0 is the relaxation rate from Xe-Xe spin rotation, surface, and all other interactions, including exchange with the gas phase. Because dilution by the solute in our samples decreased the Xe number density by less than 15%, we can as a first approximation neglect the density dependence of the Xe-Xe coupling and treat ϱ_K^0 as a constant. We can therefore approximate ϱ_K^{KI} as the difference between the measured ^{129}Xe relaxation rate and that of neat liquid Xe. The dipole-dipole coupling rate ϱ_K^{KI} should be proportional to the ^{1}H number density N_I, and we indeed observed in our cyclopentane-Xe solutions a linear dependence of the total ^{129}Xe autorelaxation rate

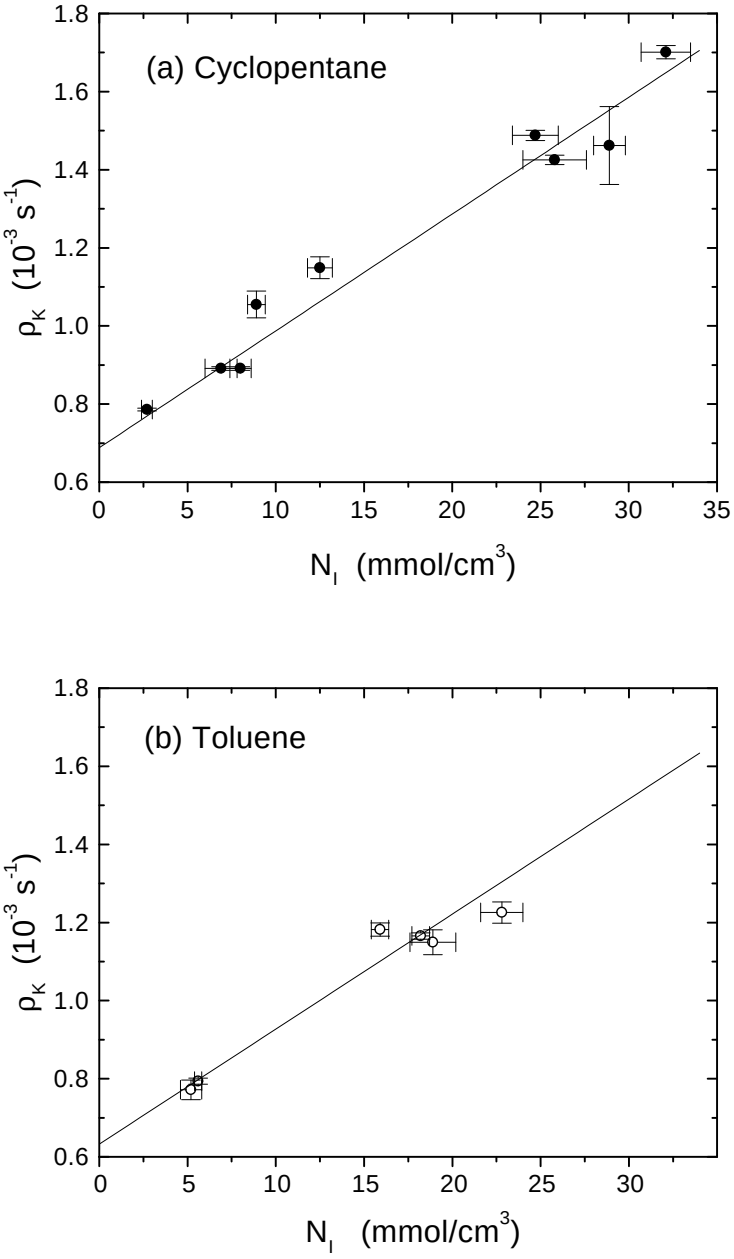

Figure 5.2: Linear dependence of the ^{129}Xe autorelaxation rate ϱ_K on the ^{1}H number density N_I for (a) cyclopentane and (b) toluene dissolved in liquid Xe at 200 K.

ϱ_K on N_I, as shown in Fig. 5.2(a). A least-squares linear fit to the data yields an intercept $\varrho_K^0 = (6.9 \pm 0.2) \times 10^{-4}$ s^{-1}, which agrees well with our previously measured ^{129}Xe relaxation rate of $(6.77 \pm 0.04) \times 10^{-4}$ s^{-1} for neat liquid Xe in uncoated pyrex containers at 200 K and 14 kG. The slope of the observed density dependence is in very good agreement with the theoretical expectation for dipole-dipole coupling between ^{1}H and ^{129}Xe. The contribution to the ^{129}Xe autorelaxation rate from dipole-dipole coupling to ^{1}H is given in the fast motion limit by citeAbragam

$$\varrho_K^{KI} = \frac{4\pi}{15}\hbar^2\gamma_K^2\gamma_I^2\frac{N_A N_I}{dD}, \tag{5.5}$$

where N_A is Avogadro's number, N_I is the number density of ^{1}H in mol/cm^3, d is the minimum internuclear separation distance, and D is the diffusion constant of the solution. Using $d \approx 3$ Å and $D \approx 3 \times 10^{-5}$ cm^2/s (the value for pure liquid Xe at 200 K citeEhrlich), we obtain a coefficient for the density dependence of 2×10^{-5} cm^3/(mmol s), compared to the value $(3.0 \pm 0.2) \times 10^{-5}$ cm^3/(mmol s) from the least-squares fit of the data in Fig. 5.2.

Figure 5.2(b) shows the linear dependence of ϱ_K on N_I as seen for liquid Xe with toluene dissolved in it. A least-squares fit to this data yields an intercept $\varrho_K^0 = (6.3 \pm 0.3) \times 10^{-4}$ s^{-1}, in agreement with both our data for cyclopentane and our data for neat liquid Xe in uncoated pyrex containers at 200 K and 14 kG. The value of the slope in Fig. 5.2(b) from a least-squares fit is $(2.9 \pm 0.2) \times 10^{-5}$cm^3/(mmol s), also in agreement with the cyclopentane data in Fig. 5.2(a) and the predictions given by dipole-dipole coupling between protons and ^{129}Xe. The linear dependence of ϱ_K on N_I, seen for both cyclopentane and toluene, demonstrates that we have not reached the saturation point of solubility in liquid Xe for these two substances.

5.3 ^{1}H Autorelaxation Rate

We measured the autorelaxation rate of the protons ϱ_I after destroying the large non-equilibrium Xe polarization. The ^{1}H autorelaxation rate ϱ_I is dominated by proton-proton coupling and can be expressed as the sum of a constant intramolecular contribution plus an additional intermolecular term proportional to the proton number density N_I. Figure 5.3 shows the least-squares fit of the measured ϱ_I in cyclopentane dissolved in liquid Xe to $\varrho_I = [(41 \pm 4) \times 10^{-3}$ s$^{-1}] + [(1.4 \pm 0.3) \times 10^{-3}$ cm^3/(mmol s)$]N_I$. The contribution ϱ_I^{IK} from dipole-dipole coupling between ^{1}H and ^{129}Xe is negligible.

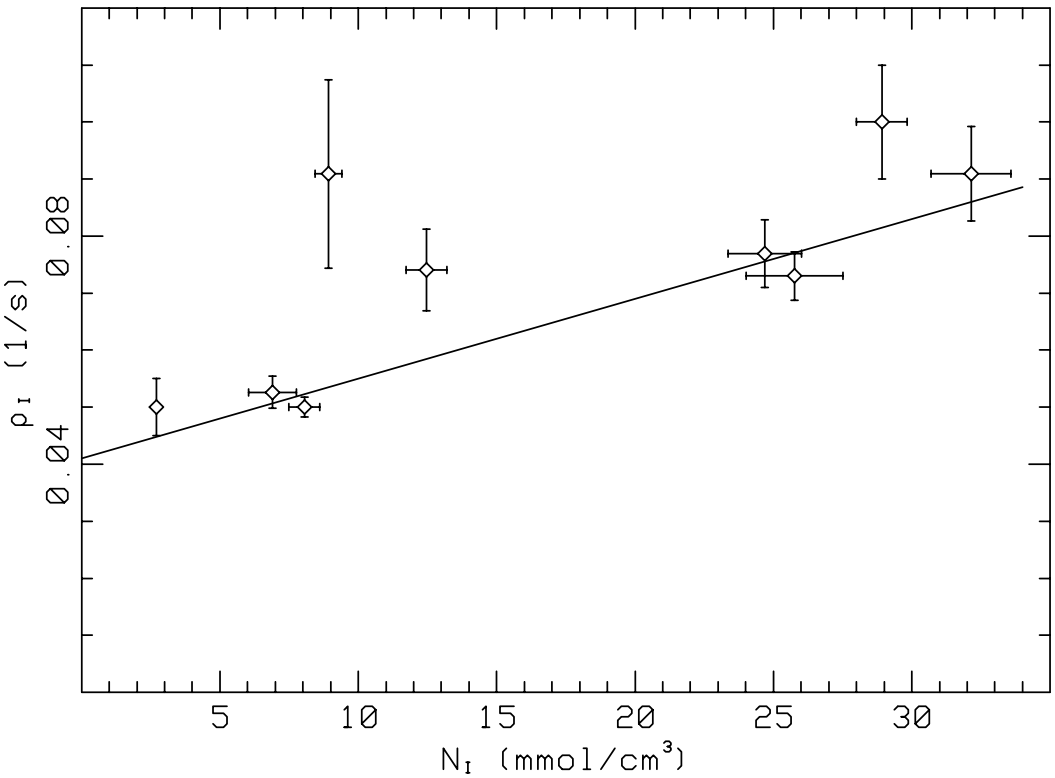

Figure 5.3: ^{1}H autorelaxation rate vs ^{1}H number density for cyclopentane dissolved in liquid Xe.

5.4 Measured and Calculated Enhancements

For our experiments with cyclopentane, ϱ_I was typically measured to be on the order of (20 sec)$^{-1}$, while ϱ_K, ϱ_K^{KI}, and hence σ_{IK} and $\sigma_{KI} \sim$ (1000 sec)$^{-1}$. Thus we are indeed in the limit $\varrho_I \gg \varrho_K, \sigma_{IK}, \sigma_{KI}$. The enhancement of our proton signal should therefore be well described by Eq. (5.2). The fractional enhancement is defined as the non-equilibrium polarization Eq. (5.2), normalized to the thermal polarization:

$$\frac{\langle I_z(t)\rangle - I_0}{I_0} = -\frac{N_K}{2N_I}\frac{\varrho_K^{KI}}{\varrho_I}\frac{\gamma_K}{\gamma_I}\frac{\langle K_z(t)\rangle}{K_0}. \tag{5.6}$$

Here $\langle K_z(t)\rangle - K_0$ has been approximated by $\langle K_z(t)\rangle$ since $\langle K_z(t)\rangle$ is five orders of magnitude larger than K_0 at 200 K and 14 kG. In Table 5.4 we compare the measured fractional enhancements for several samples, corresponding to the maximum observed proton signals (at times t_p), with those calculated from Eq. (5.6) using the sample parameters listed. Note that the calculations used the ^{129}Xe polarizations at the

times t_p of the peak ^{1}H signals. There is good agreement between the measured enhancements and the enhancements calculated by Eq. (5.6).

Fractional Enhancements		
Run #	Measured	Calculated (from Sample Parameters)
1	45 ± 1*	40 ± 4*
2	41 ± 3*	31 ± 5*
3	22 ± 1	23 ± 3
4	32 ± 2	52 ± 14
5	30 ± 2	37 ± 6
6	25 ± 1	29 ± 4

Sample Parameters					
Run #	$P_{\mathrm{Xe}}(t_p)$ (%)	N_K (mmol/cm^3)	N_I (mmol/cm^3)	ϱ_K^{-1} (min)	ϱ_I^{-1} (sec)
1	$12.4 \pm .8$	11 ± 1*	26 ± 2	$11.7 \pm .1$	$13.7 \pm .8$
2	13 ± 1	$9.6 \pm .8$*	32 ± 1	$9.8 \pm .1$	11 ± 1
3	$16.5 \pm .9$	$4.7 \pm .3$	25 ± 1	$11.2 \pm .1$	13 ± 1
4	$15.0 \pm .6$	$5.6 \pm .4$	$2.7 \pm .3$	$21.2 \pm .1$	20 ± 2
5	$14.7 \pm .9$	$5.8 \pm .7$	$6.9 \pm .9$	$18.7 \pm .1$	19 ± 1
6	$14.3 \pm .7$	$5.1 \pm .2$	$8.0 \pm .6$	$18.7 \pm .1$	$20.0 \pm .7$

Table 5.1: Measured and calculated fractional enhancements of ^{1}H for cyclopentane dissolved in hyperpolarized liquid Xe at 200 K and 14 kG. Also given are the sample parameters needed for the calculation [see Eq. (5.6)]. The listed Xe polarizations P_{Xe} are for the times t_p at which the maximum proton signals were measured. The runs marked by (*) used Xe enriched to 71% ^{129}Xe.

Knowing the functional form for the ^{1}H enhancement, we can determine the conditions for its optimization. The explicit $1/N_I$ dependence of Eq. (5.6) is cancelled by the proportionality of ϱ_K^{KI} to proton density. The fractional proton enhancement is therefore explicitly proportional to the ^{129}Xe number density N_K and the ^{129}Xe polarization. There is still an implicit dependence on N_I, however, because of the linear dependence of ϱ_I on proton density. Thus for a given solute, the greatest enhancements come from having a large ^{129}Xe number density (as can be obtained by using Xe isotopically enriched with ^{129}Xe), a large ^{129}Xe polarization, and a small ^{1}H number density. For example, the first two runs listed in Table 1, done with Xe enriched to 71% ^{129}Xe (a factor of 2.7 higher than in the natural Xe used for the rest of the runs), showed the greatest enhancements.

Although a small ^{1}H number density does reduce ϱ_I and therefore increase the proton enhancement, for a *fixed* amount of laser-polarized ^{129}Xe the total proton NMR signal (enhancement $\times$ number of protons) is maximized by dissolving in the liquid Xe as much of the solute as available. Therefore this technique is most important for a solute of which there is only a small fixed quantity to examine, as in the case when the solute is rare or expensive. The next section discusses the examination of such an expensive sample, CS_2 enriched in ^{13}C citeCDS.

5.5 Cross-Relaxation to ^{13}C

Cross-relaxation in hyperpolarized liquid Xe is not limited to ^{1}H. We have also measured a fractional enhancement of 74 ± 7 for ^{13}C in $^{13}CS_2$. The sample had a ^{13}C number density of 3.5 ± 0.1 mmol/cm^3, a ^{129}Xe polarization of 10.6 ± 0.6% at the time t_p of the peak ^{13}C signal, and a ^{129}Xe number density of 12.8 ± 0.6 mmol/cm^3 reflecting the enriched Xe used. The measured ^{129}Xe lifetime of 22.8 ± 0.8 min, close to that of neat liquid Xe, indicates that the cross-relaxation rate is small, perhaps due to the small gyromagnetic ratio of the ^{13}C (the ^{13}C gyromagnetic ratio is four times smaller than the proton gyromagnetic ratio). The enhancement was aided by the small ^{13}C autorelaxation rate; we measured ϱ_I to be $(100 \pm 20 \text{ sec})^{-1}$ for neat $^{13}CS_2$ at 200 K, in agreement with Ref. [97]. (Because 95% of sulfur is spin 0, the main relaxation mechanisms of ^{13}C in $^{13}CS_2$ can only be through spin rotation and chemical shift anisotropy.) The ability to produce such a significant enhancement of ^{13}C in spite of its small gyromagnetic ratio demonstrates the potential of this technique.

5.6 Differential Enhancement

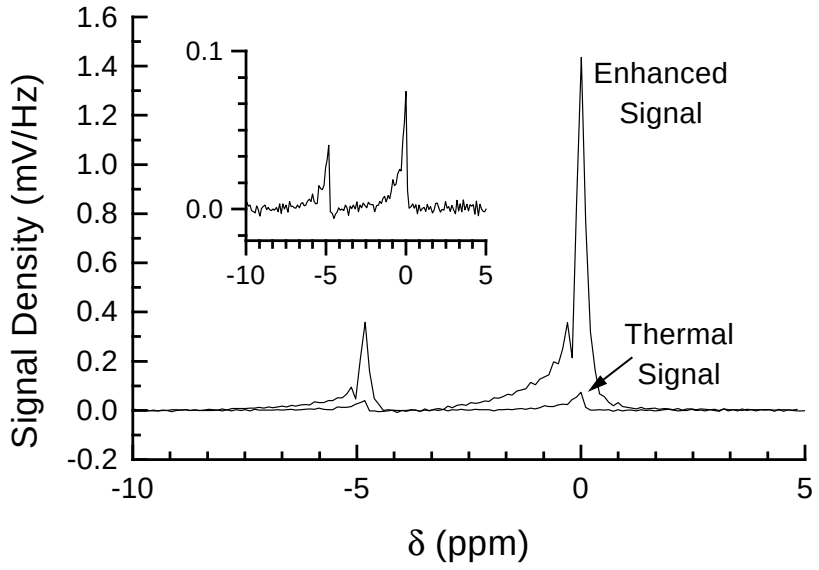

Figure 5.4: Enhanced and thermal ^{1}H spectra for toluene dissolved in hyperpolarized liquid Xe at 200 K and 14 kG, obtained with 90° pulses. The ratio of the areas of the ring proton signal (right peak) to the methyl was 4:1 in the enhanced spectrum, compared to the 5:3 area ratio of the thermal spectrum (magnified in inset). The ring proton signal was preferentially enhanced by 16, compared to a factor of 6 for the methyl.

In addition to producing very large enhancements, cross-relaxation with hyperpolarized liquid Xe can also provide *differential enhancement* of nonequivalent spins on the same molecule in solution. In toluene, we observed preferential enhancement of the five ring protons over the three methyl protons. Figure 5.6 shows the enhanced spectrum of toluene dissolved in hyperpolarized liquid Xe. The ratio of the areas of

the ring to the methyl protons is 4:1. In contrast, the thermal equilibrium spectrum of toluene, measured in the same sample after the ^{129}Xe polarization had been destroyed, shows the areas in the expected ratio of 5:3 (inset, Fig. 5.6). This difference in area ratios reflects the fractional enhancement of the ring protons by 16 and the methyl protons by only 6 (for a ^{129}Xe polarization of only 7% at time t_p). The preferential enhancement of the ring over the methyl protons may be partially attributed to their different autorelaxation rates: $\varrho_I = (21 \pm 1 \text{ sec})^{-1}$ for the ring protons and $(6.1 \pm 0.7 \text{ sec})^{-1}$ for the methyl protons of the diluted toluene in this sample. (For comparison, in neat toluene at 200 K, the intramolecular T_1 of the ring protons is ~ 10 s and that of the methyl protons is ~ 5 s [98].) A complete model, however, needs to include the coupling between the ring and methyl protons. Differential enhancement has also been observed for laser-polarized Xe dissolved in a solution of α-cyclodextrin [99]. α-cyclodextrin has a Xe binding site so that protons closer to the binding site had greater signal enhancements .

In the limit $\varrho_I \gg \varrho_K, \sigma_{IK}, \sigma_{KI}$, the lifetime of the enhanced ^{1}H signal is given by ϱ_K^{-1}, but the enhanced signal is established on the time scale of ϱ_I^{-1}. Consequently, large pulse angles can be used to sample the enhanced spins with improved signal-to-noise. The enhanced signal will be restored relatively quickly and without significant depolarization of the ^{129}Xe. For example, we have been able to follow the time evolution of the enhanced spectrum of toluene using 90° pulses about 2 min ($\sim 6\varrho_I^{-1}$) apart.

5.7 Conclusions

We have demonstrated the large enhancements of ^{1}H and ^{13}C NMR signals that are possible from cross-relaxation in solution with hyperpolarized liquid Xe. Although we have focused on liquid solutes, this method should be readily extendible to dissolved solids and gases. The measured cross-relaxation rates and fractional enhancements are in quantitative agreement with theoretical calculations. Furthermore, we have observed preferential enhancement of different proton sites on the same molecule. The ability to produce substantial enhancements with long lifetimes, and the added potential of possible structural and dynamics information from preferential enhancements, should make cross-relaxation by solution in hyperpolarized liquid Xe a valuable new spectroscopic tool for NMR of biological and other molecules.

Appendix A

Coatings

The purpose of this Appendix is to catalog cells that were made when exploring the interaction of gaseous ^{129}Xe with surfaces. Hopefully some of this work will be useful to those looking for good coatings or just looking for cells they can use for their own experiments. All measurements shown in this Appendix were done at room temperature, and all pressures given in the following tables of natural Xe or N_2 are for $T \sim 24$°C. The preparation of the cells with either hydrocarbon or silicone coatings included a bake out for about a day between 100° and 150°C as the cells were evacuated to approximately 10^{-8} torr. Afterwards the cells were filled with natural Xe, N_2, and Rb and then sealed. All cells in this Appendix were made and measured in 1995-1996.

A.1 Curing of Rb on Pyrex

The ^{129}Xe lifetime T_1 of gaseous Xe in a sealed pyrex cell, coated with nothing more than the Rb used for optical pumping, typically increases with aging of the cell [100]. We call this effect "curing", and it is often accelerated by the application of heat to the cell. The set of cells in Table A.1 were "pre-cured": before being filled with Xe and N_2 and subsequently sealed, the cells containing the Rb were baked at 60°C for 17 hours while being pumped on. Prior to the distillation of the Rb into the cells, the cells were evacuated to approximately 10^{-8} torr while being heated to about 500°C for 2 days. Table A.1 shows the ^{129}Xe lifetimes in these 4 cm^3 pyrex cells after the cells were first sealed. The cells were measured periodically over a period of about two weeks while being heated at 140°C. The cells showed an intial rapid change as evidenced by increasing ^{129}Xe lifetimes. After $2\frac{1}{2}$ days at 140°C, the ^{129}Xe lifetimes

Cell #	P Xe (torr)	P N_2 (torr)	Initial T_1 (s)	Final T_1 (s)
175A	990	70	540 ± 10	3000 ± 200
176A	4300	70	1550 ± 120	3200 ± 200
177A	2400	69	1050 ± 40	3100 ± 200
178A	6200	71	730 ± 30	—
179A	7400	73	~ 300	2490 ± 160

Table A.1: Rb on bare pyrex. The initial ^{129}Xe T_1's were measured after the cells were first sealed. The final T_1's are the equilibrium values reached after the cell had been heated at 140°C for over $2\frac{1}{2}$ days.

reached their equilibrium values shown in Table A.1. The unusually long lifetimes achieved (42-53 minutes) indicate that the concept of "pre-curing" may be a useful one.

A.2 Hydrocarbon Coatings and their Deuterated Counterparts

As shown both in Chapter 4 in this thesis and in Ref. [31], the ^{129}Xe relaxation rate for gaseous Xe in a SurfaSil-coated cell [83] at low magnetic fields is dominated by dipole-dipole coupling between the ^{129}Xe and protons in the coating. The relaxation rate associated with this contribution is proportional to $\gamma_I^2\gamma_K^2 I(I+1)$ (see Chapter 2) where I is the spin of the ^{1}H nucleus and K is the spin of the ^{129}Xe nucleus. If all the hydrogens in the coating could be replaced by deuterons, and assuming dipole-dipole coupling to be the only relaxation mechanism for ^{129}Xe, then the ^{129}Xe relaxation rate should be reduced by a factor of 16. While the full factor of 16 improvement is not usually achieved, significant enhancements can come from using deuterated coatings. For example, Bouchiat and Brossel [101] found that the Rb electron spin relaxation was reduced by a factor of 5 by replacing paraffin with deuterated paraffin as the cell coating.

Cell #	P Xe (torr)	P N_2 (torr)	Coating	8 G T_1 (s)	94 G T_1 (s)	τ_c (μs)
198A	741	72	h-Ps	—	~ 50	—
199A	698	73	65% h-Ps, 35% d-Ps	—	~ 50	—
200A	1270	74	33% h-Ps, 67% d-Ps	—	75 ± 4	—
201A	1963	73	d-Ps	—	95 ± 4	—
203A	836	73	d-Ps	—	56 ± 6	—
239A	740	70	d-polyphenylene	103 ± 3	360 ± 50	7 ± 3
240A	746	71	d-polyphenylene	~ 110	—	—
241A	724	71	polyphenylene	74 ± 5	—	—
242A	815	71	polyphenylene	97 ± 5	—	—
243A	772	72	d-polyphenylene	88 ± 1	—	—
266A	735	72	paraflint	340 ± 10	—	—
267A	714	77	paraflint on SurfaSil	510 ± 10	—	—
268A	846	70	paraflint on TMCS	120 ± 10	—	—
269A	714	72	d-paraffin	160 ± 10	—	—
270A	709	70	d-paraffin on SurfaSil	1160 ± 20	—	—
271A	730	72	d-paraffin on TMCS	72 ± 3	—	—

Table A.2: Hydrocarbons and their deuterated counterparts. Cells 198A – 203A were coated with polystyrene (h-Ps) and deuterated polystyrene (d-Ps). The polyphenylene and deuterated polyphenylene coatings were created as discussed in the text. The correlation time τ_c is from the fit of the data to a model of dipole-dipole coupling between ^{129}Xe and deuterons. The paraflint and deuterated paraffin coatings were applied according to the procedures in Ref. [102].

We first studied hydrocarbon coatings and their deuterated counterparts because the deuterated hydrocarbons were more readily available than deuterated silanes. In order to form a coating from polystyrene and deuterated polystyrene, a 10% – 20% solution of polystyrene (h-Ps) or deuterated polystyrene (d-Ps) (or some mixture of the two) in toluene was applied to the surface of a 1 cm^3 pyrex cell. The ^{129}Xe

lifetimes in these polystyrene coated cells were too short to measure at 8 G. The ^{129}Xe lifetimes at 94 G were not significantly different in cells coated with h-Ps than in cells coated with d-Ps, indicating that dipole-dipole coupling with protons in the polystyrene coating is not the dominant source of ^{129}Xe relaxation at 94 G.

The polyphenylene coatings were made by running a discharge through 1-2 torr of benzene or deuterated benzene in argon (90% argon by pressure). These coating did not stand up very well to heat, making it hard to draw conclusions about the results. While sealing the cell with a torch, the coating close to the seal turned brown and black, indicating that these coatings had been considerably altered in the presence of high heat.

Like Bouchiat and Brossel [101], we also examined deuterated paraffin $(CD_2)_n$, which is closer to the linear structure of SurfaSil than either of the two aromatic coatings discussed above. Because of the high boiling point (230°C – 260°C) of the deuterated paraffin commercially available, the deuterated paraffin could not be simply melted down onto the surface without decomposition of the alkane chains. Therefore the procedure outlined by Bartle and Meyer [102] was used. Some of the pyrex surfaces were pre-coated with either SurfaSil or trimethylchlorosilane (TMCS) in order to provide hydrophobic surfaces for the paraffin to stick to (see Table A.2). The paraflint $(CH_2)_n$ was applied in the same manner as the deuterated paraffin. Again, there appeared to be no significant difference in ^{129}Xe lifetimes in cells with the deuterated and the non-deuterated paraffin coatings, indicating that other relaxation mechanisms dominate over dipole-dipole coupling of the surface protons and ^{129}Xe.

A.3 SurfaSil

Typically SurfaSil [83] was applied to a surface by rinsing the surface with a 10% solution of SurfaSil in cyclohexane. The results of variation in subsequent surface treatment are shown in Table A.3. One of the observed trends is that the ^{129}Xe lifetimes in cells that were heated in air (one day at 140°C) after being coated with SurfaSil were as long or longer than cells that were not heated in air. Perhaps the heat speeds up the reaction of the coating with glass or enables the SurfaSil to cross-link with itself, creating a less penetrable coating to Xe. Cross-linking, where different chains of SurfaSil bind not only to the surface but also to each other, has been observed with dimethyldichlorosilane on silica surfaces by Sindorf and Maciel [103].

We tried to deuterate the SurfaSil coating by running a discharge through 1-2 torr

Cell #	P Xe (torr)	P N_2 (torr)	Coating	8 G T_1 (s)	94 G T_1 (s)	τ_c (μs)
187A	715	67	SurfaSil, DMCS,	620 ± 80	410 ± 30	—
188A	~ 700	68	and H_2O	290 ± 10	660 ± 150	—
189A	709	73	SurfaSil, DMCS,	2520 ± 140	4000 ± 200	1.7 ± 1.1
190A	704	73	and heat in air	2650 ± 190	2850 ± 150	—
191A	~ 3950	67	SurfaSil	~ 200	1050 ± 50	3.1 ± 0.1
192A	757	67	and DMCS	240 ± 20	770 ± 30	2.2±0.3
220A	714	76	SurfaSil	1600 ± 100	4200 ± 500	3.5 ± 0.5
221A	735	98		1020 ± 50	—	—
222A	719	72	SurfaSil and	1250 ± 130	2900 ± 200	3.3 ± 0.5
223A	741	86	heat in air	3890 ± 140	4560 ± 160	9 ± 3
224A	725	72	heat,migration?	4700 ± 200	5200 ± 200	7 ± 6
230A	931	71	D discharge	360 ± 30	1210 ± 70	19 ± 10
231A	740	76	D discharge	1040 ± 30	2490 ± 160	4.8 ± 0.9
232A	799	70	H discharge	700 ± 20	1672 ± 169	4.3 ± 0.5
233A	682	89	no discharge	180 ± 60	840 ± 120	3.8 ± 0.7
234A	735	76	D discharge	960 ± 40	2100 ± 300	4.0 ± 0.6
244A	750	73	coated	$2700 \pm 300*$	3400 ± 300	—
245A	750	69	by	$1480 \pm 130*$	2300 ± 200	—
246A	746	72	migrating	$2600 \pm 200*$	3100 ± 500	—
247A	825	71	SurfaSil?	$2100 \pm 200*$	2900 ± 400	—
248A	730	71	SurfaSil	$1530 \pm 150*$	3100 ± 500	—

Table A.3: Surfasil coatings. The major divisions of the cells in the above table indicate batches made at the same time (for example, 187A – 192A were made at the same time). Dimethylchlorosilane (DMCS) was applied in equal parts with SurfaSil for cells 187A – 192A. As indicated above, sometimes after the coating was applied the cells were heated in air at 140°C for about 24 hours. The ^{129}Xe lifetimes marked by $*$ were measured at about 1 G.

of deuterium inside the Surfasil-coated cells 230A, 231A, and 234A. Cells 230A – 234A were all coated with SurfaSil in the usual manner. Cell 233A was used as a control while cell 232A had a discharge through 1-2 torr of hydrogen inside of it. From the ^{129}Xe lifetimes it appears as though the deuteration process was unsuccessful. Moreover, all the coatings had noticeable cracks caused by the discharge that might have degraded the quality of the coating.

The SurfaSil coating was found to migrate when under vacuum to other uncoated surfaces. In one string, cell 248A was coated with SurfaSil while the cells 244A – 247A were left uncoated. After the cells were baked out under vacuum at 150° C for two and a half days, Rb was distilled into the cells. By their interaction with Rb, all of the cells looked coated; they turn white in the presence of Rb. Moreover, all of the cells exhibited field dependence in the ^{129}Xe relaxation rate below 100 G which is characteristic of coated cells, but uncharacteristic of an uncoated cell. The ^{129}Xe lifetimes in the cells coated by migration were as long or longer than in the cell coated by rinsing with SurfaSil (see Table A.3). SurfaSil is made up of a distribution of chain lengths of chlorine-terminated siloxanes. One can imagine that the shorter chains migrate and form a thinner coating. The evolution of the ^{129}Xe lifetime in cells 244A, 246A, and 248A under application of heat was studied. At temperatures below 100°C the ^{129}Xe lifetimes in cells 244A and 246A increased while in cell 248A they did not change. However, at high temperatures, both the coating by migration and the coating by rinsing seemed unstable. After cells 246A and 248A were kept at 144°C for 96 hours the ^{129}Xe lifetimes in these cells significantly decreased to less than 11 minutes.

A.4 Dimethyldichlorosilane

SurfaSil is basically made by polymerizing dimethyldichlorosilane (DMDCS) with a controlled amount of water to get a distribution of chain lengths ending in chlorines. The migration studies of SurfaSil seem to indicate that it might be worthwhile to examine some of the shorter components of SurfaSil, like dimethyldichlorosilane. DMDCS has the added benefit that it is easier to deuterate than the longer chains in SurfaSil. We applied DMDCS as a coating in a similar manner to SurfaSil.

Initial work with DMDCS shows that the ^{129}Xe lifetimes in cells coated with DMDCS are similar to those cells coated with SurfaSil. The correlation times associated with these DMDCS coatings look a bit shorter than SurfaSil so that it was necessary to go to higher magnetic fields to see the field dependence. For instance, although the ^{129}Xe lifetimes at 8 G and 94 G in cell 276A were both about 2800 s,

Cell #	P Xe (torr)	P N_2 (torr)	Coating	8 G T_1 (s)	94 G T_1 (s)	τ_c (μs)
272A	725	73	DMDCS migration?	140 ± 6	—	—
273A	741	78	DMDCS migration?	311 ± 10	—	—
274A	852	79	DMDCS and heat	1220 ± 50	—	—
275A	735	69	DMDCS and heat	710 ± 20	—	—
276A	741	69	DMDCS	2900 ± 100	2700 ± 300	0.6 ± 0.2
277A	735	75	DMDCS	1500 ± 100	—	—
280A	746	72	DMDCS, CH_3OH	1930 ± 60	—	—
281A	788	73	DMDCS, CH_3OH	1710 ± 150	—	—
283A	762	70	DMDCS, CD_3OD	4100 ± 400	5600 ± 300	—
284A	756	79	DMDCS	1400 ± 100	—	—
285A	825	72	DMDCS	670 ± 20	—	—
286A	762	71		2900 ± 100	—	—
287A	778	71		2520 ± 50	—	—
288A	762	71	DMDCS,CD_3OD	3240 ± 150	—	—
289A	799	71		1420 ± 40	—	—
290A	783	78		910 ± 40	—	—
291A	762	70		1670 ± 60	—	—
296A	770	71		All	—	—
297A	788	73		cells	—	—
298A	783	73	dimethyl-	are	—	—
299A	778	73	diethoxysilane	less	—	—
300A	770	74		than	—	—
301A	770	69		1 min.	—	—
302A	788	80	Coated by	120 ± 6	~ 90	—
303A	783	72	known	510 ± 20	—	—
304A	770	70	vapor	720 ± 30	—	—
305A	767	74	pressure	1130 ± 60	1450 ± 160	—
306A	751	77	of	121 ± 6	~ 140	—
307A	778	70	DMDCS	313 ± 3	—	—

Table A.4: Dimethyldichlorosilane (DMDCS) and dimethyldiethoxysilane coatings. The correlation time τ_c is extracted from fitting the ^{129}Xe relaxation rate as a function of field to a model of dipole-dipole coupling between ^{129}Xe and protons.

as seen in Table A.4, the ^{129}Xe lifetime at 1.5 kG in this cell was 4300 ± 300s. Table A.4 also shows the results for different methods of applying DMDCS. Unlike with SurfaSil, coating by migration of DMDCS did not seem to coat the surface very well, and heating the DMDCS coating in air at 140°C for a day did not seem to improve the coating at all. After applying DMDCS to the surface, a methanol or deuterated methanol rinse was tried in an effort to react any remaining chlorines. Variations from cell to cell dominated any effect the different rinses may have had.

We found with the DMDCS coating that heat changed the nature of the coating in a non-predictable way, making it difficult to do reproducible field dependence studies since we optically pumped the Rb at 80°C. As an example of the surface evolution of these cells, the ^{129}Xe lifetimes in cells 286A – 291A went from the values they have in Table A.4 to between 7 minutes and 2 hours after the being heated for 16 hours at ~ 100°C.

In an effort to control the observed variation in coatings from cell to cell, we evacuated a set of uncoated cells (cells 302A – 307A) to below 20 millitorr and baked them out at 200°C for 17 hours. We then allowed DMDCS vapor into the cells and baked them again at 200°. The resulting coating did not compare favorably with the coating done by rinsing with a solution of DMDCS. Sindorf and Maciel [103] found that surface-adsorbed water plays an important role in determining the extent to which silylation occurs. Perhaps in baking the cells before coating them we drove off some of the water necessary for forming a good coating.

We also examined another multifunctional silane, dimethyldiethoxysilane, which in principal should make a similar coating to dimethyldichlorosilane. It was deposited from an aqueous alcohol as outlined in the Gelest catalog under “Applying a Silane

Coupling Agent" [104]. This also did not provide a good coating.

A.5 Deuterated Dimethyldichlorosilane

Coating with deuterated DMDCS in comparison to DMDCS did *not* reduce the ^{129}Xe relaxation rate (see Table A.5). Neither did rinsing with deuterated methanol (after applying the deuterated DMDCS) in an effort to react the remaining chlorines with a deuterated reagent (as opposed to water in the air or water adsorbed on the surface) have any effect. We also explored applying the deuterated coating in a dry nitrogen environment to try to remove the effects of water vapor in the air on the coating. This also seemed to have no significant effect. These results indicate that dipole-dipole coupling between surface protons and ^{129}Xe is not the dominant relaxation mechanism in the DMDCS coating. Unfortunately, it has also been found that these DMDCS coatings evolve as a function of time. Therefore it would be very difficult to repeat with DMDCS the experiments done with SurfaSil that in that case clearly demonstrated the contribution to the ^{129}Xe relaxation rate of dipole-dipole coupling between surface protons and ^{129}Xe.

Cell #	P Xe (torr)	P N_2 (torr)	Coating	8 G T_1 (s)	94 G T_1 (s)	τ_c (μs)
320A	772	70		2500 ± 150	4000 ± 150	—
321A	772	71		2680 ± 110	—	—
322A	767	69	DMDCS-d_6†	420 ± 30	470 ± 20	—
323A	772	68		700 ± 10	—	—
324A	767	69		1540 ± 60	—	—
325A	767	69		1080 ± 50	—	—
326A	772	69		1200 ± 110	1730 ± 20	21 ± 4
327A	767	73	DMDCS-d_6†	2000 ± 50	—	—
328A	767	69	and	870 ± 50	—	—
329A	794	69	CD_3OD rinse	2160 ± 130	—	—
330A	778	71		1640 ± 110	—	—
331A	762	70	migration?	1080 ± 50	—	—
334A	767	68	DMDCS-d_6‡	1270 ± 70	1380 ± 110	$2.3 \pm 0.6*$
335A	745	72	and CD_3OD	1060 ± 60	—	—
336A	767	72	rinse, in a	1360 ± 60	—	—
337A	761	73	dry nitrogen	1350 ± 40	—	—
338A	767	68	environment	1200 ± 50	—	—

Table A.5: Deuterated dimethyldichlorosilane coatings. DMDCS-$d_6^\dagger$ was prepared in collaboration with the Princeton University Chemistry Department by Richmond Sarpong. DMDCS-d_6‡ was prepared CDN isotopes with a chemical purity of 96.5% and 99.9 atom % D. The correlation times given in the table above were extracted from fitting the ^{129}Xe relaxation rates as a function of field to a model of dipole-dipole coupling between deuterons and ^{129}Xe. The correlation time marked by an $*$ is that value initially measured for the coating. However four days later the coating had evolved so that τ_c was measured to be 0.8 ± 0.2 μs.

Bibliography

[1] M.A. Bouchiat *et al.*, *Phys. Rev. Lett.* **5**, 373 (1960).

[2] 1 amagat = 2.69×10^{19} cm^{-3}, the density of an ideal gas at STP.

[3] B.C. Grover, *Phys. Rev. Lett.* **40**, 391 (1978).

[4] T.G. Walker and W. Happer, *Rev. Mod. Phys.* **69**, 629 (1997).

[5] K. Abe, *Phys. Rev. Lett.* **79**, 26 (1997).

[6] M.V. Romalis, Ph.D. thesis, Princeton University, unpublished, 1997.

[7] B. Driehuys *et al.*, *Appl. Phys. Lett.* **69**, 1668 (1996).

[8] P.L. Anthony *et al.*, Phys. Rev. Lett **71**, 959 (1993).

[9] T.E. Chupp *et al.*, *Phys. Rev. Lett.* **72**, 2363 (1994).

[10] N.R. Newbury *et al.*, *Phys. Rev. Lett.* **67**, 3219 (1991).

[11] A.K. Thompson *et al.*, *Phys. Rev. Lett.* **68**, 2901 (1992).

[12] M.S. Albert *et al.*, *Nature* **370**, 199 (1994).

[13] M. Ebert *et al.*, *Lancet* **347**, 1297 (1996).

[14] M. Leduc, P.J. Nacher, and G. Tastevin, *Laser Physics* **8**, 799 (1998).

[15] H. Middleton *et al.*, *Magn. Reson. Med.* **33**, 271 (1995).

[16] J.P. Mugler III *et al.*, *Magn. Reson. Med.* **37**, 809 (1997).

[17] M.S. Albert *et al.*, *J. Magn. Reson. B* **111**, 204 (1996).

[18] Y.-Q. Song *et al.*, *J. Magn. Reson. A* **115**, 127 (1995).

[19] R. Seydoux *et al.*, *J. Magn. Reson. A* **101**, 78 (1993) .

[20] M. Steinberg and B. Manowitz, *Ind. and Eng. Chem.* **51**, 47 (1959).

[21] H. Susskind *et al.*, *Prog. Nucl. Med.* **5**, 13 (1978).

[22] T. Pietrass and H.C. Gaede, *Adv. Mater.* **7**, 826 (1995).

[23] B.M. Goodson, *Proc. Natl. Acad. Sci. USA* **94**, 14725 (1997).

[24] S.D. Swanson *et al.*, *Magn. Reson. Med.* **38**, 695 (1997).

[25] M.E. Wagshul *et al.*, *Magn. Reson. Med.* **36**, 183 (1996).

[26] R.C. Welsh *et al.*, *Nucl. Instrum. Meth. A* **402**, 461 (1998).

[27] B.F. Chmelka *et al.*, *Phys. Rev. Lett.* **66**, 580 (1991).

[28] T. Pietrass *et al.*, *Surface Science* **334**, L730 (1995).

[29] D. Raftery *et al.*, *J. Phys. Chem.* **97**, 1649 (1993).

[30] B. Driehuys, Ph.D. thesis, Princeton University, unpublished, 1995.

[31] B. Driehuys *et al.*, *Phys. Rev. Lett.* **74**, 4943 (1995).

[32] G. Navon *et al.*, *Science* **271**, 1848 (1996).

[33] E. Brunner *et al.*, *J. Magn. Reson.* **130**, 145 (1998).

[34] H.W. Long *et al.*, *J. Am. Chem. Soc.* **115**, 8491 (1993).

[35] T. Rõõm *et al.*, *Phys. Rev. B* **55**, 11604 (1997).

[36] P.M. Rentzepis and D.C. Douglass, *Nature* **293**, 165 (1981).

[37] M.B. Sponsler *et al.*, *J. Am. Chem. Soc.* **111**, 6841 (1989).

[38] R.J. Fitzgerald, K.L. Sauer, and W. Happer, *Chem. Phys. Lett.* **284**, 87 (1998).

[39] G.R. Davies *et al.*, *Chem. Phys. Lett.* **230**, 237 (1994).

[40] M. Gatzke *et al.*, *Phys. Rev. Lett.* **70**, 690 (1993).

[41] D.M. TonThat *et al.*, *Chem. Phys. Lett.* **272**, 245 (1997).

[42] V.A. Rabinovich *et al.*, *Thermophysical Properties of Neon, Argon, Krypton, and Xenon* (Hemisphere Publishing Corporation, Washington, 1988).

[43] H.C. Torrey, *Phys. Rev.* **130**, 2306 (1963).

[44] E.R. Hunt and H.Y. Carr, *Phys. Rev.* **130**, 2302 (1963).

[45] X. Zeng *et al.*, *Phys. Rev. A* **96**, 191 (1983).

[46] G.D. Cates *et al.*, *Phys. Rev. A* **37**, 2877 (1988).

[47] R.L. Gamblin and T.R. Carver, *Phys. Rev.* **138**, A946 (1965).

[48] L.D. Schearer and G.K. Walters, *Phys. Rev.* **139**, A1398 (1965).

[49] M. Gatzke, Ph.D. thesis, Princeton University, unpublished, 1992.

[50] I. Oppenheim, M. Bloom, and H.C. Torrey, *Can. J. Phys.* **42**, 70 (1964).

[51] R.S. Ehrlich and H.Y. Carr, *Phys. Rev. Lett.* **25**, 341 (1970).

[52] P.W. Peereboom *et al.*, *Physica A* **156**, 260 (1989) .

[53] D.R. Lide, ed., in: *CRC Handbook of Chemistry and Physics 1995-1996* (CRC Press, Boca Raton, 1995).

[54] A. Abragam, *The Principles of Nuclear Magnetism* (Oxford University Press, New York, 1961).

[55] L. Banci, *et al.*, *Nuclear and Electron Relaxation* (VCH Publishers, New York, 1991).

[56] N. Bloembergen, *et al.*, *Phys. Rev.* **73**, 679 (1947).

[57] C.P. Slichter, *Principles of Magnetic Resonance* (Springer-Verlag, New York, 1990).

[58] W. Happer, *Spin Relaxation*, unpublished notes (1994); R. Fitzgerald, *Spin Relaxation Addendum*, unpublished notes (1998).

[59] M.E. Rose, *Elementary Theory of Angular Momentum* (John Wiley and Sons, New York, 1957).

[60] N.D. Bhaskar *et al.*, *Phys. Rev. Lett.* **49**, 25 (1982).

[61] G.D. Cates *et al.*, *Phys. Rev. A* **45**, 4631 (1992).

[62] W. Happer *et al.*, *Phys. Rev. A* **29**, 3092 (1984).

[63] X. Zeng *et al.*, *Phys. Rev. A* **31**, 260 (1985).

[64] W. Happer, *Rev. Mod. Phys.* **44**, 169 (1972).

[65] W. Happer and W.A. Van Wijngaarden, *Hyp. Int.* **38**, 435 (1987).

[66] S. Appelt *et al.*, *Phys. Rev. A* **58**, 1412 (1998).

[67] D.K. Walter *et al.*, *Phys. Rev. A*, (in press for November 1998).

[68] B.T. Saam, Ph.D. thesis, Princeton University, unpublished, 1995.

[69] R.L. Streever and H.Y. Carr, *Phys. Rev.* **121**, 20 (1961).

[70] Ultrapure Systems, Inc., Nitrogen purifier part No. 00040-VCR-N2.

[71] N.W. Ashcroft and N.D. Mermin, *Solid State Physics* (W.B. Saunders, Philadelphia, 1976).

[72] K.C. Hasson, Senior thesis, Princeton University, unpublished, 1989.

[73] D.E. Kaplan and E.L. Hahn, *J. Phys. Radium* **19**, 821 (1958).

[74] S.R. Hartmann and E.L. Hahn, *Phys. Rev.* **128**, 2042 (1962).

[75] E. Fukushima and S.B.W. Roeder, *Experimental Pulse NMR: A Nuts and Bolts Approach* (Addison-Wesley, New York, 1981).

[76] K.L. Sauer, R.J. Fitzgerald, and W. Happer, *Chem. Phys. Lett.* **277**, 153 (1997).

[77] J. Kestin *et al.*, *J. Phys. Chem. Ref. Data* **13**, 229 (1984).

[78] J. Crank, *The Mathematics of Diffusion* (Oxford University Press, Bristol, 1975).

[79] F.J. Adrian, Ph.D. thesis, Cornell University, University Microfilms Inc., 1955.

[80] F.J. Adrian, *Phys. Rev.* **136**, A980 (1964).

[81] F. Reif, *Fundamentals of Statistical and Thermal Physics* (McGraw-Hill, New York, 1965).

[82] R.S. Mulliken, *J. Chem. Phys.* **52**, 5170 (1970).

[83] SurfaSil consists primarily of dichloroctamethyltetrasiloxane and is a trademark of Pierce (product # 42855)

[84] A.W. Overhauser, *Phys. Rev.* **91**, 476 (1953).

[85] A.W. Overhauser, *Phys. Rev.* **92**, 411 (1953).

[86] T.R. Carver and C.P. Slichter, *Phys. Rev.* **92**, 212 (1953).

[87] T.R. Carver and C.P. Slichter, *Phys. Rev.* **102**, 975 (1956).

[88] I. Solomon, *Phys. Rev.* **99**, 559 (1955).

[89] J.H. Noggle and R.E. Schirmer, *The Nuclear Overhauser Effect: Chemical Applications* (Academic Press, New York, 1971).

[90] D. Neuhaus and M.P. Williamson, *The Nuclear Overhauser Effect in Structural and Conformational Analysis* (VCH, New York, 1989).

[91] C.R. Bowers *et al.*, *Chem Phys. Lett.* **205**, 168 (1993).

[92] B. Driehuys *et al.*, *Phys. Lett. A* **184**, 88 (1993).

[93] H.C. Gaede *et al.*, *Appl. Magn. Reson.* **8**, 373 (1995).

[94] T. Pietrass *et al.*, *Abstr. Pap. Am. Chem. S.* **213**, 418 (1997).

[95] E. Brunner *et al.*, *Chem. Phys. Lett.* **290**, 112 (1998).

[96] Carbon Disulfide enriched to 97%-99% ^{13}C can be bought from Cambridge Isotope Laboratories, Inc. (catalog # CLM-730) for $235/0.5 g.

[97] J.R. Lyerla, Jr. *et al.*, *J. Phys. Chem.* **75**, 3967 (1971).

[98] R.G. Parker and J. Jonas, *J. Magn. Reson.* **6**, 106 (1972).

[99] Y.-Q. Song *et al.*, *Angew. Chem.* **109**, 2464 (1997); *Chem. Int. Ed. Engl.* **36**, 2368 (1997).

[100] K.L. Sauer, General's Project, Princeton University, unpublished, 1995.

[101] M.A. Bouchiat and J. Brossel, *Phys. Rev.* **147**, 41 (1966).

[102] C.M. Bartle and H.O. Meyer, *Nuc. Instr. Meth.* **112**, 615 (1973).

[103] D.W. Sindorf and G.E. Maciel, *J. Am. Chem. Soc.* **105**, 3767 (1983).

[104] B. Arkles, ed., in: *Gelest: Metal-Organics Including Silanes and Silicones* (Gelest Inc., Tullytown, PA, 1995).